RADIOISOTOPE POSITRON PROPULSION

NIAC PHASE I REPORT

PI: Ryan W. Weed, PhD

Co-I: Joshua Machacek, PhD

Co-I: Balachandar Ramamurthy

Positron Dynamics Inc

This material is based upon work supported by NASA under award 80NSSC18K0910.
Any opinions, findings, and conclusions or recommendations expressed in this material are those of the author(s) and do not necessarily reflect the views of the National Aeronautics and Space Administration.

EXECUTIVE SUMMARY

After decades of travel, the fastest man-made object, the Voyager Spacecraft, has only recently passed the edges of our solar system. Since the launch of Voyager in 1977, spacecraft engines have not fundamentally changed. In regard to asteroid mining, the use of chemical propellants is not practical due to their low specific impulse and ultimately insufficient delta-V.

The incredible energy density of antimatter is the key to unlocking the solar system for practical business and human exploration. When antimatter annihilates with matter, it releases an amount of energy equal to the rest mass of both particles in the form of photons. This results in a specific energy of 90MJ/ug, the highest known specific energy of any process. Since the prediction and discovery of antimatter in the 1920's and 1930's, its' use as an energy source for rocket propulsion has been considered in many forms but has yet to be demonstrated.

Producing antimatter is straight forward, but antimatter trapping is challenging. Our concept uses a radioisotope to generate antimatter via beta-decay. These antimatter particles are collected, and their density tailored to generate fusion reactions which provides high performance thrust. The neutrons produced in the fusion reaction are used to generate more radioisotope via neutron capture. This constitutes the first closed-closed cycle antimatter rocket engine of its kind.

Why Positrons? The positron, or anti-electron, is the antimatter counterpart of the electron. It has the same mass as an electron but opposite charge. Positrons are produced by several readily available radioisotopes (e.g. Na-22, Co-58, Kr-79) in large number and with a broad energy spread. By creating long-lived radioisotopes that emit positrons, we can essentially 'store' the positrons in the nuclei of the radioisotope, eliminating the need for high magnetic field storage techniques.

In light of these high delta-V mission opportunities and Positron Dynamics' technology developments, we propose a means of antimatter-based propulsion that does not require gamma ray reflection, long-term storage of antiprotons or positrons, and can be integrated into a medium sized (<1000kg) spacecraft. In this Phase I effort, we have analyzed the feasibility of this radioisotope positron propulsion (RPP) concept. In addition, we have applied the concept to a specific mission, the capture/redirect of asteroid 2009BD, comparing the performance of RPP with the original electric propulsion ARM concept.

Contents

This page intentionally left blank

1.Introduction – Antimatter Propulsion

The idea of using antimatter as a propulsion fuel for spacecraft was proposed by Eugene Sanger in the 1950's [1] (Fig 1). Significant technical barriers have kept the cost of usable antimatter well outside the realm of propulsion applications, but progress has been made in recent years. This section will cover some background on antimatter propulsion, a positron physics introduction, and a quick look at previous work in antimatter propulsion.

1.1 **Background**

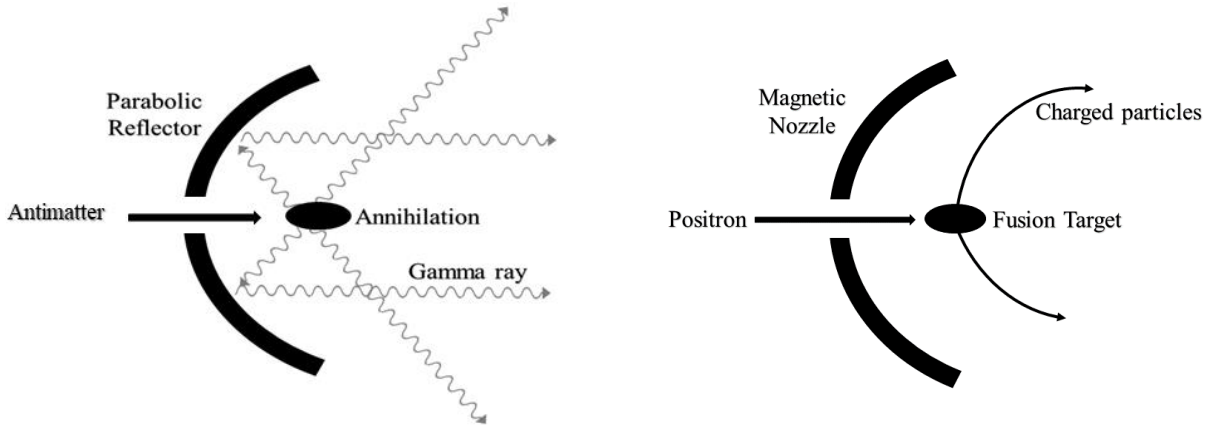

Figure 1. On the left, the original 'Photonraket' design of Sanger [2]. On the right, the annihilation events generate fusion reactions and charged particles which are guided to produce thrust.

Early concept did not completely consider the technological and financial hurdles required to produce and store massive amounts of antimatter, nor the challenge of directing the energy produced in annihilation of antimatter and matter. Anti-protons and positrons are the two antimatter particles most often considered for propulsion applications.

In general, positrons are significantly easier to produce, while anti-protons require accelerator energies on the scale of CERN. Over the past 20 years the cost of radioisotope-based positron production has decreased, and the techniques have become more widely known [3, 4]. Our solution to antimatter propulsion is based on using radioisotope sources of positrons to generate fusion reactions in solid targets (see Fig. 1).

1.2 **Positrons – The Basics**

The positron is the antimatter counterpart of an electron and is sometimes referred to as the anti-electron. It has the same mass as an electron (511.0031 +/- .0032 keV/c^2)[49], but opposite charge

and magnetic moment. Like the electron, the positron is a fermion with spin +1/2 or -1/2. It's lifetime in vacuum is essentially infinite (>10^{21} years; [50]).

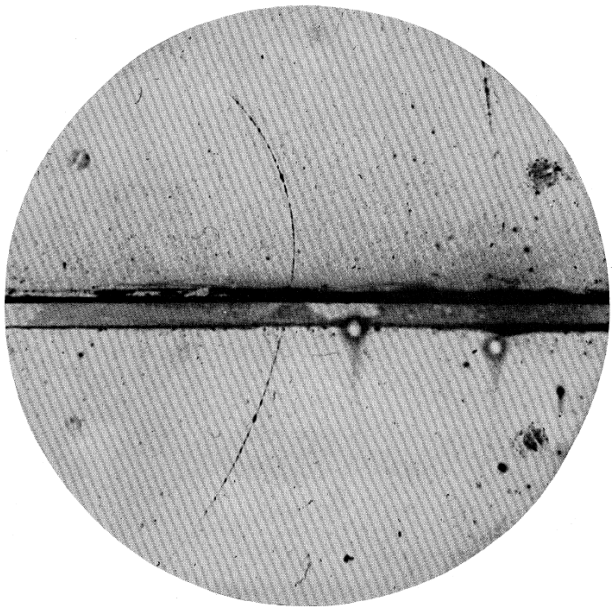

Figure 2. Predicted by Dirac in 1930, the positron was discovered years later at Caltech by Carl Anderson who captured this 63MeV positron bending the "wrong way" in this historic cloud chamber track [51-53]. Reproduced from [51].

1.2.1 Positron Sources

There are many ways to create positrons (see Fig. 3). Most sources of positrons require massive amounts of infrastructure (e.g. Nuclear reactor, Linear Accelerator, kJ Laser Facilities). For the purposes of spacecraft propulsion, a radioisotope source is the most attractive as it does not require power to generate antimatter because the unstable isotope decays naturally. A refined quantity of radioisotope will have relatively low mass and a high activity limited only by the specific activity of the radioisotope.

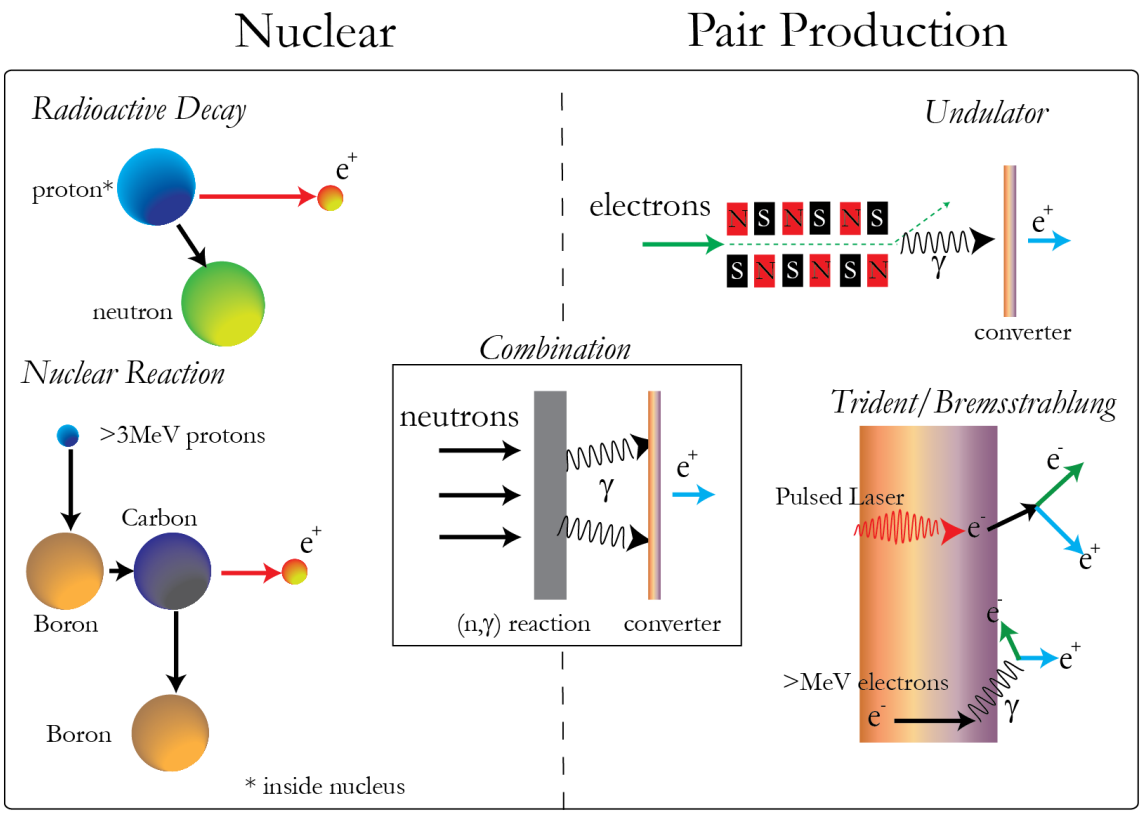

Figure 3. Creating positrons. Most of the radioactive positron sources make use of (p,n) or (n,γ) reactions in accelerators or reactors to produce a positron emitting isotope [54].

1.2.2 Annihilation

A unique property of antimatter interactions with matter is the possibility of annihilation, or the conversion of the total energy (kinetic and rest mass energy) of two particles into electromagnetic radiation. For an electron and positron, the annihilation process can be understood in terms of their associated Feynman diagrams, shown in Fig. 4.

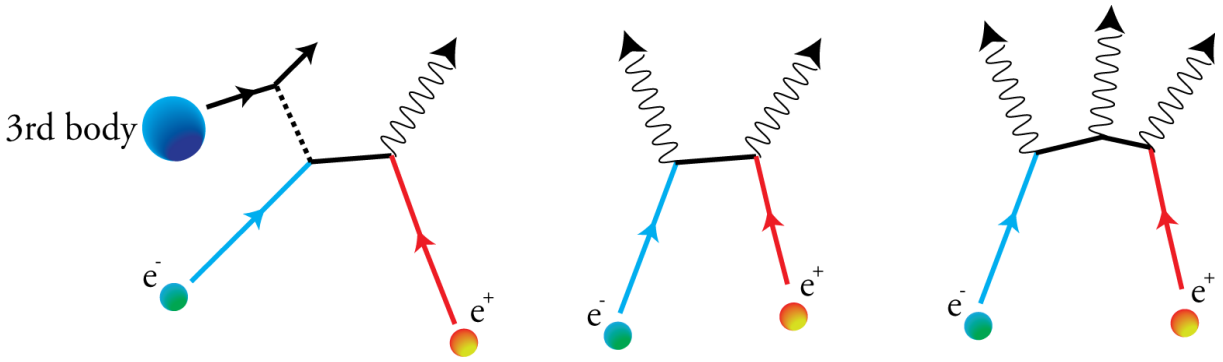

Figure 4. Feynman diagrams for the one, two and three-photon annihilation events.

Single photon annihilation is only possible in the presence of a 3rd body, typically an electron or nucleus which can absorb the recoil momentum required by conservation. The addition of a vertex in the Feynman diagrams, illustrated above, decreases the probability of such an event by a factor of the order of the fine structure constant, $\alpha \sim 1/137$, hence the cross section for 3-photon annihilation is more than two orders-of-magnitude smaller than for 2-photon annihilation [62].

In condensed matter, the positron will rapidly thermalize through interactions with the surrounding electrons. Eventually, the positron will annihilate with an electron in the material and emitting several gamma rays. In metals, the positron will annihilate with a mean lifetime of, typically, only a few hundred picoseconds. In insulators and in large open volumes in semiconductors, the positron can bind with an electron to form an atom of positronium (Ps), the bound state of an electron-positron pair.

1.2.3 Positrons in Materials

From the time of impact on the surface of a material, the positron can undergo many processes spanning approximately six orders-of-magnitude in time through thermalization, diffusion, trapping, and eventually annihilation with an electron. Fig. 5 shows the characteristic timescales of different processes in the life of a positron.

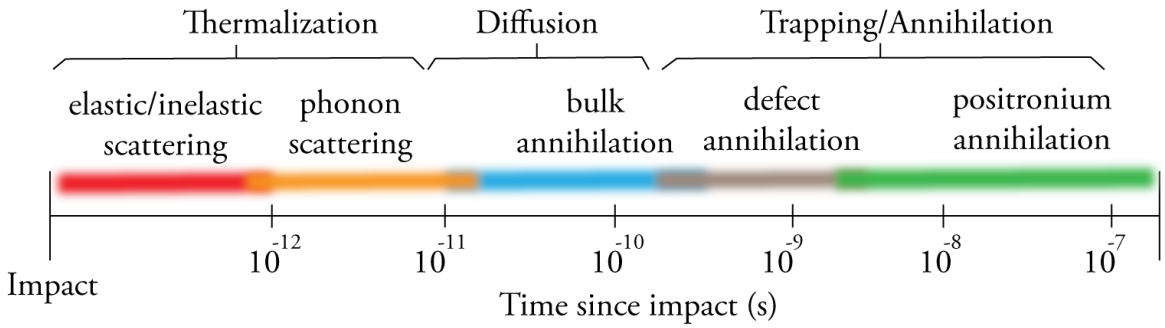

Figure 5. Positron timeline in materials from impact to annihilation.

Once thermalized, positrons will diffuse until they either annihilate in the bulk or are trapped in a defect or surface state. Diffusing positrons are repelled by nuclei and spend most of their time in the interstitial regions between atoms of the lattice. Positrons can be ejected from the surface of a material if the surface has a negative work function allowing the moderation of and ensemble of positrons.

1.2.4 Moderation

All known positron sources produce a continuous distribution of positrons with high energy in the range between a few hundred keV to several MeV. In order to use these positrons, they have to be cooled to more reasonable temperatures (~eV). Madansky and Rasetti realized the need for a cooled source of positrons in the 1950's but were unsuccessful in their first attempts at moderation [55]. Slow positron production was not observed until 1958, when Cherry used a chromium-on-mica surface to produce positrons with 0-5eV energies with an efficiency of fast to slow conversion of 10^{-8} [56].

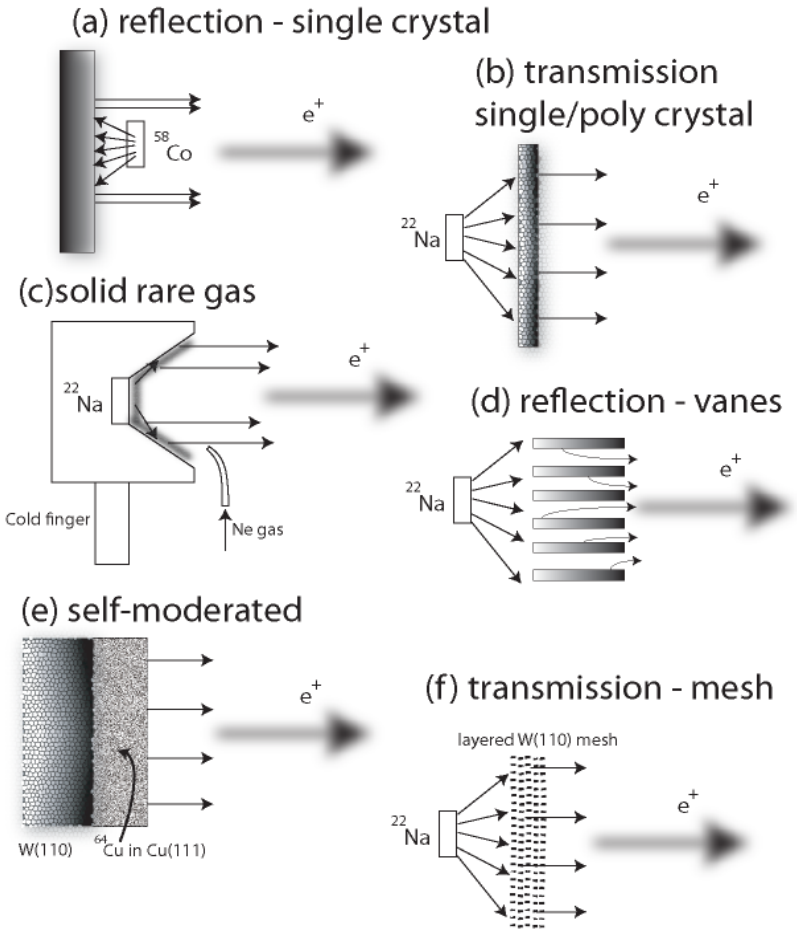

Figure 6. Different moderation geometries and techniques.

In the late 1980's, it was discovered that solid-state rare-gas crystals produced low-energy positrons with extremely high efficiencies approaching 1% [57]. Positrons emitted from these moderators do not have a thermal energy distribution, as is the case with the metallic moderators. The mechanism for moderation is consistent with the 'hot' positron model, where positrons are emitted from the surface due to their incomplete thermalization because of the absence of efficient energy loss mechanisms below the electric band-gap.

The efficiency of modern positron moderators is currently limited by the short diffusion length of the positrons inside the bulk, typically a few tens or hundreds of nm's. In the presence of an electric field, however, positrons will gain a drift velocity in the direction of the field, in principle increasing their diffusion length. This technique was first proposed in 1979 and is referred to as Field Assisted Moderation (FAM) [58,59]. FAM has been used to increase the positron diffusion length in Diamond [60] by applying a potential to deposited Au mesh, although the absolute efficiency was limited by the annihilation at the deposited Au layer.

Positron Dynamics has developed a new moderator geometry that utilizes FAM and a crossed electric and magnetic field extraction technique that is expected to reach much higher moderation efficiencies than currently achievable with solid rare gas moderator geometries. (see Proprietary Appendix X).

1.2.5 Positron Beams

In order to use a high-efficiency positron source based on the rare gas moderator, which does not lead to complete thermalization, an additional step is required to obtain a room temperature, or completely thermalized, beam. A number of techniques have been developed [81].

The trapping of positrons within a buffer gas trap (BGT) relies on inelastic collisions with the buffer gas or gases. Inelastic collisions with a trapping gas are used to dissipate the kinetic energy of the positrons so that they can be trapped within an electrostatic well. The trapped positrons thermalize with the system via collisions with a cooling gas. Typically, nitrogen (N_2) is used as a trapping gas and tetrafluoromethane (CF_4) is used as a cooling gas. The various techniques that have been developed over the past 20 years or so have been recently reviewed [81]. A buffer gas traps (BGT) can be used to generate a high-repetition rate or high-intensity beam [82]. An example of a BGT used for daily operation at the University scale is shown in shown in Fig. 7. Here, a mono-energetic positron beam is used to investigate the Nano-scale vacancies using a technique known as beam-based Positron Annihilation Lifetime Spectroscopy (PALS). Work towards a binary-gas BGT [83,84] should result in the simplification of the supporting equipment required to operate a BGT.

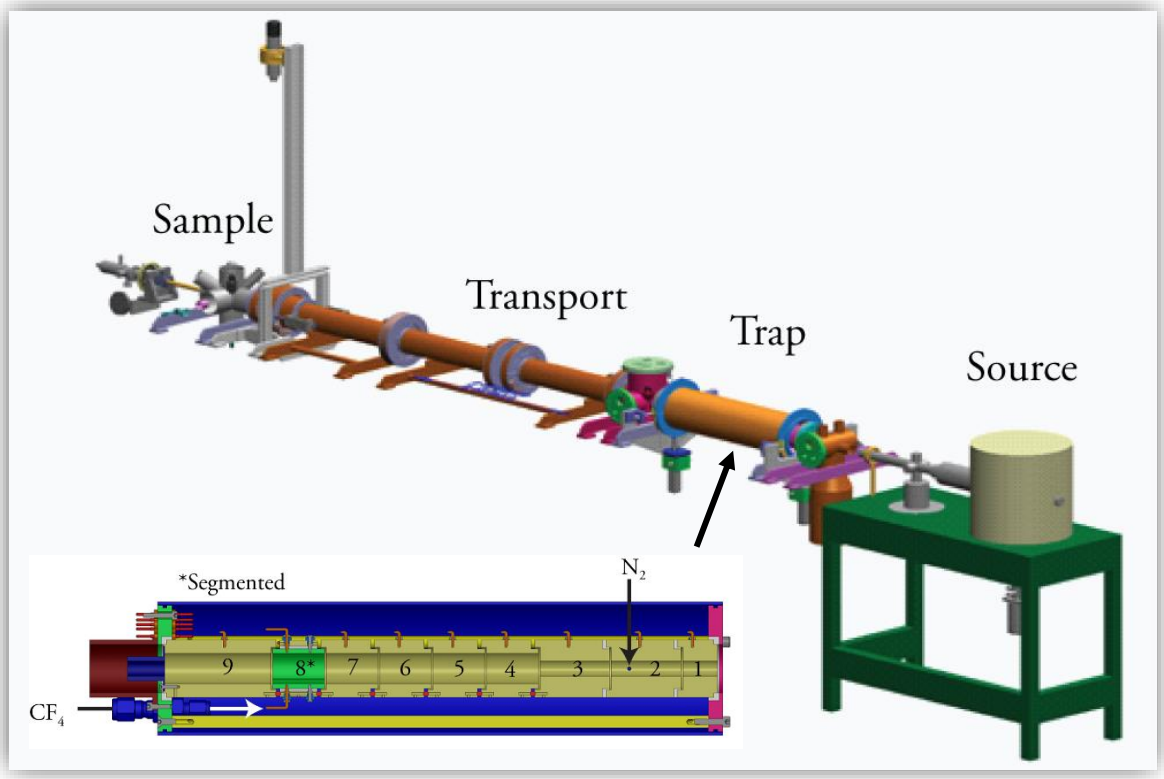

Figure 7. A typical university research positron beamline, using radioisotope source with frozen rare gas moderator, buffer gas trap (inset) and magnetic transport to a sample. Reproduced from [80].

1.3 Previous Concepts and Challenges

Since the discovery of the anti-electron in the 1930's, there have been several proposed concepts for antimatter-based propulsion, none of which have been demonstrated. The main driver behind these concepts is the energy density of antimatter (when annihilated with matter) at 90MJ/ug, the highest of any known substance. In 2015, NASA's Office of the Chief Technologist released a 'Technology Roadmap' which describes the technological hurdles that must be overcome in order to move beyond chemical propulsion and harness the potential of antimatter [75].

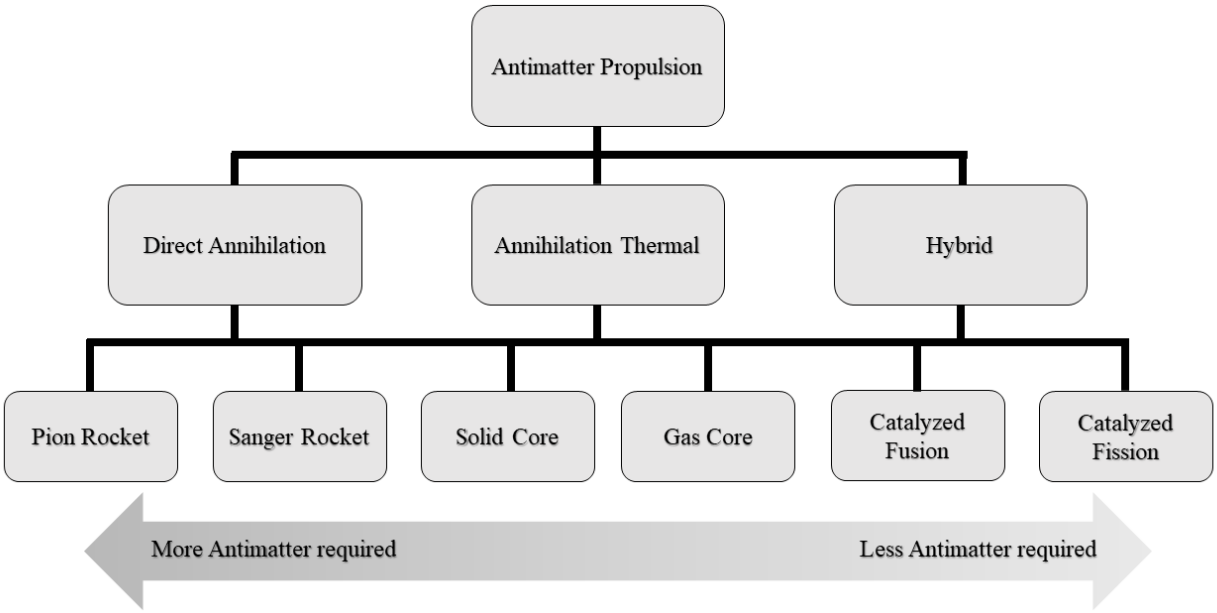

Figure 8. The Taxonomy of antimatter propulsion.

In general, the earlier concepts like antiproton/proton annihilation (i.e. Pion Rocket) utilized annihilation products directly to produce thrust. While these concepts promise incredibly high propulsion performance, they required massive amounts of antimatter (antiprotons) not feasible in the foreseeable future.

It is the direct conversion of mass to electromagnetic energy which makes antimatter propulsion the 'holy-grail' of in-space propulsion. Using gamma rays directly for propulsion, as envisioned by Sanger in the 1950's, requires the ability to efficiently reflect gamma rays. No currently known (solid state) material is capable of gamma-ray reflection. In general, the absorption of photons scales with the mass of the material. Thus, it is likely that a gamma-ray mirror would be prohibitively massive for a spacecraft. Without a gamma-ray mirror, the only mechanism known to produce a well collimated beam of gamma-rays is the gamma-ray laser. This requires production and control of a Bose-Einstein Condensate (BEC) of positronium atoms (a bound state of a positron and an electron). To-date, a BEC of positronium has not been produced.

Later concepts used the annihilation energy to heat a propellent before exhausting in a traditional rocket nozzle. In the 1990's, hybrid concepts were developed that took advantage of the high energy density of antimatter to catalyze fusion or fission reactions [70-72]. These concepts rely on the transfer of energy from annihilation events to produce fission and/or fusion reactions [6, 7], but required unrealistic amounts of stored antiprotons or anti-hydrogen using current technology.

More recently, it was shown that positrons are created by intense laser pulses on high-Z targets using the Trident/Bremsstrahlung process [73]. In this work, 2 x 10^{10} positrons were created from a single shot of the Titan Laser at LLNL, at ~200J per pulse. Based on this, propulsion concepts were developed that utilize laser produced positrons to catalyze fusion reactions [74]. The performance of such a system is likely limited by the inefficient conversion of laser photons to positrons (10^{11}positrons/kJ), and the requirement to moderate and direct the very high energy positrons (>MeV) towards interaction with a fusion fuel. If an on-board laser were used (i.e. interplanetary missions), the mass of the laser required to generate fusion burns would further reduce overall system performance. Similarly, pulsed lasers have been used to initiate fusion reactions, however, the mass and power requirements of such laser driver systems limits their use in space propulsion applications [8,9], using current laser technology.

In 2006, a NASA Institute for Advanced Concepts (NIAC) study of positron propulsion investigated 3 different positron fueled engines; solid-core, gas-core, and ablative [5]. This study investigated techniques requiring ug's to mg's of stored positrons but offered only moderate improvements to specific impulse over chemical and nuclear thermal propulsion. Storage of ug's of positrons requires a several orders of magnitude improvement over current state of the art. Antiprotons (and anti-Hydrogen), while offering much larger amount of energy per annihilation event, not only require large accelerators (e.g. CERN, Fermilab) to produce, but they also face the same storage difficulties as positrons.

Storage Limitations

The fundamental limit of any charged particle beam system is the space charge limit. This occurs when the charge density becomes sufficiently high that the beam interacts with itself. In a charged-particle trap most common to positron beam physics, the charge density repulsive forces are counteracted by the 'end-cap' electrodes. As the charge density increases, so to does the required electrode potential to contain it. Ultimately, unrealistic potentials are required. In addition, confinement in the radial direction require a magnetic field. This drives another fundamental trap density limitation, called the Brillouin limit. The Brillouin limit requires that the energy stored in the rest mass of the trapped particles is always less than the energy stored in the confining magnetic field [85]. This is the primary reason for the relatively low performance of 'antimatter-trap' based propulsion concepts.

The primary challenges of an antimatter propulsion system include:

1. Production & Storage of antimatter
2. Conversion of the annihilation products into propulsive force

To address challenge #1 above, we propose the use of a radioisotope source of positrons (Kr-79) produced via neutron capture, eliminating the need for long-term storage of antimatter

To address challenge #2 above, we utilize the positron-electron annihilation energy to catalyze a nuclear fusion reaction(s), resulting in fast charged particle products that produce thrust.

1.4 Asteroid Retrieval

One application where a high specific impulse antimatter-based propulsion system would be beneficial is an asteroid capture and return mission. This type of mission is demanding not only in the spacecraft propulsion requirements, but also in the rapid response required, from detection to mission launch. Therefore, minimizing launch mass is a critical factor in mission design – as this expands flexibility in launch vehicle opportunities.

Cost effective access to asteroids opens up a range of applications such as mining for resources, including several rare materials used in electronics and other manufacturing, and in situ resource utilization (ISRU) for subsequent interplanetary missions. (e.g. water for life support, Deuterium fuel). Retrieval of the entire asteroid and bringing it to the proximity of Earth at a low cost, allows for the return on investment to be realized and for potential commercial markets to be created. Another important facet of RPP capability is the improved reconnaissance of asteroids through rapid scout and sample return missions. This may also be important to the long-term planetary defense from asteroid impact- understanding both the makeup of asteroids with the potential to collide with Earth as well as developing a means to alter their orbits are essential capabilities [119].

We will describe a high specific impulse propulsion system - Radioisotope Positron Propulsion (RPP) - and compare this system with Solar electric propulsion (SEP) in the context of an asteroid retrieval mission.

2. Technology Concept:

Currently, Antimatter Annihilation Catalyzed Fusion Propulsion is a concept that has been formulated and analyzed [11,38,39], although no experimental demonstration of thrust has been realized. Thus, we assign the current TRL as (1-2). The goal of this Phase I work was to advance the RPP thruster concept to TRL (3) by documenting and describing the feasibility of the concept.

Radioisotope Positron Catalyzed Fusion Propulsion works by injecting pulses of positrons onto a region of high Deuterium density [10,11]. The positron-electron annihilation couples to a lattice-trapped deuteron giving it a kinetic energy kick [12]. This 'knock-on' process provides a mechanism to accelerate Deuterium ions using positrons. The accelerated deuteron has sufficient kinetic energy to fuse with other deuterons in the substrate [13]. Thus, the high energy density of antimatter (positrons) can be converted into kinetic energy of a deuteron leading to a fusion reaction. These

fusion reaction products produce the propulsive force. Neutrons from these fusion reactions are captured in a nozzle blanket to produce a positron-emitting radioisotope, which is enriched and deposited onto a source layer, producing more positrons and more thrust. This 'breeder' fuel cycle avoids the need to store large amounts of antimatter and allows for launch with a minimal amount of radioisotope.

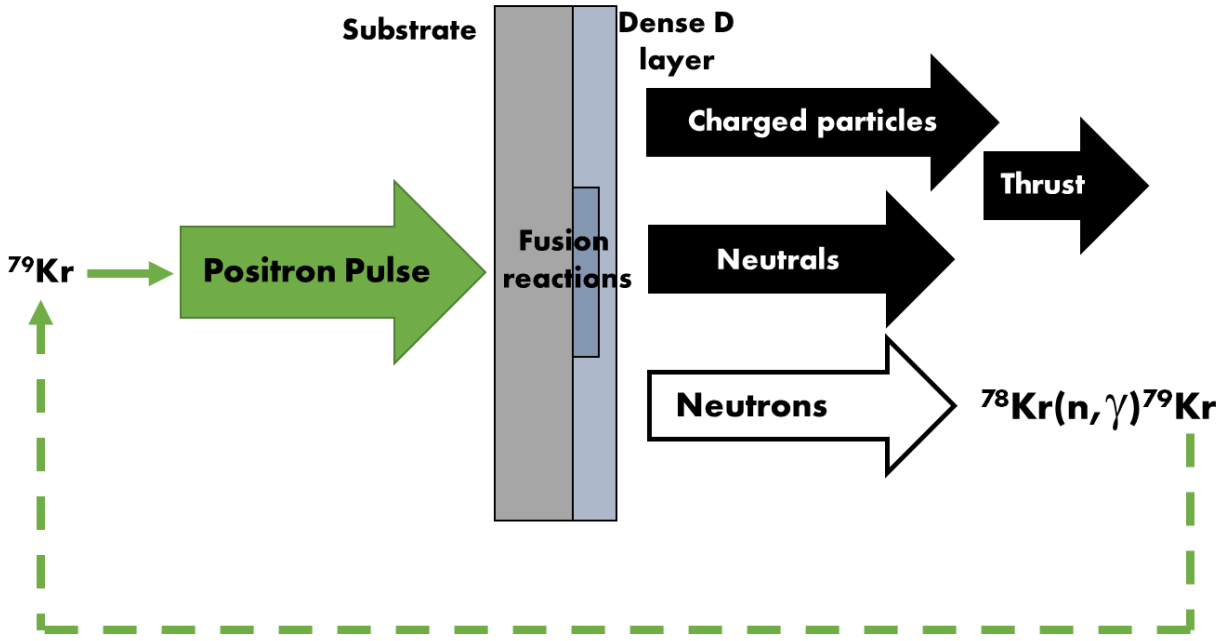

Figure 9. RPP Concept overview

2.1 Coupling positron annihilation energy

It has been postulated that positron-electron annihilation could induce fusion reactions in hydrogen isotopes. This 'knock-on' mechanism is similar to the positron nuclear excitation process described by

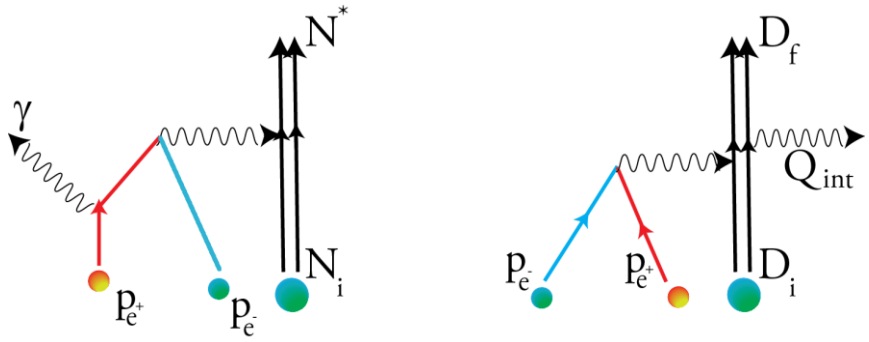

Figure 10. Feynman diagrams for Inelastic Nuclear Excitation Process (left) and the Morioka Process (right). Q_{int} describes the sudden momentum transfer interaction with the surrounding crystal (analogous to the Mossbauer effect).

Raghavan and Mills [14] and has been shown experimentally to produce excited metastable states of surrounding nuclei (Fig. 10 left) [15-17].

Fig. 10 (right) shows the Feynman diagram for a similar nuclear excitation process, whereby a virtual photon imparts a large amount of kinetic energy to a trapped deuteron, theorized by Morioka [12]. The fusion rate becomes $\lambda_F^D = R\lambda_F$ where R is the non-relativistic spin averaged differential cross section for the momentum transfer process described above. Although the value for R will depend on the substrate material characteristics, it has been calculated to be R~10^{-3} for reasonable atomic parameters. Initial measurements of this probability indicate R is closer to 0.1 [18]. The higher than expected value for R is not yet explained. However, Morioka's original theory did not take into account more than a single Deuterium atom in a lattice vacancy. As such, the local density and quantum state are likely to play a role in the annihilation momentum transfer probability.
Once this momentum transfer to the deuteron occurs, the fusion reaction probability is determined by the DD fusion cross-section and surrounding Deuterium number density [13,19].

2.2 Ignition

By combining dense Deuterium surface states with an intense pulsed positron beam, our aim is to generate a fusion burn in a planar target. While the physics of inertial confinement fusion (ICF) has been developed over the last five decades [88], this concept differs in several important ways. Typically, ICF geometry is spherical, not planar. To reach sufficient densities and temperatures, lasers (ICF drivers) pre-compress the fusion fuel. This process leads to several inefficiencies (e.g. Rayleigh-Taylor instability) that make producing fusion burns, and reaching break-even energy production, difficult. During this compression of the fusion target, densities approaching 10^2g/cm^3 can be achieved. By creating dense Deuterium clusters in a thin substrate with densities >10^5g/cm3 [27,28], we eliminate the need for a laser compression.

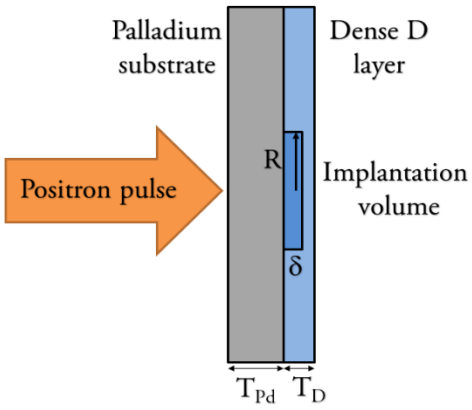

Figure 11. Microfusion ignition of Deuterium based on pulsed positron beam implantation.

While spherical symmetry is lost, we can still estimate energy deposition required to satisfy Lawson criteria for ignition; charged particle focusing limits place a realistic lower bound on positron beam diameter. Another limiting factor is positron pulse duration. Positron beam pulse widths of <400ps are routinely created in the lab [4]. Simulation and analysis results for ignition characteristics are included in Section 3.2.

2.3 Positron source breeding

While radioisotope sources with long half-lives (>1 yr.) made with proton accelerators (e.g. Na-22) on earth are sufficient for low-thrust or small total impulse [11], a regenerative source of positrons will be required to reach thrust levels required for more demanding missions like ARM.

This is mainly due to self-absorption, which becomes a limiting factor for long half-life radioisotopes. For example, self-absorption in Na-22 limits the specific activity to ~1Ci/cm^2[136], making a kCi source unreasonably large. Fortunately, the Deuterium-Deuterium fusion process produces an abundance of fast neutrons.

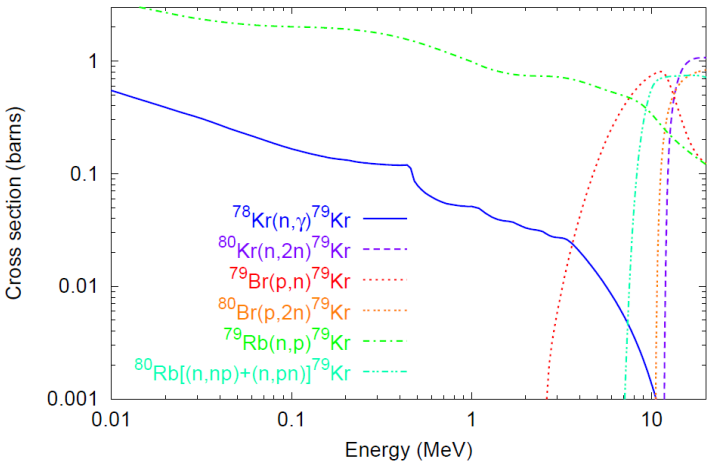

Figure 12. Production channels for 79Kr, including the neutron capture cross section 78Kr(n,g)79Kr (solid blue) considered for breeding positron emitting radioisotope 79Kr. Reproduced from [33].

As such, we propose a radioisotope breeding technique that utilizes the neutron capture cross section of Krypton-78 [33] to produce Krypton-79, a positron emitting radioisotope with 35-hr half-life (see Fig. 12). Using neutrons in this manner to generate a positron beam was originally conceived by Mills in 1990's [35,36]. It is estimated that 10-100 atm blanket of pressurized Kr will be sufficient to thermalize these hot neutrons within a reasonable length scale (<1m). The Kr then passes into the cryogenic isotope enrichment stage. This allows for source specific activities (>kCi/g) high enough to generate the number of positrons, considering the low branching ratio, required for higher thrust levels. The Krypton blanket is described in detail in section 3.5.2.

2.4 Source and Moderator

Hot positrons are generated from layers of Kr (^{79}Kr-rich) frozen onto a metallic surface adjacent to an array moderator structure. The source thickness is minimized, and the enrichment factor is maximized in order to reduce self-absorption of emitted positrons. The source deposition area is limited practically by the ability to produce strong and uniform magnetic field used to radially confine the positrons produced in decay of ^{79}Kr. We will focus our analysis on source deposition areas between

100-500 cm^2. The moderator, described in Appendix C, utilizes an array of wide band-gap semiconductor (e.g. SiC) thin films in a field-assisted geometry to efficiently produce ~eV positrons.

2.5 Beam System

The purpose of the positron beam system is to generate large pulses of focused positrons and direct them onto a fusion target. The system is composed of 3 sections – accumulator, compression and pulsing (bunching). The challenge with such a system is to maintain high efficiency in each of the stages, while minimizing the size and mass of the entire system for space applications. Details of this system are included in section 3.3.

3. Results:

Key technical questions this report answers:

1. Given recent measurements of positron annihilation catalyzed fusion cross section, is fuel ignition achievable using pulsed positron source?
2. Can the required positron source, accumulator and charged particle pulsing optics be integrated into Size, Weight and Power (SWAP) envelope of a spacecraft, while maintaining reasonable propulsion performance metrics?
3. Will the propulsion system benefit a proposed mission supplication (asteroid retrieval)?

Sections 3.1-3.5 provide answers to the first two key questions, and lead to a refined Reference Spacecraft Design which further allows us to answer the mission specific question in Section 3.6.

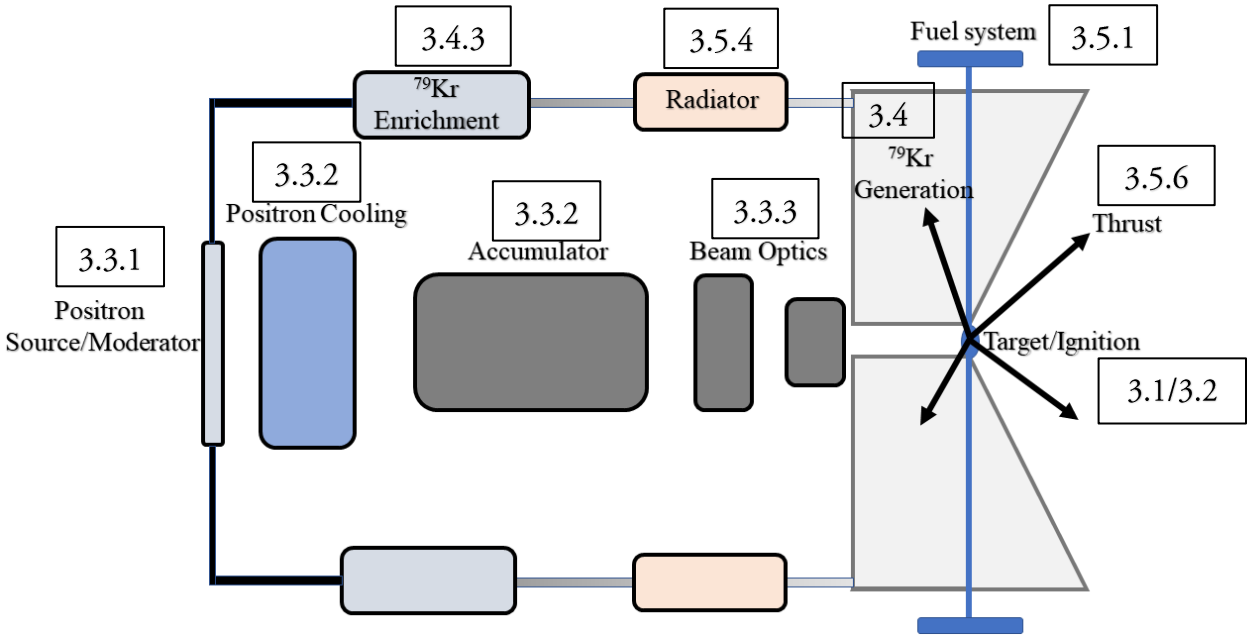

Figure 13. An overview of the RPP subsystems with corresponding analysis/results section.

3.1 Positron Implantation

Can we inject a positron pulse into a localized depth in a fusion target?

To ensure a large fraction of implanted positrons annihilate near or on the interface of the dense Deuterium layer and the substrate, we need to determine the optimum implantation energy and substrate thickness. In order to target a specific depth, the implantation profile $P(z, E)$ must be determined. In simple cases, $P(z, E)$ can be approximated by a 'Makhov profile', named after A.F. Makhov's original work on electron implantation [76], which has been found to agree with measurements [77].

Alternatively, an implantation profile can be determined using a Monte-Carlo simulation of the thermalization process in a (complex) layered system. The computer code PENELOPE is well suited to this task [40]. The simulation algorithm is based on a scattering model that combines numerical databases with analytical cross section models for the different interaction mechanisms with energies up to ~1 GeV.

Transmission / Reflection

A positron incident on a solid surface may be elastically scattered backwards away from the surface or it may enter the bulk of the material. In the context of RPP, reflection will result in reduced propulsion system performance. The reflection of a positron due to nuclear scattering (backscattering) is similar to the electron scattering process with the main difference being the repulsion from atomic nuclei rather than attraction for the case of the electron.

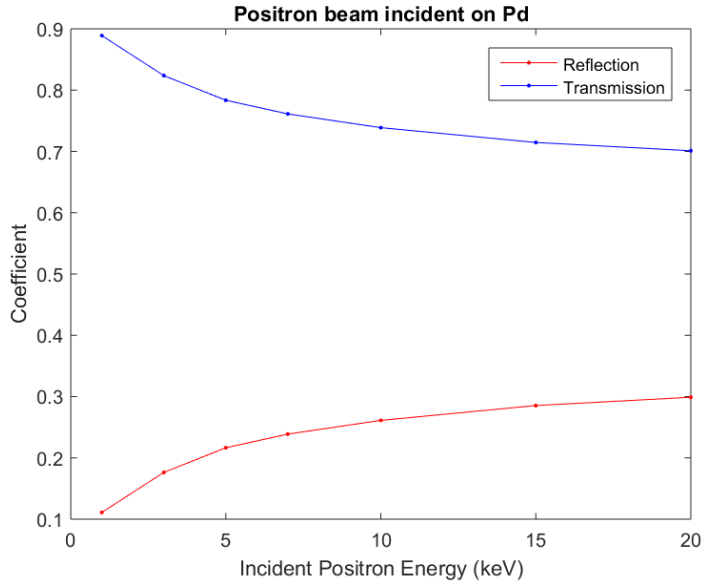

Figure 14. Reflection and implantation coefficients for Pd and Dense Deuterium layer as a function of the incident positron energy (keV).

The reflection and transmission coefficients determined using the PENELOPE code are shown in Fig. 14. These results indicate that a low (~1keV) energy positron beam is optimum to minimize reflections upon implantation into a Pd substrate. The reflection coefficient rises to 30 % by 20 keV. The rapid rise of the reflection coefficient may provide a means of diagnosing the surface of the fuel substrate. As the primary consideration of the positron beam system is to provide a high positron density within the fuel substrate, the reflected portion of the beam could be recaptured to minimize the loss of positrons. Ultimately, the implantation energy needs to be sufficient to optimize the overlap of the implanted positrons and the dense deuterium fuel.

The Planar Target

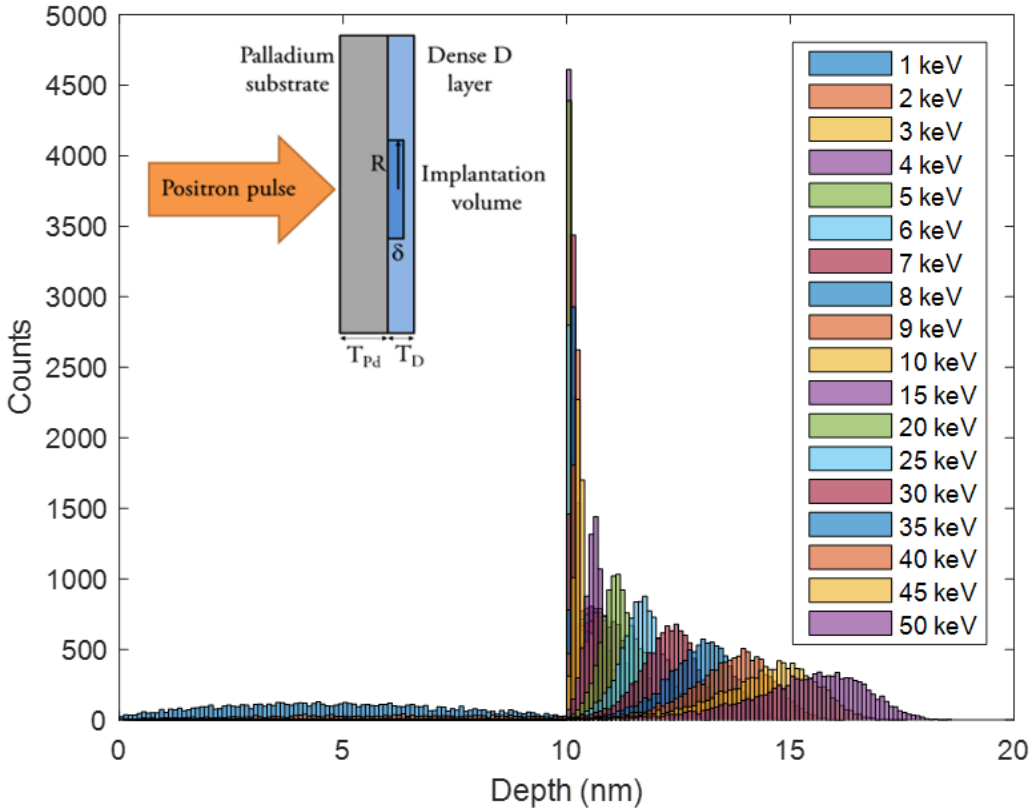

Figure 15: Implantation of positrons into a planar fuel structure shown in the inset with T_{Pd} = T_D = 10 nm for energies ranging from 1 to 50 keV.

The longitudinal extent of the thermalized positrons changes drastically within the planar fuel substrate, as seen in Fig. 15. Channelling is also a possibility in crystalline substrate (Pd)[78], which causes a shift of implantation profiles towards the bulk or skews the distribution deeper into the material. From the results shown in Fig. 15, positrons with energies between 4 and 7 keV enter the fuel substrate and thermalize within the top 1 nm of the dense Deuterium layer after traversing 10 nm of the Pd substrate.

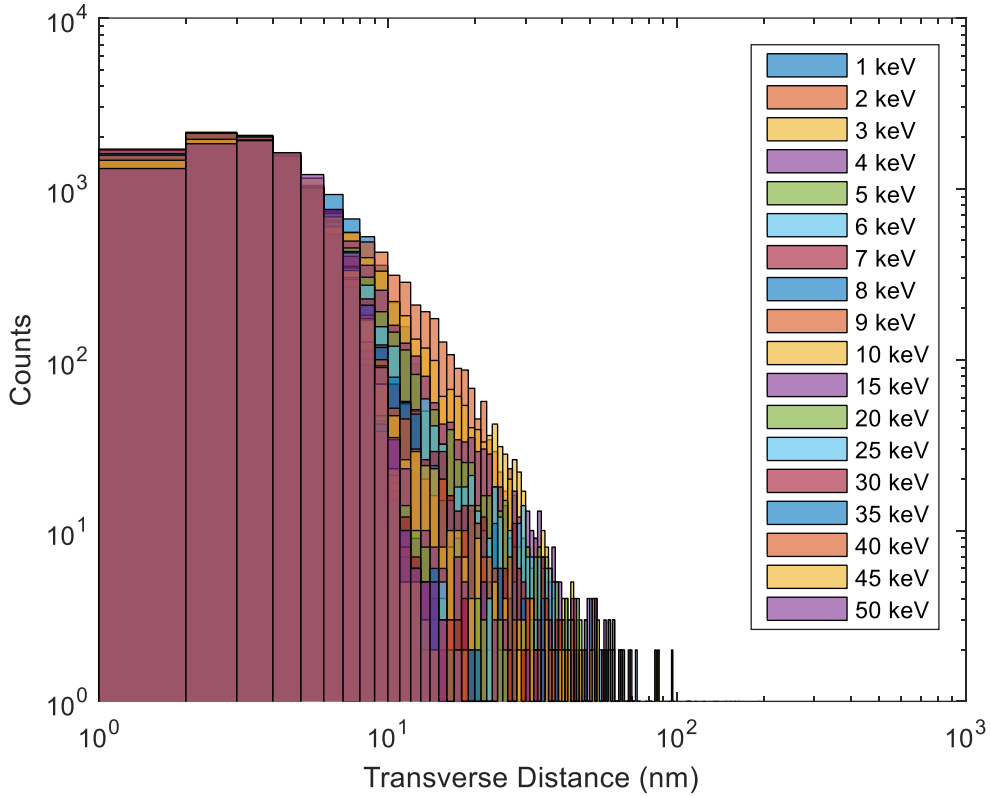

Figure 16: Radial expansion of the positron beam positrons within the fuel substrate (T_{Pd} = T_D = 10 nm) as a function of the incident positron beam energy.

The expansion of the beam in the transverse direction is shown in Fig. 16. At high implantation energies, the transvers extent of thermalized positrons within the fuel substrate is narrower than at low energies. High energy positrons scatter preferentially in the forward direction. Thus, the transvers extent of the positrons at higher energies (~50 keV) is effectively frozen at the Pd-deuterium interface in the fuel substrate.

According to these Penelope results, a positron beam with a kinetic energy between 4 and 7 keV can be injected into a Pd substrate loaded with dense Deuterium located at 10 nm below the surface with an efficiency of 94 %. These positrons will have thermalized with the substrate within a longitude dimension of 1 nm. The radial expansion of the incident beam due to thermalization with the substrate leads to an expansion of the transverse extent by 5-10 nm. This results in an implantation volume within the dense Deuterium layer for a 25 μm radius positron beam of approximately 2e-18 m^3 or 2e-12 cm^3.

3.2 Microfusion ignition using positron annihilation

Can we generate microfusion ignition in solid targets using positron pulses?

Fast ignition is a promising technique for generating inertial confinement fusion, where Deuterium and/or Tritium are first compressed with a set of lasers to densities higher than 100g/cm3, followed by another laser pulse or ion beam that ignites part of the compressed fuel, and the fusion burn propagates across the entire fuel pellet [89].

Previous work with ion-beam driven inertial confinement fast ignition gives us a rough order-of-magnitude requirement for energy deposition requirement to initial a fusion burn in Deuterium-Deuterium fuel. In the fast ignition scheme, it is estimated that a Deuteron beam of approximately 10^{18} ion/cm^2 would achieve ignition in a 10nm thick Palladium foil, loaded with D clusters at a 10% packing fraction [79].

The RPP concept, where the positron/electron annihilation momentum transfers to a Deuteron, has similarities to ion-beam driven inertial confinement fusion concepts. We can make a first positron beam ignition estimate, assuming R=0.1 and a 50um beamspot diameter. In this case, ignition should be achieved with a pulse of 2.5x10^{11} positrons.

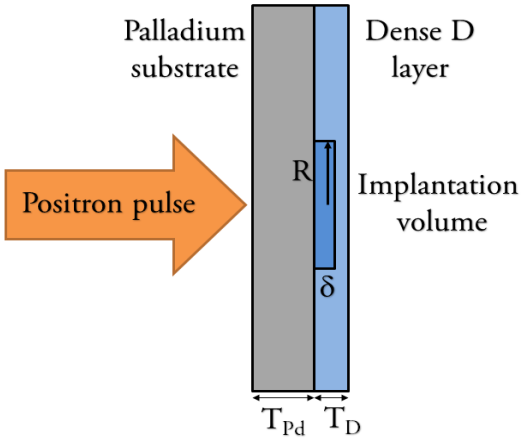

Figure 17. Estimating fusion ignition (Lawson Criteria) based on pulsed positron beam implantation.

3.2.1 Lawson Criteria

Another means of predicting ignition parameters is to use the Lawson Criteria to estimate density, temperature and confinement time requirements to reach ignition [88].

If we consider the Lawson criteria with number density n, confinement time τ:

$n\tau > \frac{12\,k_bT}{<\sigma v>Q}$ Where k_b is Boltzmann's constant and Q ~3.5MeV (for DD fusion). In the case where annihilation of a pulse of 10^{12} positrons injected into a 10um beamspot, a large number of MeV Deuterons in the implantation volume deposits >10^{13} W/cm^2 leading to a ~keV plasma, similar to what has been measured for comparable laser intensities [25-29]. Confinement times can be estimated with the ion sound velocity and hot spot depth, T_D: τ ~ T_D /Cs. Using $C_s = \sqrt{\frac{\gamma Z k_b T_e}{m_i}}$, where γ is the adiabatic index and Z is charge state, gives a sound velocity [19] of $C_s = 2.7x10^5 m/s$ at a temperature of 1keV and a confinement time in the range of 200ns to microseconds assuming D layer thickness >nm.

The DD fusion reaction rate (Maxwellian averaged) at 1keV is $< \sigma v >= 1.5x10^{-22} cm^3/s$. The Lawson Criteria is satisfied when the confinement time is larger than a few nanoseconds (estimated >200ns above).

3.2.2 0-D Model

A 0-D model of positron annihilation catalyzed fusion was developed using measured [Appendix B] positron annihilation momentum transfer probability. This model (see Fig. 18) included a model of radiative energy loss, ionization, and fusion cross sections from most recent databases. Details of the implementation of this model are found in Appendix D.

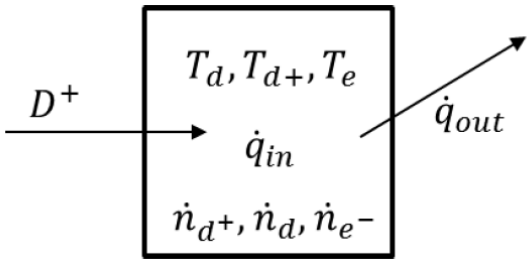

Figure 18. Control volume for 0-D ignition model.

While the model did not include any geometry or boundary conditions, it indicated that a pulse of approximately 10^{11} positrons was sufficient to generate microfusion events in solid D targets for realistic combination of positron implantation densities and target densities and assuming realistic pulse characteristics from previous research (pulse temporal width, pulse width, energy and depth distribution). The model assumes an R value of 0.1 (D^+ density is an order-of-magnitude lower than positron implantation density)

Time Evolution

The simulation code also outputs the species temperatures and densities for each run as a function of time, allowing us to study the temporal evolution of the simulation. Figure 19 and 20 show two such cases. The injection deuteron density is the same in both runs, but the target density is about 1.5 orders of magnitude greater in the plot on the left. Here we can see that once the beam is shut off at $t = 50$ ps, the ion density rapidly decays until matching that of the target. This is an example of the elastic collision transfer. The two population temperatures then continue to decay, likely due to line emission. A very different behavior is seen with the case on the right. Here, there is no clear indicator for when the beam was switched off. The temperature is decaying but at a much slower rate. This indicates that a fusion reaction is ongoing. In this particular case, the reaction will likely eventually

quench itself, however, the time during which the burn is sustained may be sufficient for propulsion application.

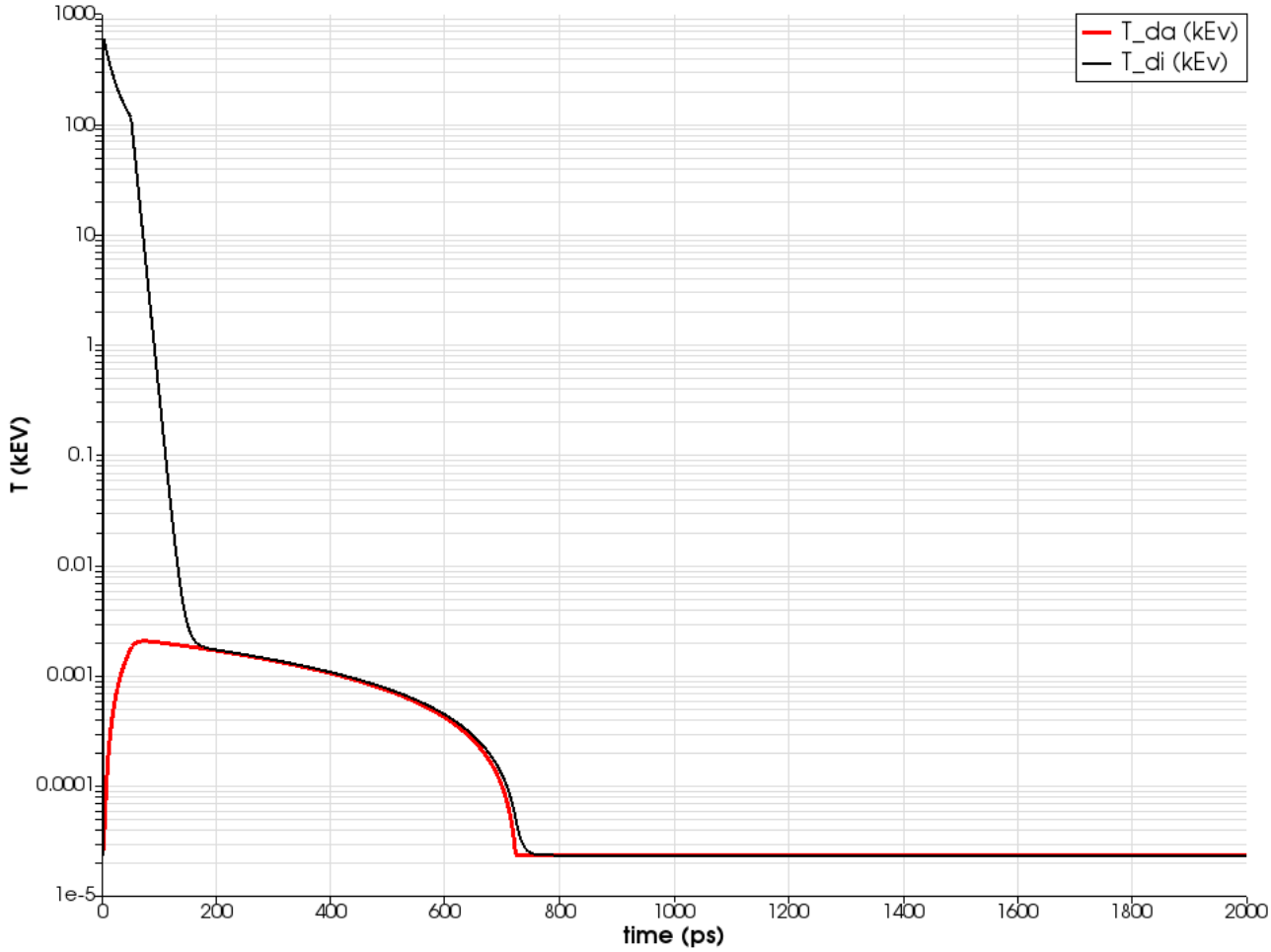

Figure 19. Time evolution of Deuterium (red) and deuteron (black) temperatures for two simulations with $n_{d^+} = 7.8 \times 10^{21}$ *and* $n_d = 2.3 \times 10^{27} m^{-3}$

Fig. 19 shows a case where an insufficient number of positrons are injected into the fuel, and the energy loss mechanisms dominate over fusion energy gains. We also see that the timescale for energy loss is on the order of ~ns, which is promising for the expected positron pulse widths of several hundred ps.

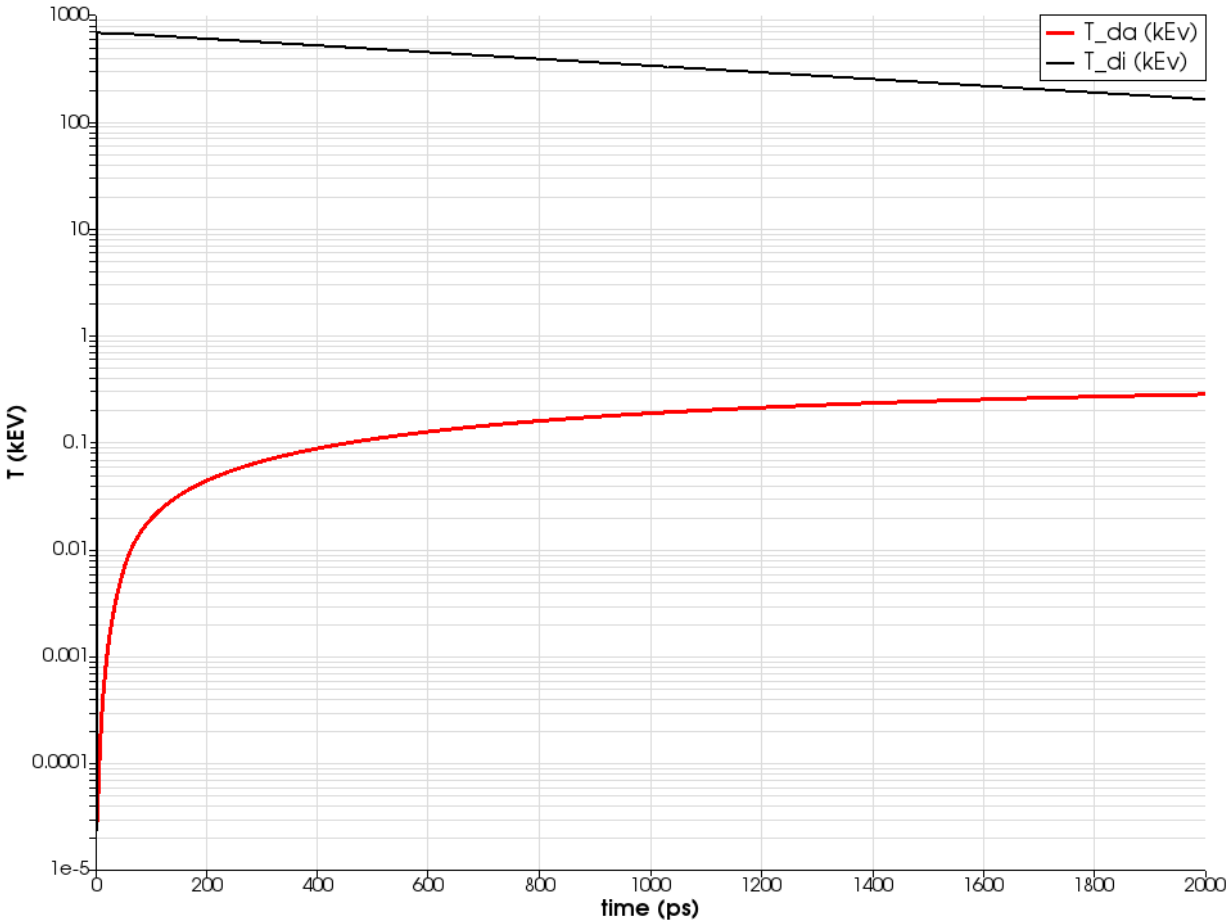

Figure 20. Time evolution of Deuterium (red) and deuteron (black) temperatures for two simulations with $n_{d^+} = 7.8 \times 10^{21}$ *and* $n_d = 2.3 \times 10^{25} m^{-3}$.

Fig. 20 shows the final temperature of Deuterium and tritium atoms as a function of injection deuteron (x-axis) and target Deuterium (y-axis) density. Specifically, these plots indicate that the density of the energetic deuterons from the annihilation reaction needs to reach at least 10^{20} m^{-3} for the fusion to ignite. Interestingly, the model predicts an influence of the target density.

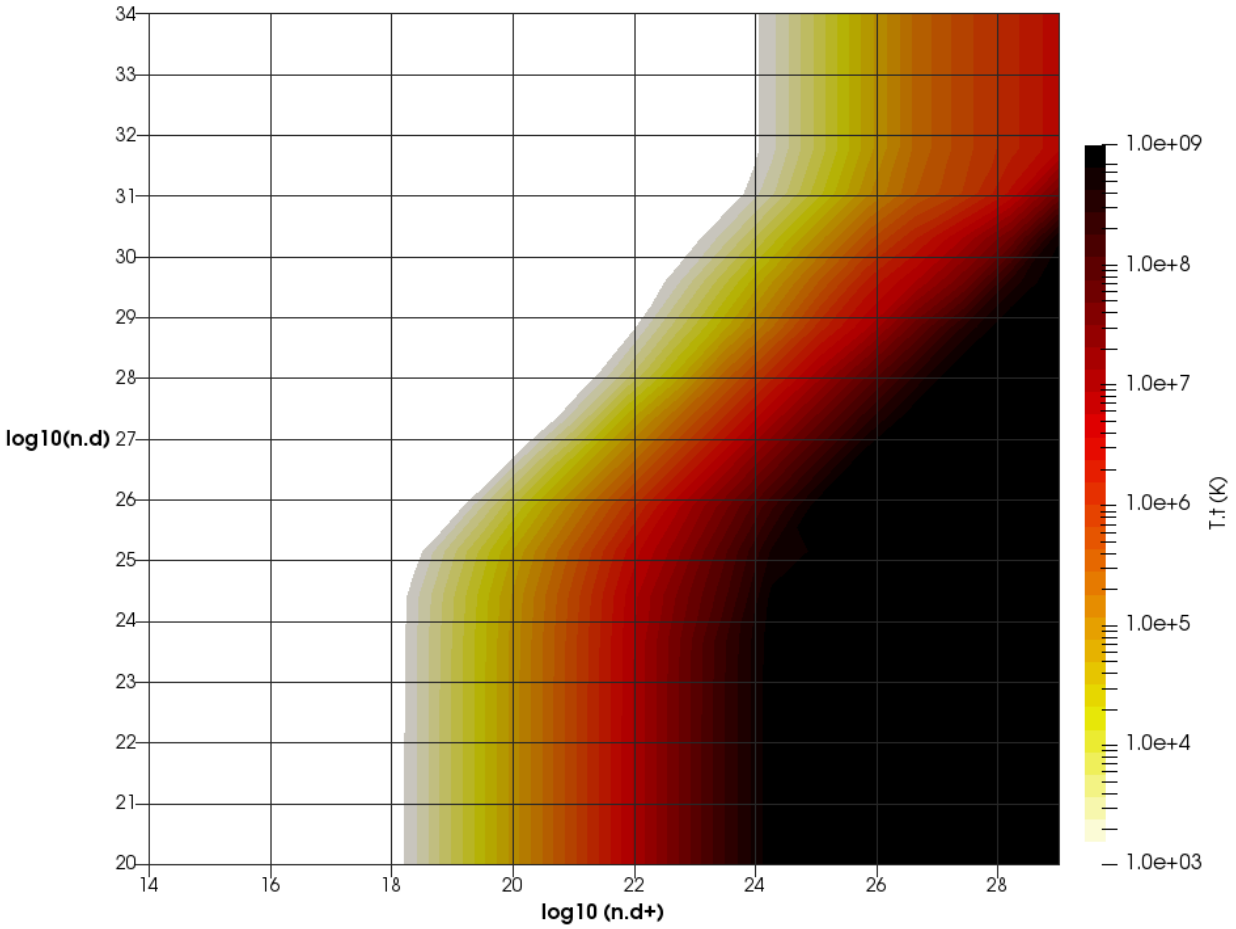

Figure 21. 0-D Model Fusion ignition landscape. Colors represent final temperature of background Deuterium (see right) versus target Deuterium density and initial energetic Deuteron density (generated via positron annihilation).

In some cases, increasing density of the target fuel can actually have a detrimental effect on the ignition, which could be due to interspecies elastic collision transfer. For example, at a positron implantation density of 1E21m^{-3} (D+ density of 1E20m^{-3}), as the target density increases above 1E26 m^{-3}, more and more of the energetic deuterons kinetic energy is transferred to heat the background Deuterium, but below temperatures required for fusion reactions.

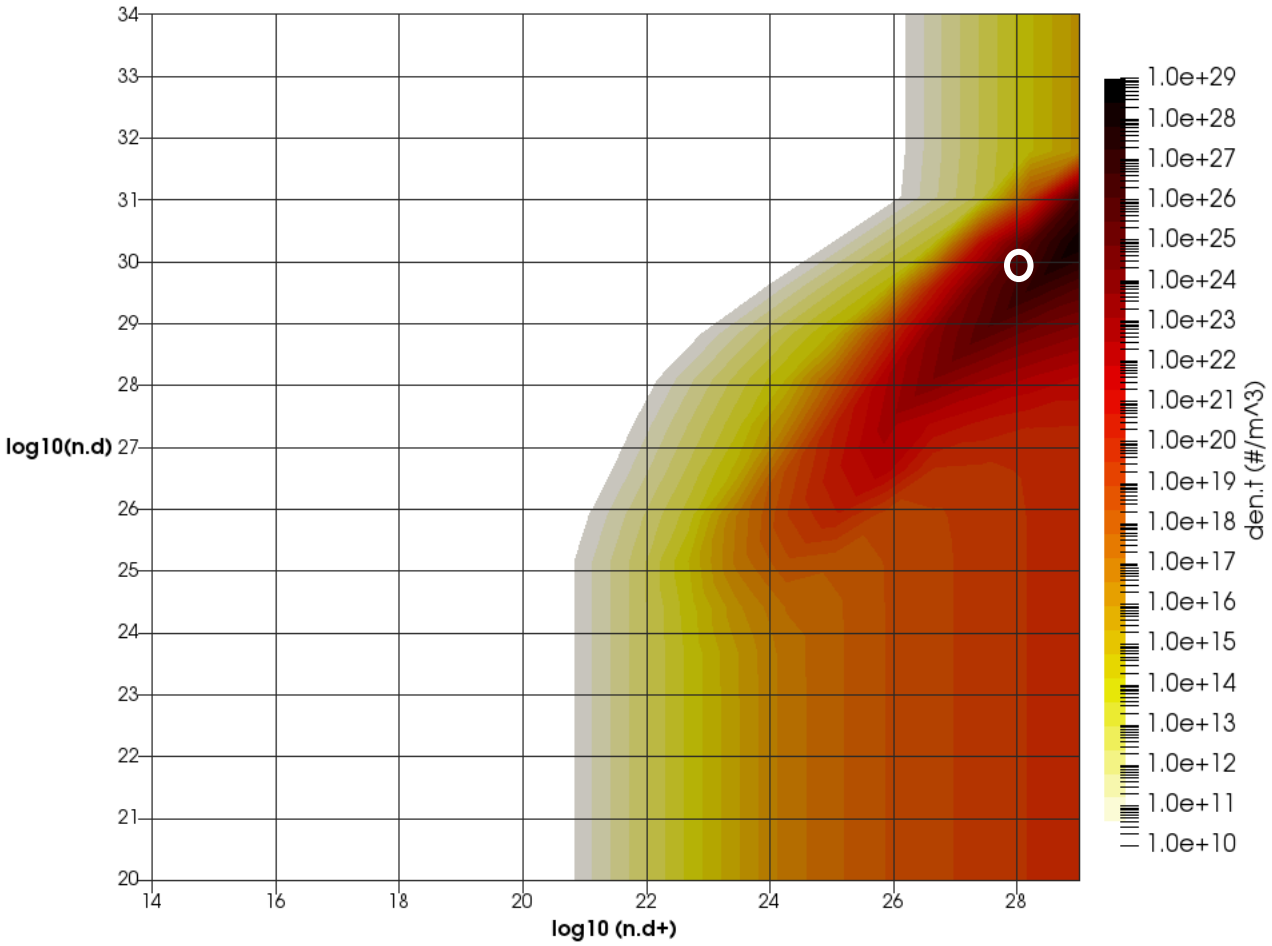

Figure 22. Tritium number density The results below show results obtained on a 20×20 *grid with* $(n_a)_{d^+} \in [10^{14}, 10^{29}]$ *and* $n_d \in [10^{20}, 10^{34}]$ m^{-3}.

Fig. 22 shows the number density of tritium. Presence of this species is indicative of fusion reaction occurring as it is not present in the cell at the start of the simulation. This gives us an idea of what the ideal background Deuterium and positron implantation density, since the burn fraction will be related to the Tritium density compared to the background Deuterium Density. For example, the white circle in Fig. 22 indicates a density regime where the burn fraction could reach 10%.

3.2.3 2-D Model

To make the simulation of ignition more realistic, a 2-D particle in cell environment (adapted Monte Carlo) was created with required collisional cross sections and demonstrated thermalization of energetic Deuterons from the initial positron pulse. The goal of this initial effort was to demonstrate

physical processes of the 2-D simulation over a short simulation time period (2,000ps). We continue to add relevant physics to the 2-D PIC simulation (radiation, ablation, ionization, fusion cross sections) in order to determine required positron pulse properties to achieve ignition. Details of the implementation of this model are found in Appendix D.

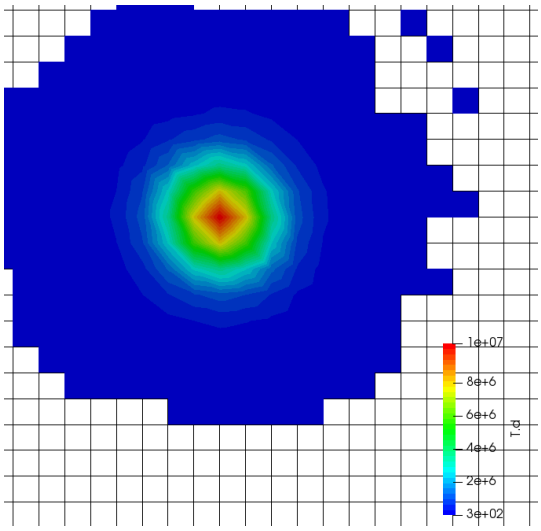

Figure 23. Temperature of neutral Deuterium with background density of 10^{26} m^{-3} after $2x10^{-9}$ sec simulation time.

Initial results indicate that collisions can transfer energy to the background Deuterium and give rise to temperature distributions like that in Fig. 23 above. However, the MCC solver struggles with densities higher than 10^{26} m^{-3}. A more robust energy solver is under development that will handle background densities up to 10^{32} m^{-3}.

Line Emission

While energy transfer from the hot ions to the neutrals is the primary heating mechanism, there are also some cooling mechanisms that need to be considered. The first one is radiative loss per line emission. Following the AMDIS model (see Appendix D), we were able to show temperature loss due to line emission in the 2-D model (see below).

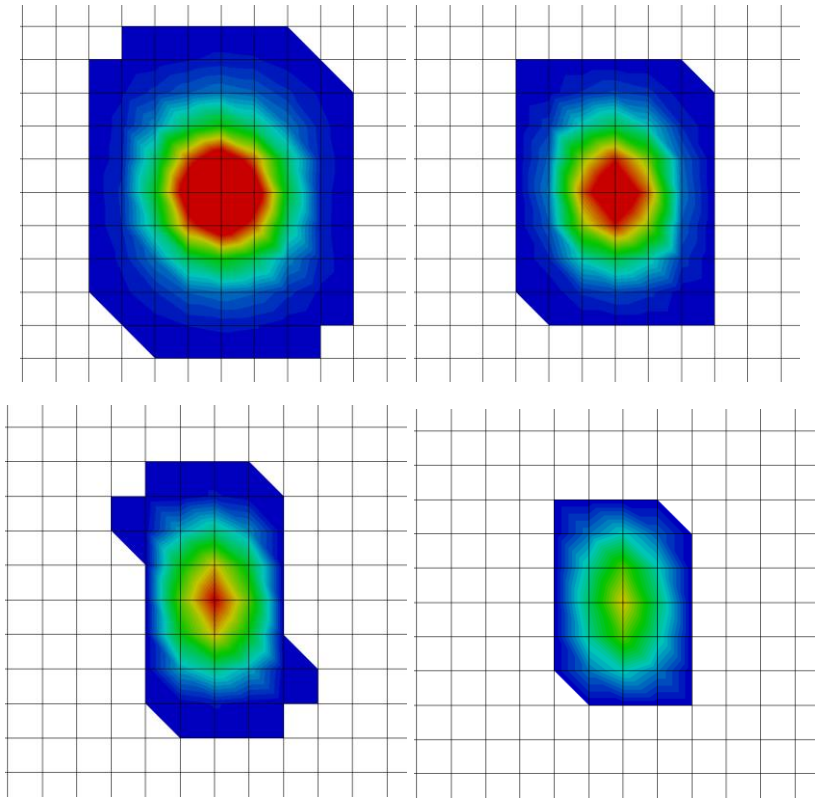

Figure 24. Decrease in D temperature due to line emission over $2x10^{-9}$ sec simulation. Here, line emission rates are exaggerated by 9 orders of magnitude for demonstration purposes.

Saha Ionization

Energy loss from ionization was also implemented, with ionization rate obtained from the Saha equation. One interesting result here is a total loss of energy in the high temperature core. This 'donut-hole' phenomenon is shown in Fig. 25 which could be the result of a non-physical energy solver artefact, or even the initiation of a plasma wave effect, although more work will be required to investigate.

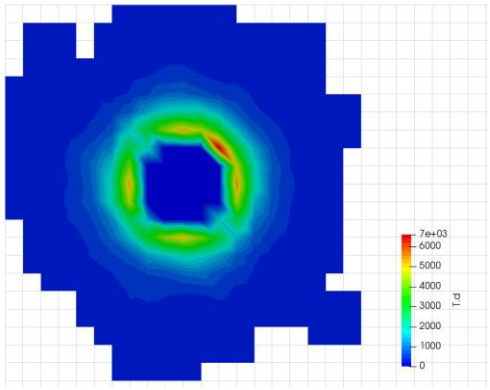

Figure 25. 2-D model results at simulation time of $2x10^{-9}$ sec, including Saha ionization energy transfer.

Fusion Reactions

Finally, support for modeling fusion was also included. Fusion is modeled as a chemical reaction, with rate given by the Bosch-Hale equation. Only the $D(d,n)\,^3He$ reaction is included so far. The generated helium is modeled as particles. Result from a test of the algorithm is shown in Fig. 26. Fig. 27 shows that the number of Helium particles continues to rise even after annihilation source is turned off, indicating a sustained fusion burn.

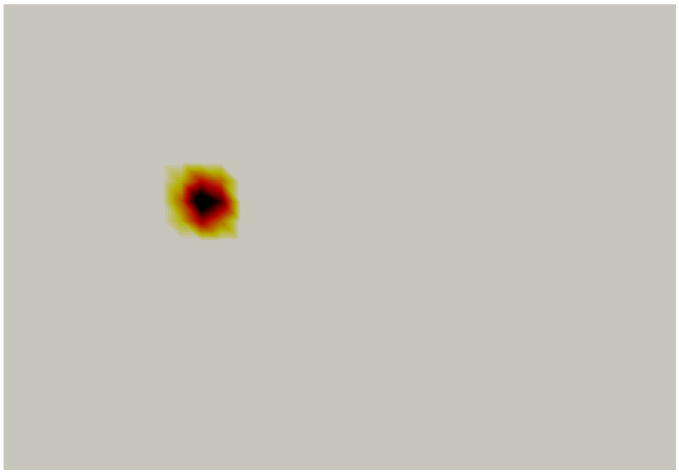

Figure 26. Creation of He-3 by fusion reaction, using artificial scaling of the fusion cross section due to the non-physical MCC energy solving routine at high densities.

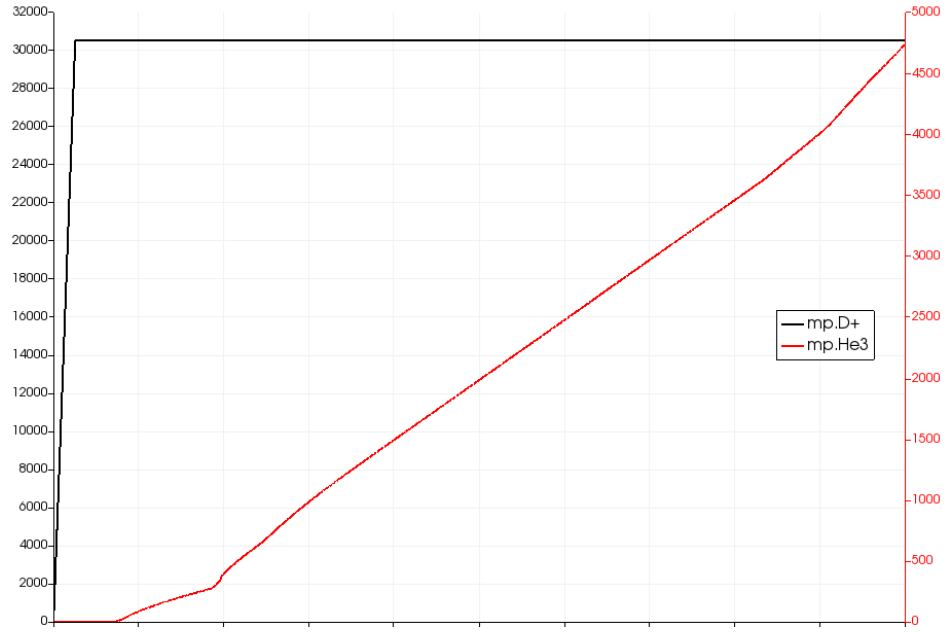

Figure 27. Time evolution of He-3 macroparticle count, using artificial scaling of the fusion cross section due to the non-physical MCC energy solving routine at high densities. The X-axis is simulation time (up to 2000ps).

Because of the issues with the MCC solver at extremely high background densities, we were required to run the 2-D simulations at the lower densities and artificially scale the Bosch-hale reactivities. Based on this, it is difficult to say that ignition was reached. An updated MCC energy solver will be able to answer these questions and is the focus of the next phase of Simulation work. That being said, these preliminary 2-D results were able to show relevant energy loss mechanisms and fusion reactions, and we are confident that future simulation work will demonstrate ignition characteristics so that target geometry and positron beam characteristics can be further optimized.

Ignition estimates from previous beam target fusion work, combined with Lawson criteria and 0-D Ignition model results (see above) give a rough estimate for the positron beam requirements for the RPP system. However, the parameter space for target and positron implantation density is so large that we are forced to choose a particular combination that makes sense. In this case, we chose a target density of 10^{30} m^{-3}, which is higher than normal solid hydrogen fuels, yet well below the ultra-dense regime($>10^{35}m^{-3}$) claimed in recent experiments [24-28]. This target density was also chosen to maximize burn fraction, based on the tritium production results in the 0-D simulations (see Fig. 22). Based on this analysis and the target fuel density and positron implantation density, we will assume that a 400ps pulse of 10^{11} positrons focused on to a beam spot of 50um diameter is required.

3.3 Positron Pulsed Beam System

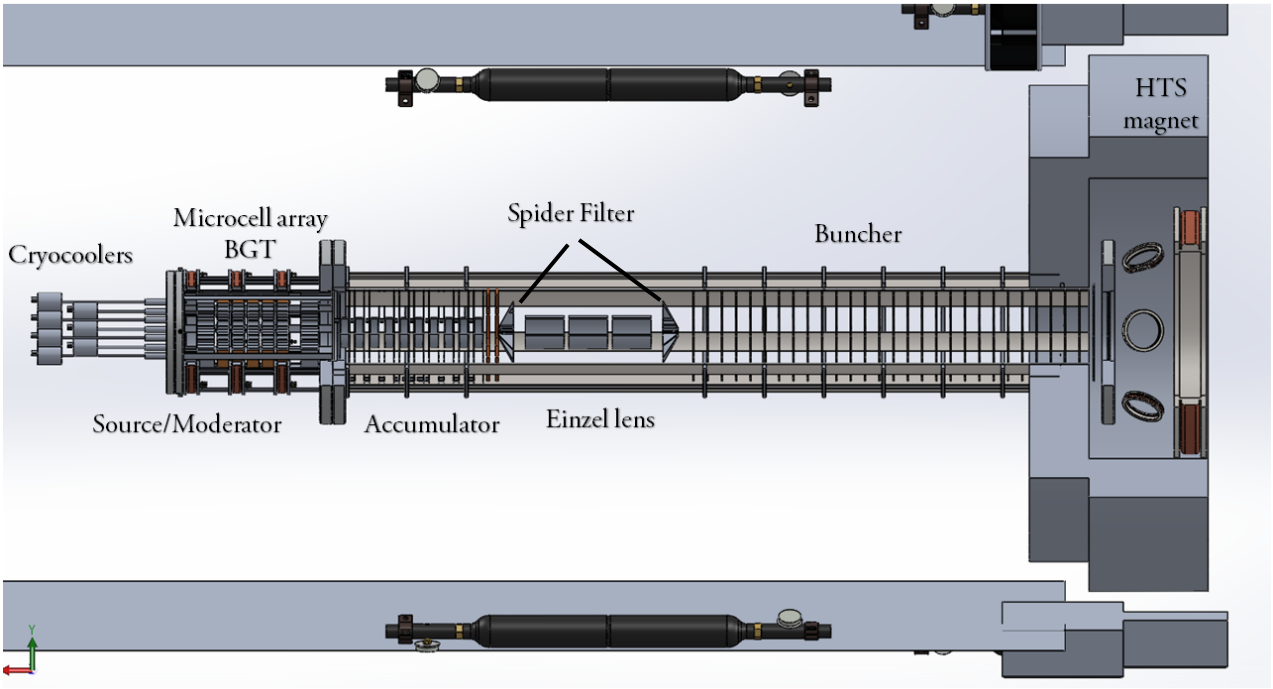

Figure 28. Sideview of the Positron beam system from the source on the far left to target on the far right.

The purpose of the beam system is to transform the continuously emitted positrons from a large area source into short pulses focused onto a small spot size. Because we are limited in the specific activity (Ci/g) of radioisotope and source area, the goal for each step of this process (moderation, accumulation, focusing, bunching) is to maximize the efficiency and intensity of the resulting positron beam.

3.3.1 Source and moderator stage

Can we design a stable Krypton source/moderator that can generate enough positrons/sec?

The positron source takes gaseous, enriched ^{79}Kr and deposits a thin layer on a cryogenic surface as shown in Fig. 29 (left). The Kr layer is isolated from the moderator using a thin-film window that is transparent to energetic positrons. By separating the source layer and moderator structure, we eliminate the positron mobility poisoning effect of Bromine, produced by ^{79}Kr decay [36].
Two significant challenges in this design maximizing the positron intensity, considering the possibility of self-absorption, while maintaining integrity of the frozen Kr source/moderator layers under irradiation from self-emitted gamma-rays and energetic positrons.

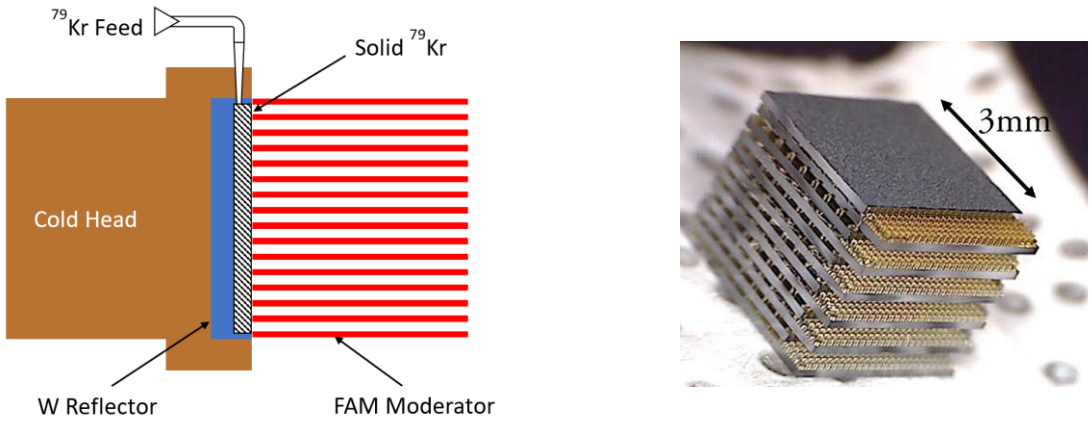

Figure 29. On the left, a diagram of Source/Moderator design and a SiC moderator array test article on right.

To determine the fraction of positrons that escape the frozen Kr layer, we performed PENELOPE simulations of positron implantation at average kinetic energy of 265keV, as seen in Fig. 30. To increase the number of positrons that are emitted towards the moderator, a high-Z (W, Ta) reflector is placed adjacent to the source layer, which is common in commercially available sources. PENELOPE simulations indicate the 40% of incident positrons will be reflected towards the moderator for a planar geometry using a Ta reflector.

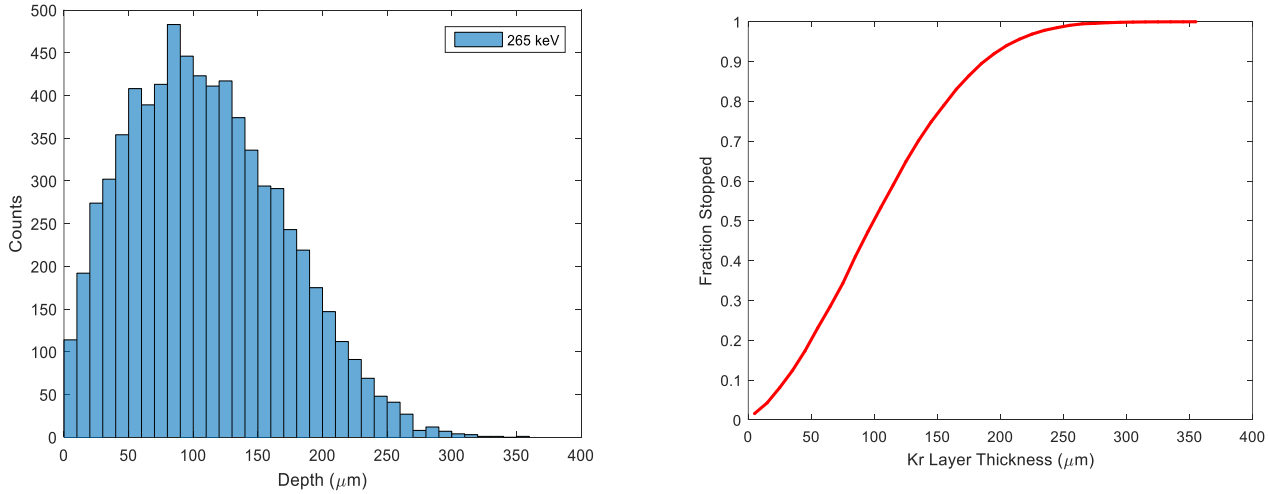

Figure 30: Positron implantation profile for solid Kr (2.826g/cm^3) at the mean positron energy of ^{79}Kr decay (265 keV).

The effectiveness of the high-Z reflection will be directly related to the thickness of the source material and ultimately the enrichment. A source layer of less than 200 um is likely optimal allowing positron emitted away from the moderator structure to be reflected through the Kr source layer with sufficient

kinetic energy to implant into the moderator structure. The application of an electric field, applied via surface charging or a planar electrodes/grids, may assist in driving positron diffusion to the source layer surface.

Source stability

We can estimate the heat deposition due to ^{79}Kr gamma rays emitted during decay using the NIST energy absorption coefficient of $\frac{\mu}{\rho} = 4.6\ x\ 10^{-2} cm^2/g$ [90] the density of solid Krypton $\rho = 2.8 g/cm^3$ and the Beer-Lambert law:

$$E_{abs}^{\gamma} = B_q E_{avg}^{\gamma} \left[1 - e^{-\left(\frac{\mu}{\rho}\right)\rho T}\right],$$

Where B_q is the source activity in Becquerels, $E_{avg} = 300keV$ is the average gamma ray energy. Likewise, the upper limit for positron kinetic energy that is deposited in the source layer is given by:

$$E_{abs}^{pos} = B_q E_{avg}^{pos} \beta,$$

Where E_{avg}^{pos}=265keV is the average positron kinetic energy from ^{79}Kr decay.
In general, the heat load due to the positrons will be greater than the gamma ray heat load, since for most realistic values of source thicknesses:

$$\frac{E_{abs}^{pos}}{E_{abs}^{\gamma}} \sim \frac{\beta}{\left[1 - e^{-\left(\frac{\mu}{\rho}\right)\rho T}\right]} \gg 1.$$

An example of the heat load characteristics of the source layer is shown in Fig. 31.

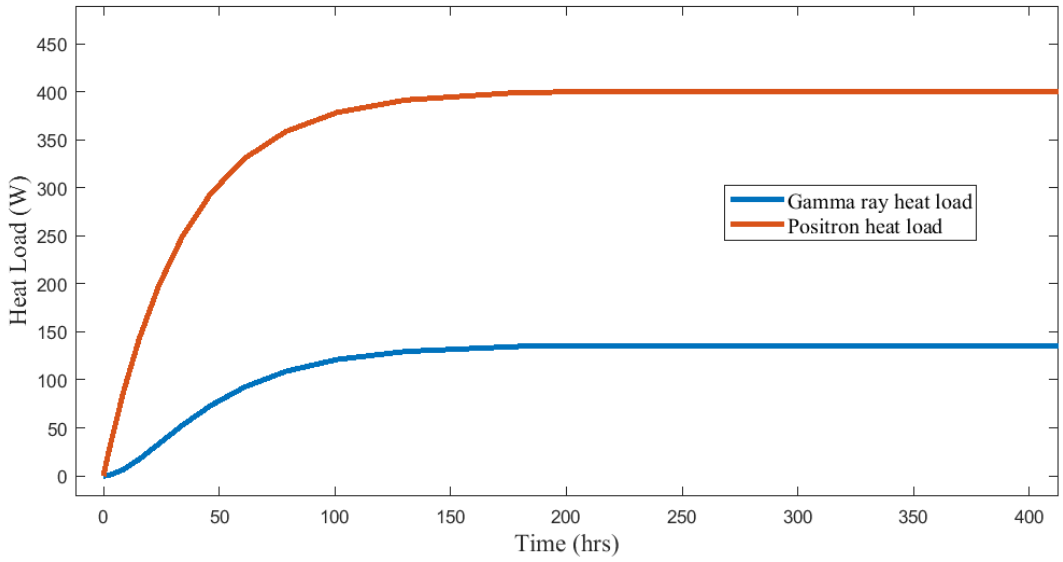

Figure 31. Heat load vs time for gamma rays and positrons for 100cm² square source area, 25% enrichment and maximum ^{79}Kr activity of 2.5E17 Bq.

The heat load to the source layer in this example is ~5W/cm^2. With the source layer temperature of <100K, radiative heat transfer away from the surface is minimal, therefore active cooling must be applied. Modern Pulse Tube Cryocoolers (see Fig. 32) could apply the required cooling power at cryogenic temperatures [91]. Additional cooling could also be applied flowing low temperature D_2 gas through microchannels in the coldhead structure.

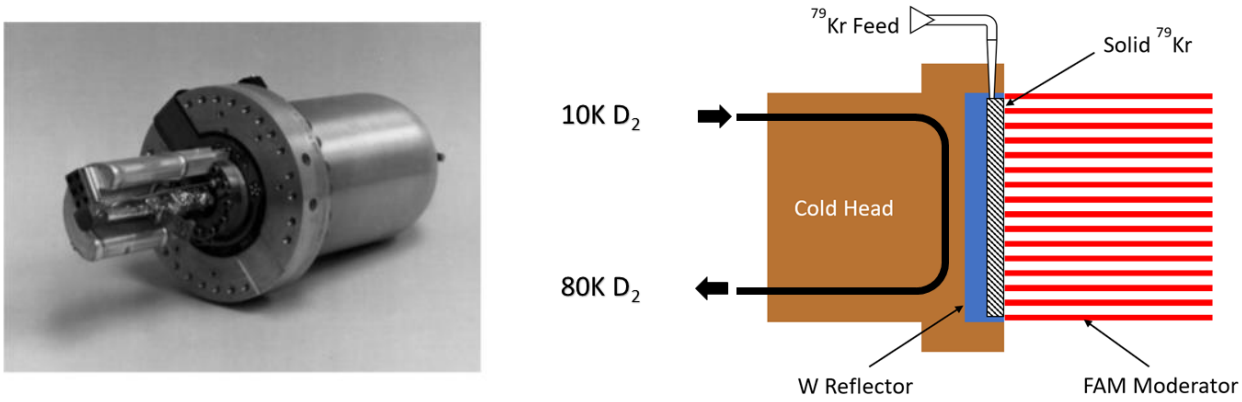

Figure 32. On the left, an example of a pulse-tube cryocooler for space applications, reproduced from [92] On the right, cryogenic D_2 gas assists in cooling the source stage.

With a molar heat capacity of K_c = 29J/(mol*K), the cooling capacity is estimated by:

$$\dot{Q} = K_c(T_1 - T_0)\dot{M}_u.$$

Using the inlet and outlet temperature estimates from Fig. 32, for cooling capacity to reach 500W, requires a D_2 flow rate of 2.5E-4 kg/s. In this system, the D_2 cooling may act as a passive system to dissipate the majority of heat load, while the cryocooler provides active cooling such that fine temperature control of the cold head can be achieved. In this way, depleted ^{79}Kr source layers can be evaporated and a new source layer can quickly be deposited.

3.3.2 Trap and Accumulator

Greaves et al [93] provides a detailed analysis and review of positron trapping and accumulator technologies required for production of large pulses. In general, our concept for the trap and accumulator follows current state-of-art designs which have produced the largest positron pulses to date [94,95].

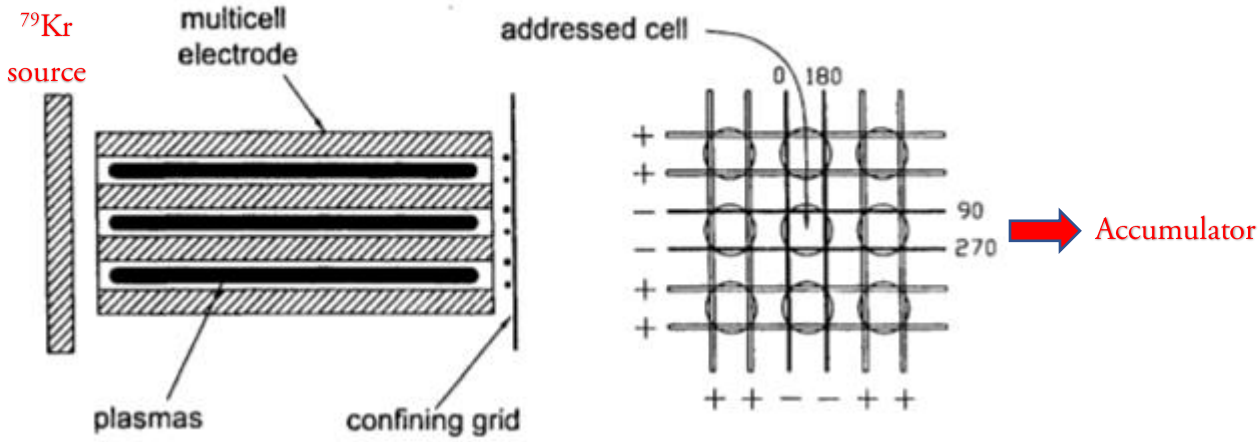

Figure 33. Showing multicell array concept and extraction scheme. Reproduced from [93], with added notation in red.

The positrons from the microcell array are loaded continuously into the accumulator stage until the required approximately 10^{11} positrons are accumulated in a plasma with approximate dimensions of 100mm length and 3mm radius and a plasma density of 3E8cm^{-3}. At field strength of 0.1T, the Brillouin limit is

$$n_B = \frac{B^2}{8\pi mc^2} = 5e10cm^{-3}.$$

In addition, for a non-neutral plasma (like a positron plasma), space charge repulsion will limit the maximum number of positrons that can be trapped for a given confining potential with a plasma radius $R_p$and wall radius R_w:

$$N_{max} \sim 7x10^6 \frac{V_e L}{\left[1 + \ln\left(\frac{R_w}{R_p}\right)\right]}.$$

For a confining potential of $V_e = 10kV$, L = 10cm, and $\frac{R_w}{R_p} = 2$ this corresponds to a space charge limit of 3E11 positrons.

Positrons generated from a radioisotope source have a high kinetic energy. They must be slowed down or moderated before trapping them is feasible. Once moderated, a positron beam can be trapped and cooled further. Typically, tetrafluoromethane (CF_4) is used as a cooling gas because of its high cooling rate. This allows the trapped positron cloud to thermalize rapidly providing for high repetition rates.

In this concept, positrons are produced in the beta decay of ^{79}Kr. For every positron produced, a ^{79}Br atom is also produced. As the breeding cycle produces more ^{79}Kr, it also produces more ^{79}Br. This

bromine can be exhausted, but it could also be used to produce CBr_4 or tetrabromomethane, which could be used as a trapping/cooling gas. An investigation of the chemistry required to produce CBr_4 is outside the scope of the current work but appears to require a multistep process. It remains to be seen if onboard generation of the trapping/cooling gas from the biproducts of beta-decay can significantly decrease the launch mass of the system.

Collisions between positrons and CBr_4 gas provide the energy loss mechanism required for trapping the moderated positrons inside cylindrical electrodes. The partial pressure of CBr_4 will be varied depending on the repetition rate of the positron accumulator and the activity of the ^{79}Kr source. By utilizing the Bromine created during the decay of ^{79}Kr, we avoid the requirement of carrying additional trap gas. In addition, CBr_4 is expected to have similar positron trapping characteristics as CF_4, a commonly used positron buffer gas [4].

Over the last two decades, positron trapping and cooling to produce a pulsed positron beam has become a standard practice using a buffer gas, or Surko-style, trap (BGT). Typically, nitrogen (N_2) is used in the first stage of the BGT to initially trap positrons before being cooled in the second stage of the trap using tetrafluoromethane (CF_4) [4]. Nitrogen was found to have the highest trapping efficiency when used with a solid neon moderator [110]. It has been suggested that CF_4 alone could be used as the sole gas in a compact BGT to both bunch and cool a positron beam [111]. Subsequent theoretical work confirmed trapping efficiencies could be obtained up to 90 % if the initial radioisotope (^{22}Na) positron beam was moderated by tungsten (W) [112]. They found that when using a CF_4 based BGT using a rare gas (Ne) moderated radioisotope-based positron beam the efficiency was reduced from 90 %, using W, to around 60 %.

Table 1: Comparison of molecular parameters and known positron trapping and cooling parameters.

Gas	State (NIST)	Trapping Efficiency [a](Greaves/Surko2002) [b](Marjanović2016) [c](Murtagh2012)	Relative Cooling Time (Greaves 2001 Phys Plas 8, 1879)	Normal Modes (cm^{-1})
SF_6	$^1A_{1G}$	7[a]	1 (0.36)	774, 642, 948, 616, 525, 347
CF_4	$^1A_1$	60[b],90[c]	3.33 (1.2)	909, 435, 1283, 631
CBr_4	$^1A_1$	-	-	267, 122, 672, 182
N_2	$^1\Sigma_g$	100[a], 20[b]	319 (115)	2359
CO	$^1\Sigma$	68[a]	5.83	2170

A comparison of various molecules for positron trapping and cooling is shown in Table 1. The trapping efficiency numbers are sensitive to the energy spread of the positron beam which are being trapped. Note that the experimental and theoretical results are not in agreement at this time, but work

is ongoing to bridge the gap. Experimental cooling times have been reported and are listed in Table 1. These results have been normalized; a larger cooling time is equivalent to a slower cooling rate. Finally, the ground state of each molecule and the molecules normal modes are tabulated [113] for comparison.

Tetrabromomethane is solid at room temperature. Thus, a CBr_4-based BGT would require the beam system to be operated at an elevated temperature (~100C) to prevent condensation. Experimental measurements would be required to determine the trapping efficiency and cooling time for CBr_4.

3.3.3. Charged Particle Optics Simulations

Can we design a positron beam system that provides the required intense, focused pulses of positrons to the fuel target?

To maximize the fusion ignition probability, a focused and controlled beam of positrons is required. In recent years, a number of positron beam systems have been designed and commissioned [4]. Low-power radio frequency techniques have been used to demonstrate precise control of ensembles of positrons [42]. Significant improvements have been made in the reliability of positron trapping systems using an array of techniques [61]. The generation of large instantaneous currents (i.e. Pulses) requires an accumulator to produce a large reservoir and a bunching technique for temporal compression [43]. The goal is to scale-down the accumulator, ion optics and buncher to fit into the size of the Reference Spacecraft Design, while satisfying the beam ignition requirement from section 3.2.

Two methods exist for creating a pulsed beam: chopping and bunching. In the chopping method, a continuous beam is passed through a chopper consisting of a narrow slit or system of slits. An off-axis RF cavity periodically deflects the beam through the slit to produce the pulsed beam. This mode of pulse production is rather inefficient, as the majority of particles are not transmitted.

Alternatively, one may create a pulsed beam by altering the velocity of a distribution of particles through application of electric fields. This method is called bunching and is a much more efficient means of creating pulses. We will focus the discussion of pulse creation on bunching methods because the beam flux is limited by source strength. The two main bunching techniques are RF-cavity [96] and time (or space)-dependent potential bunching methods [97].

Regardless, the desired result is a positron pulsed beam of <1ns FWHM. In most cases, creation of these pulses requires a modulation of the positron beam in phase space. Any modulation in the phase space of a particle distribution must follow Liouville's theorem, which states that the volume of a particle distribution in phase space remains constant.

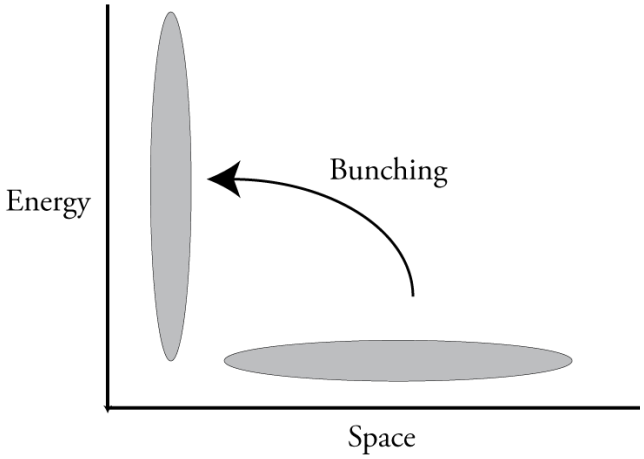

Figure 34. Phase space transformation

Traditionally, the most common method of bunching positrons for beam-based PALS experiments is through the application of RF cavity buncher(s) during the transport from source to sample [98].

Alternative methods of positron beam bunching were introduced by Mills [97], who described several methods of distorting the phase space volume of a positron pulse.

- Instantaneous quadratic potential
- Ideal voltage ramp

In the first method, low energy positrons along a length L are accelerated by a series of ring electrodes (see Fig. 35) with potentials applied to them such that they create a quadratic potential profile at t=0 along the axis of the beamline $V(z,t) = \frac{k}{2} z^2 H(t)$.

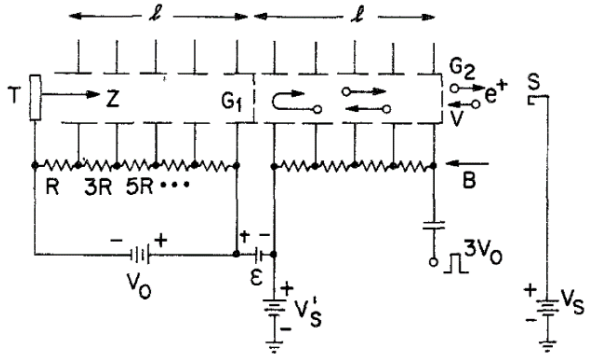

Figure 35. Mills quadratic potential bunching scheme. Reproduced from [97]

Using this method, it can be shown that for a given maximum accelerator voltage V_0, the timing spread of the positron bunch when it reaches the sample T is given by [93]:

$$\Delta t = 2\sqrt{\frac{m}{e}}\frac{L\sqrt{\langle W_{\parallel}\rangle}}{V_0}.$$

Using this equation, with L=5cm, $\langle W_{\parallel}\rangle = 40\ meV$ and $V_0 = 200\ V$, one should be able to achieve a timing pulse of ~240ps.

In addition to temporal compression (bunching), the positron beam must be compressed radially to a small diameter on the fusion target and thereby increase the density of positrons at the target. In our

compression and focusing scheme, the moderated positrons are magnetically guided into a microcell array buffer gas trap with rotating wall compression that feeds a low-pressure accumulator stage. The low-temperature positron plasma in the accumulator stage is 'dumped' into a combination of magnetic and electrostatic compression, and finally through a Mills-style quadratic bunching stage. An overview of this scheme is shown in Fig. 36.

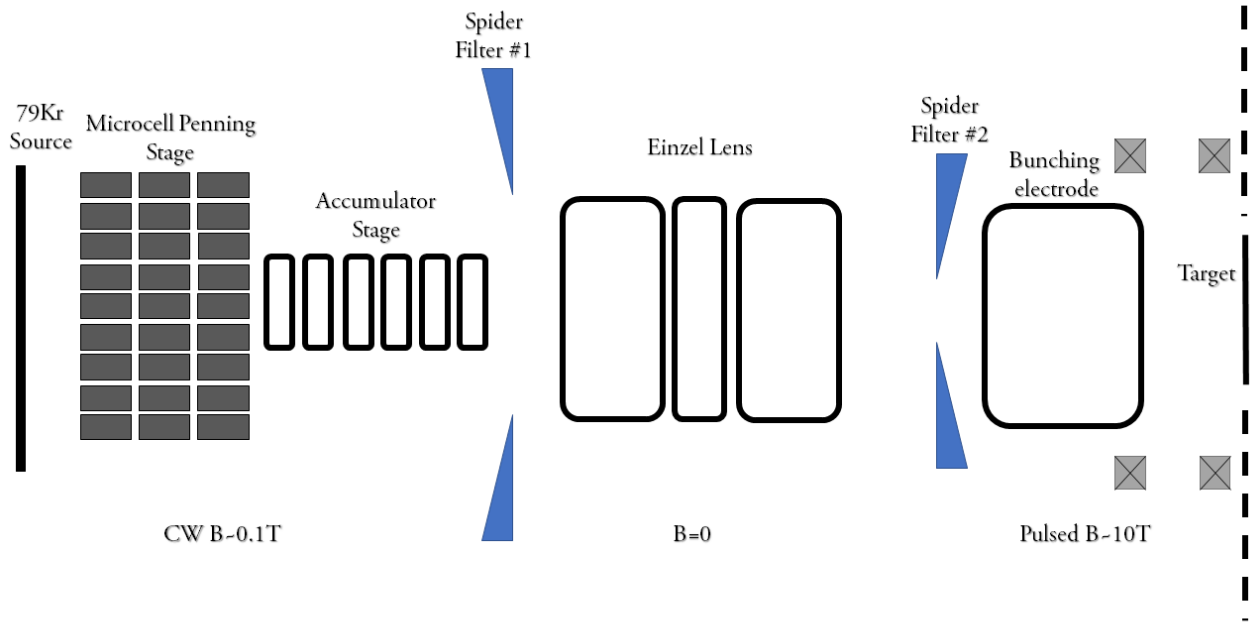

Figure 36. An overview of bunching and focusing scheme for producing the required temporal and radial compression of the positron beam. The entire beam system length is 2m.

Because of the high magnetic field requirements of the moderator and large source area, single stage magnetic adiabatic compression would require unrealistically high magnetic fields at the target, since adiabatic compression is proportional to the square root of the ratio of magnetic fields: $\frac{r_1}{r_2} = \sqrt{\frac{B_1}{B_0}}$. Our beam system design takes advantage of recent advances in electrostatic beam extraction using mu-metal 'Spider' filters. Such systems are based on rapid changes to magnetic field over small distances, such that the adiabatic parameters, Υ_1 and Υ_2 are much larger than unity:

$$\Upsilon_1 = \left|\frac{\rho_L \nabla \cdot \boldsymbol{B}}{B}\right| ,$$
$$\Upsilon_2 = \left|\frac{1}{\omega_B B}\frac{\partial \boldsymbol{B}}{\partial t}\right|.$$

'Spider' filters have been shown to allow charged particle beams to be extracted from high magnetic field regions with very high efficiency (>90%). Previous work demonstrated a grid of high-permeability 'mu-metal' grid arranged in radial spoke pattern [99,100] (see Fig. 37).

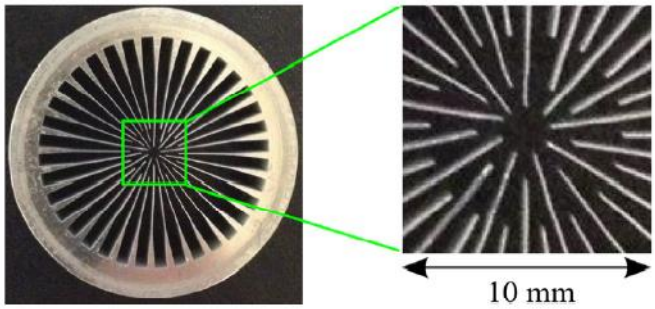

Figure 37. An example of 'mu-metal' radial spoke pattern Spider Filter. Reproduced from [100].

The SIMION simulation combines the Spider filter with an Einzel lens for electrostatic focusing. The magnetic field is programmatically defined based on a combination of solenoid fields [101]. This hybrid approach to beam focusing/pulsing using both magnetic adiabatic compression and electrostatic focusing is expected to generate the required intense positron pulses at the target.

The charged particle optics of the positron beam were simulated using software, SIMION. These simulations began at the accumulator stage, assuming that a Penning-Malmberg accumulator w/ rotating wall compression [44] will be sufficient for primary cooling and loading of the accumulator. The source, microcell array trap and accumulator are surrounded by electromagnets that produce a moderate strength longitudinal magnetic field (1000 Gauss). This field is used for the ExB moderator extraction process (see Appendix C) as well as transverse positron confinement.

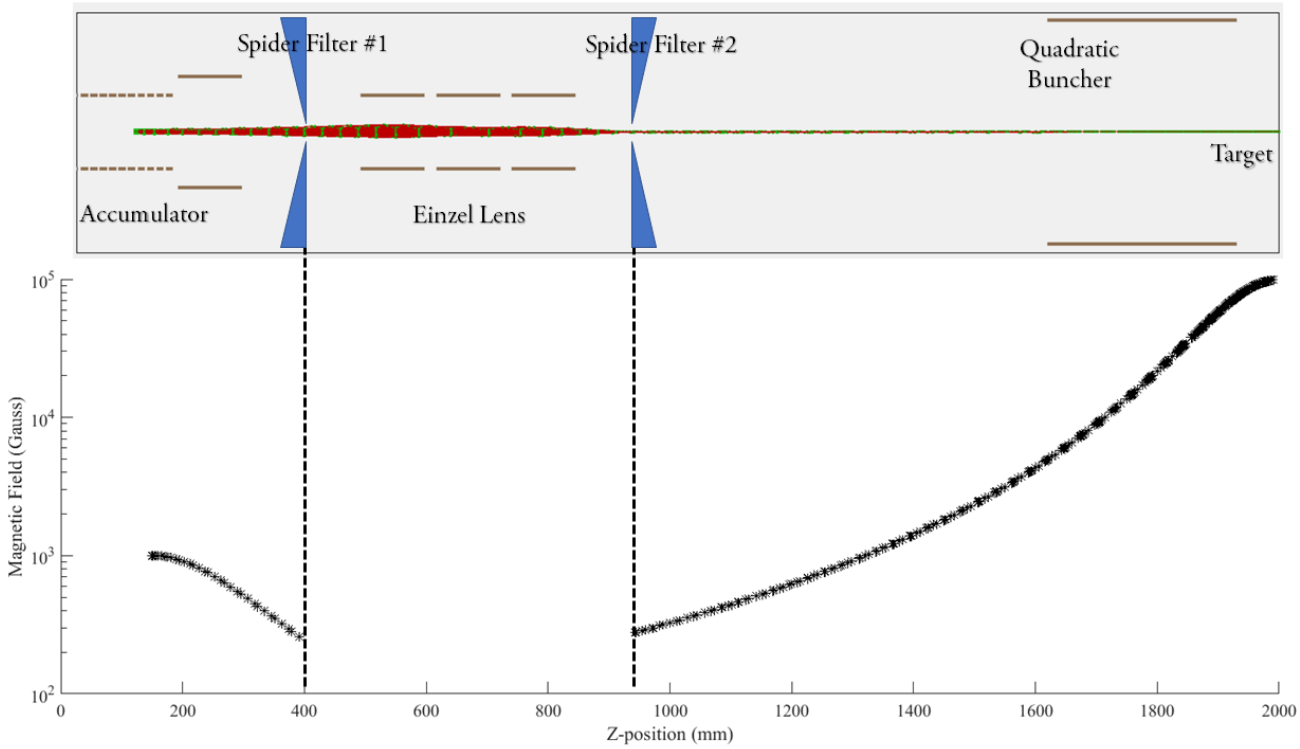

Figure 38. SIMION setup for charged particle optics simulations (above) and Magnetic field strength on axis.

In this hybrid approach to beam compression, the positron cloud in the accumulator exits towards the first Spider filter, expanding adiabatically as the field strength reduces (see Fig. 38). At 400mm the magnetic field drops to zero at the first Spider Filter, and the beam enters the Einzel Lens. At the focal length of the Einzel Lens (~950mm), the second Spider Filter terminates the magnetic field generated by solenoids near the target (at 2000mm) and the positron beam follows those field lines towards the target, undergoing adiabatic compression. A quadratic buncher between 1600mm and 1950mm applies the final accelerating potential to the positron bunch.

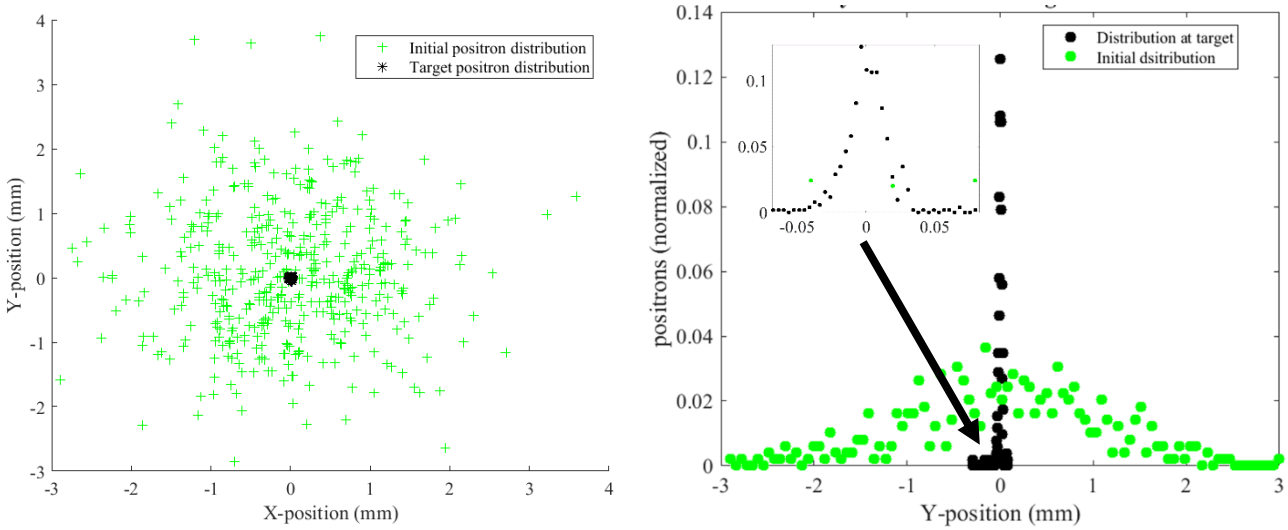

Figure 39. SIMION simulation results for hybrid electrostatic and magnetic focusing scheme, without quadratic bunching stage and without charge repulsion effects. The beam FWHM is approximately 25um. Initial beam dimensions are 100mm length, Gaussian radial distribution with FWHM=2mm.

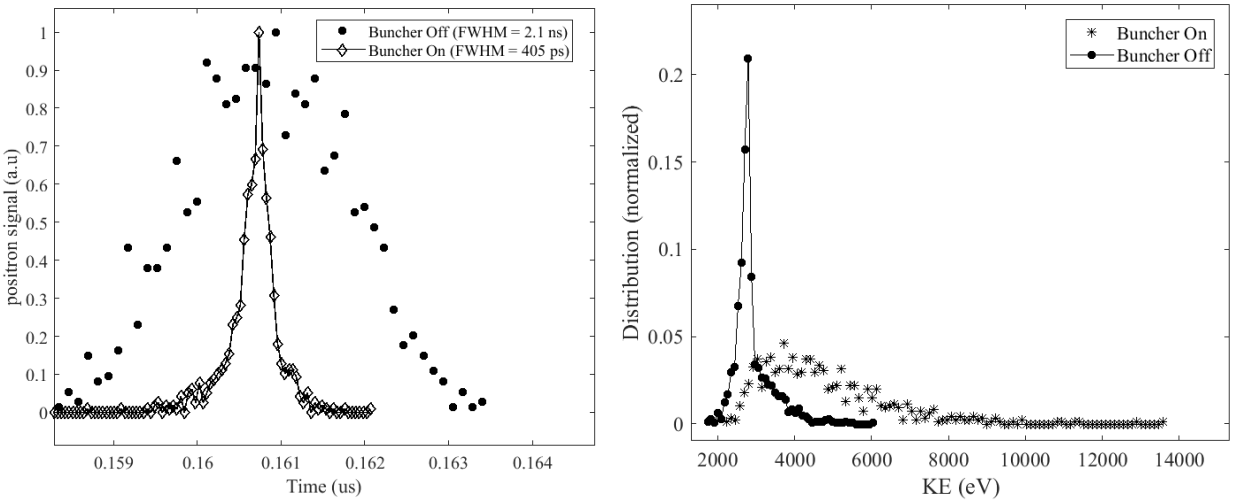

Figure 40. SIMION simulation results including the Mills Quadratic bunching stage.

From Fig. 39 above, we see that beam temporal and spatial compression is accomplished, bringing the beamspot from mm's initially at the accumulator exit down to <50um diameter FWHM at the target. In Fig. 40 (left), we see the effect of the buncher electrodes, which reduce the pulse width from 2ns FWHM down to 405ps. Fig. 40 (right) also shows the increase to average KE and KE deviation due to the instantaneous quadratic potential applied to the positron bunch. The increase in KE energy of the positron pulse due to the bunching electrodes will need to be taken into account in the target and

substrate geometry, as the positron implantation profile (and ignition characteristics) will depend on this initial KE distribution.

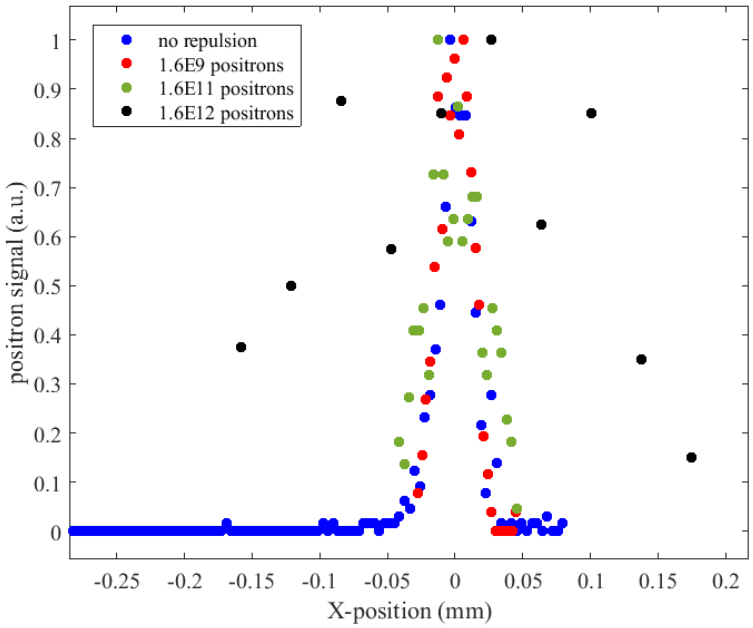

Figure 41. SIMION simulation results including charge repulsion effects.

Fig. 41 above shows the effect of charge repulsion in beam compression dynamics. The beamspot diameter is relatively unchanged up to a positron pulse of 1.6E11 positrons. However, when the positron pulse number is increased to 1.6E12, the beamspot expands due to charge repulsion to more than 100um. For this geometry and particular set of electrode potentials, this puts a limit on the maximum number of positrons per pulse, although further optimization of magnetic field characteristics and electrode geometry and potential could relax this limit further.

3.4 Breeding of positron-emitting radioisotope (^{79}Kr)

Can we efficiently capture fast neutrons and enrich enough ^{79}Kr to generate sufficient number of positrons?

3.4.1 Fuel Cycle

The ^{78}Kr(n,g)^{79}Kr reaction cross section is used to generate the positron emitting radioisotope. In order to breed sufficient positron radioisotope, we need to ensure that enough of the fast neutrons emitted isotopically (4π) from DD fusion events are captured in the nozzle area surrounding the fuel target. While ^{79}Kr is not technically the propulsion system fuel (Deuterium is the fuel), the production of

^{79}Kr is so essential to the propulsion mechanism that it is included in the fuel cycle analysis (see below)

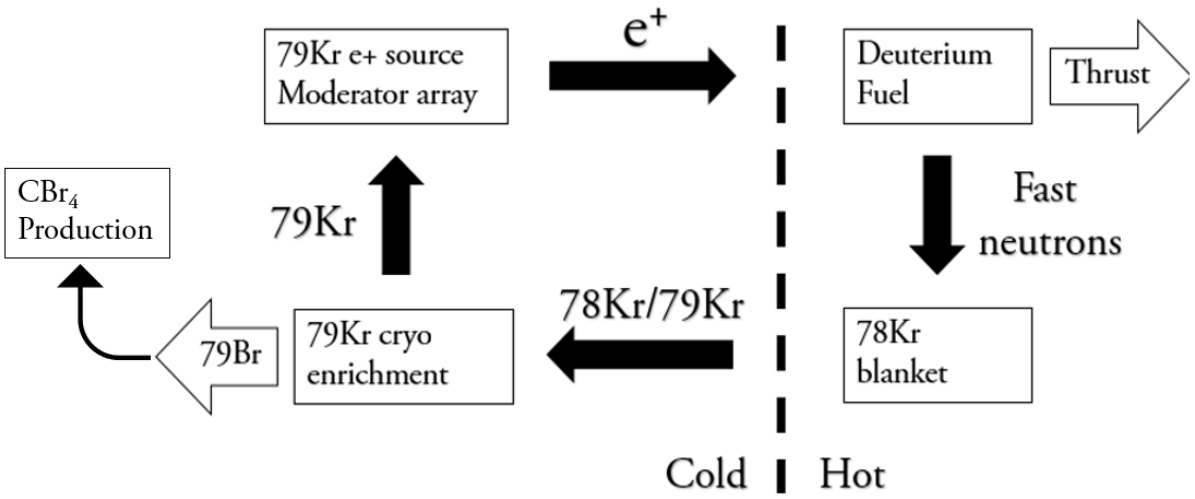

Figure 42. The ^{79}Kr breeding cycle (e+ indicates positron).

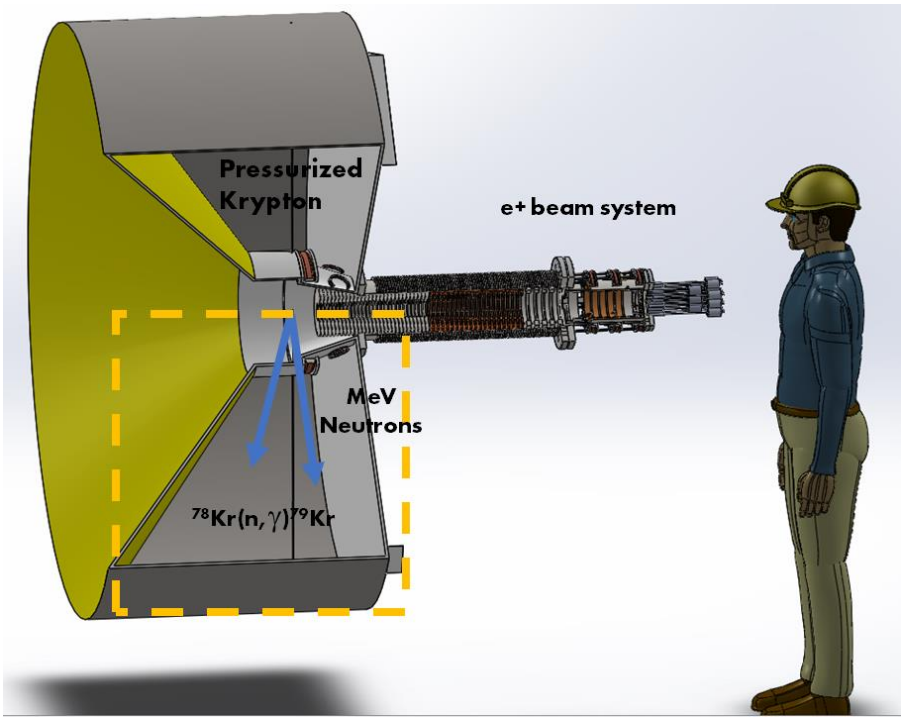

Figure 43. An overview of the first blanket design using high pressure Kr.

An initial nozzle design covered approximately 2π of the fuel target with a 1-meter thickness gaseous Krypton layer (see Fig. 43). Later iteration of this design included a 'hot section' and 'cold section' with varying Kr density but maintained the overall shape that maximizes solid angle to the fuel target.

Monte Carlo N-particle Code (MCNP) [41] (Version 6.2 with ENDF/B-VII.1 Cross Sections) was used to refine the positron source breeding estimates by determining neutron transport characteristics surrounding the engine core. The results will determine initial mass scaling of engine nozzle components, Kr blanket and ^{79}Kr enrichment subsystems.

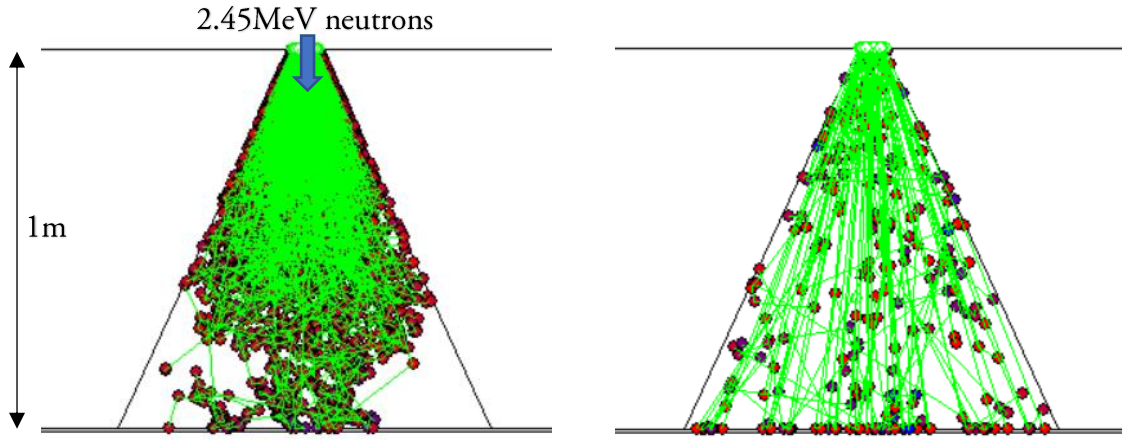

Figure 44. MCNP simulation results for 100atm (left) and 10atm (right) pressurized Kr blanket. While the 100atm blanket offers high neutron capture probability, it requires more than 1400kg of Kr. The 10atm blanket offers lower neutron capture probability (13%), but uses an order of magnitude less Kr.

We used MCNP neutron propagation simulation with relevant capture cross section to demonstrate that we could capture a significant fraction of fast neutrons with a realistic amount of gaseous Kr at high pressure (10 bar).

In these simulations, we found the neutron capture probability, η_c, to scale with the number density and path length: $\eta_c \sim 0.013\ atm^{-1}m^{-1}$. This scaling will be beneficial in determining optimal blanket sizing for a given mission application and were used in fuel cycle system model (MATLAB) which will refine system performance estimates and mass estimates.

3.4.2 Breeding analysis

The ^{79}Kr positron source breeding follows the linear set of coupled differential equations, with N_{78} and N_{79} representing the amount of ^{78}Kr and ^{79}Kr in grams, respectively:

$$\frac{\partial N_{78}}{\partial t} = -(neutron\ capture) = -A * N_{78}N_{79}\ , \quad (1)$$

$$\frac{\partial N_{79}}{\partial t} = +(neutron\ capture) - (radioisotope\ decay) = A * N_{78}N_{79} - \lambda N_{79}\ . \quad (2)$$

Where λ is the decay rate (λ=8E-6 s^{-1} for ^{79}Kr) and A is a constant describing positron beam production, transport to fusion target, fusion characteristics and neutron capture properties. If we define the number of neutrons generated per incident positron as n_p and the probability of neutron capture in the ^{79}Kr blanket per incident neutron as η_c, then equation 2 becomes:

$$\frac{\partial N_{79}}{\partial t} = \lambda N_{79}\{\ln(2)\,\beta\varepsilon_m T n_p \eta_c \Omega N_{78} - 1\}\,. \qquad (3)$$

With β the branching ratio for positrons emitted per decay of ^{79}Kr [36], T representing the accumulator and transport efficiency, ε_m the moderator efficiency, and Ω the solid angle of the ^{79}Kr blanket. From equation 3 we see that the breeding requirement is:

$$\ln(2)\,\beta\varepsilon_m T n_p \eta_c \Omega\, N_{78}^0 > 1\,, \qquad (4)$$

Where $N_{78}^0$is the initial amount of ^{78}Kr. Equation 4 does not explicitly depend on the initial amount of ^{79}Kr, however, it is likely that the accumulator and transport efficiency, T, will drop to zero at arbitrarily small values of N_{79}^0, due to finite trap and accumulator lifetimes as well as limitations to the ^{79}Kr enrichment process. To include this in our mathematical model, we will assume that accumulator and trap efficiency depends on the amount of ^{79}Kr, such that $T = [1 - e^{\frac{-N_{79}}{\kappa}}]$. In this model, κ corresponds to the amount of ^{79}Kr that will produce the required number of positrons to reach ignition in the target (N_{pos})within the trap/accumulator lifetime, τ,

$$\kappa \equiv \frac{M_u N_{pos}}{\ln(2)\beta\varepsilon_m a_v \lambda \tau},$$

where M_u is the molar mass of ^{79}Kr and a_v is Avogadro's number. A realistic upper limit for trap/accumulator lifetimes is on the order of 100 secs based on previous work with low pressure accumulator stages [110,111]. Given the branching ratio of ^{79}Kr of $\beta = 0.067$ and $N_{pos} = 10^{11}$ per pulse (see section 3.2) the transport efficiency, T, rises rapidly to unity when the amount of ^{79}Kr is above 10 μg.

Similarly, the propulsion system cannot support an arbitrarily large amount of ^{79}Kr due to several factors (heat load and neutron damage in source/blanket/nozzle/magnets, positron cooling/compression/ bunching timescales, Kr isotope enrichment throughput, etc.). The first limitation will likely be reduction in moderator efficiency when the thickness of ^{79}Kr-rich source layer approaches the thermalization length of the energetic positron emitted during decay of ^{79}Kr. The average positron energy in ^{79}Kr decay is 265 keV. Monte-Carlo simulations of thermalization in Krypton suggest that source thickness above 200 μm will suffer self-absorption and reduction in moderation efficiency. Therefore, our model for moderator performance follows $\varepsilon_m = \varepsilon_0[1 - e^{\frac{-C}{N_{79}}}]$. In this model, C corresponds to an amount of ^{79}Kr that produces a source thickness of 200 μm and ε_0 is the baseline moderator performance. Since the source area is fixed, the value of C depends only on enrichment, α,

$$C \equiv (\rho_s V)\alpha,$$

where ρ_s is the density if solid Kr and V is the source volume. Combining these models gives us the range of parameters (^{79}Kr amount, heat loads, positron pulse repetition rate, etc.) in which of operating propulsion system will perform, as shown in Fig. 43.

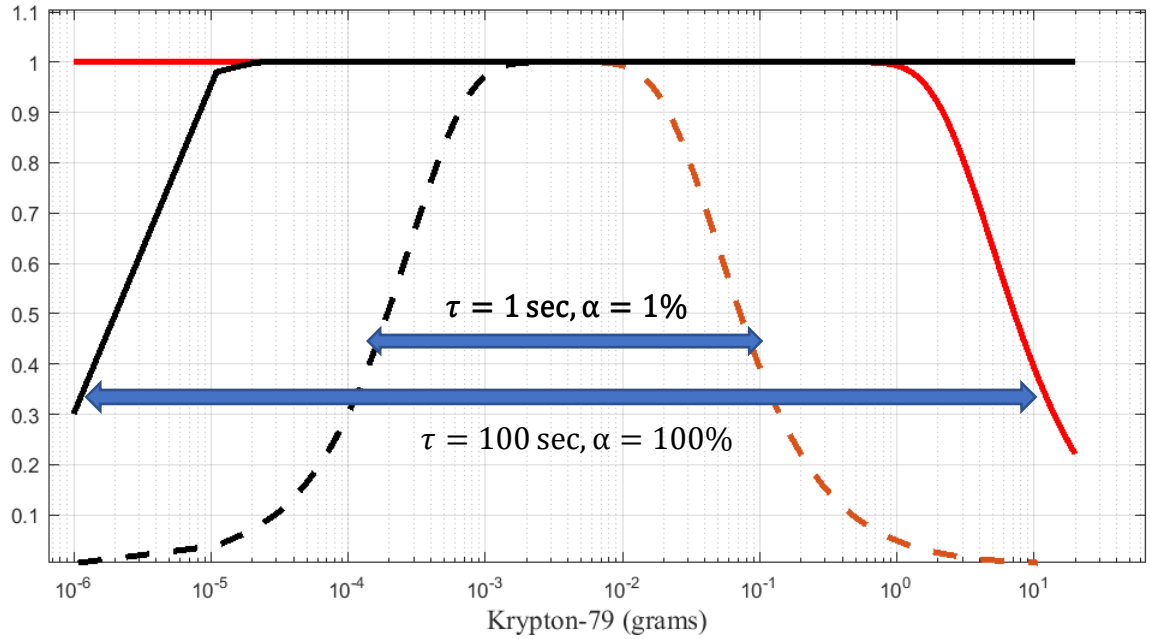

Figure 45. A model for transport efficiency, including trap and accumulator lifetimes (black lines), The red lines are a model of source moderation efficiency $\frac{\varepsilon_m}{\varepsilon_0}$ *based on a 100 cm² source area.*

^{79}Kr Seed

From the breeding analysis above, an initial amount of ^{79}Kr up to 1ug (~1.2 Ci) must be generated on the ground using a neutron source. Here, we consider a fission reactor core with thermal neutron flux of 10^{15} ns^{-1}cm^{-2}. Mills calculated that 60 mL of standard temperature pressure (STP) isotopically pure ^{78}Kr would produce a ^{79}Kr source with a saturation activity of 2.7Ci/cm^2 for a 200um thick source layer. With the RPP source area between 100-500cm^2, it is likely that a fission reactor neutron source could feasibly produce the required ^{79}Kr(>>1Ci) seed for the RPP source breeding fuel cycle.

3.4.3 ^{79}Kr Enrichment

The RPP system relies on a very high activity ^{79}Kr source distributed over a relatively small area (100-500cm2). For positrons to escape this source layer, the thickness of the of the source layer must be minimized (<300um). Based on the finite size of the source area, isotopic enrichment of the ^{79}Kr must

take place prior to deposition of the source layer to reach the very high source activities (>10^{17} Bq) required at full thrust operation.

In general, isotope separation mechanisms take advantage of the slightly different thermodynamic or mass/charge properties of isotopes of a similar element. Most of these technologies were developed in the mid-20th century for the purpose of separating fissile Uranium or Plutonium isotopes [130]. The performance of an isotope separation method is described by the separation factor, a, is ratio of molar concentration ratios of two isotope species, $N_1$and N_2, before and after the enrichment stage(s):

$$a = \frac{(N_1/N_2)_{after}}{(N_1/N_2)_{before}}$$

Centrifuge based isotope separation is the most common method of separation of gas-phase isotopes, however, the inherent mechanical support structure, drive mechanisms and high number of stages (due to the low enrichment factor) make this approach unreasonable for a spacecraft application. Calutron separation and ion-cyclotron resonance (ICR) separation are methods that utilizes the 1.3% difference in charge-to-mass ratio of ^{78}Kr and ^{79}Kr. A strong magnetic field separates the isotopes based on slightly different ion trajectories. While these methods offer very high enrichment factors in a single stage, the practical limitations to beam current and massive permanent magnets required reduce the utility of the Calutron and ICR methods in a spacecraft application [102].

More recently, tunable high-power lasers have opened up the possibility of using laser photons to selectively excite hyperfine or molecular rotational states [103]. Unfortunately, these laser isotope separation concepts include an ion optics and magnetic selection components which will suffer from the same limitations described above (beam current, magnet mass).

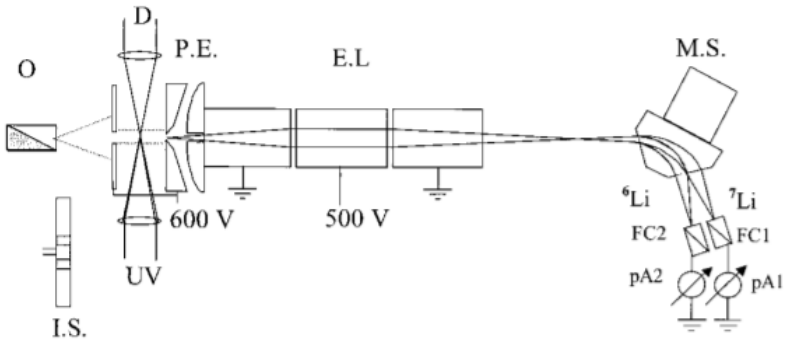

Figure 46. Laser Ionization Separation (LIS) of Lithium isotopes, including annotation for ion optics (E.L) and magnet selector (M.S). Reproduced from [103].

Another demonstrated method of isotope separation is through DC Discharge in narrow capillaries across cathode and anode structures. In this method, heavier isotopes become enriched in the cathode region, while lighter isotopes are enriched at the anode [104,105]. This method offers higher separation factors compared to centrifugal and thermal diffusion methods, while also offering much higher throughput. Finally, a novel method of isotope separation described by Mills [35,36] has not been realized experimentally, yet offers extremely high separation factors (a >10) in a single stage. In this concept, a carrier gas oscillates in sync with heater elements to produce binomial distribution based on the difference in sublimation rates between ^{78}Kr and ^{79}Kr [106].

Here, we compare these two concepts for enrichment of the ^{78}Kr/^{79}Kr mixture required for production of the intense positron source.

DC Discharge Method

In this method, a medium pressure discharge (3-15 Torr) is setup in a long capillary tube. The friction force created between ionized and neutral components of the discharge, known as 'ion wind', is responsible for the isotopic redistribution in the discharge capillary.

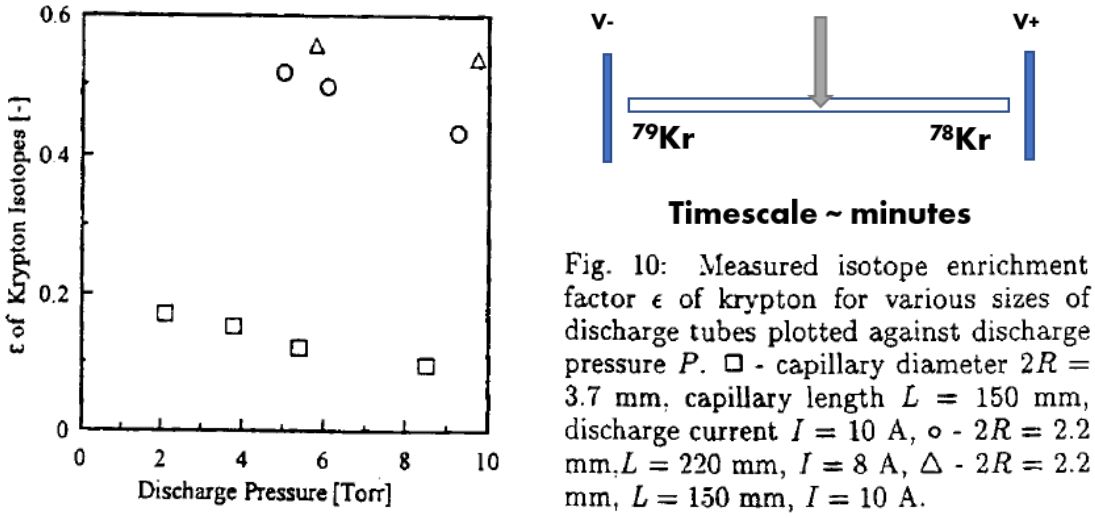

Fig. 10: Measured isotope enrichment factor ϵ of krypton for various sizes of discharge tubes plotted against discharge pressure P. □ - capillary diameter $2R$ = 3.7 mm, capillary length L = 150 mm, discharge current I = 10 A, ○ - $2R$ = 2.2 mm, L = 220 mm, I = 8 A, △ - $2R$ = 2.2 mm, L = 150 mm, I = 10 A.

Figure 47. Krypton isotope enrichment factors in various DC Discharge capillaries. Here, the enrichment factor, ϵ , is defined as $\epsilon = a - 1$. *Reproduced from [104]*

From previous work on DC discharge separation, the separation factor was found to be linear with discharge current and follow the proportional relationships:

$$\epsilon \propto \frac{\Delta m}{m}\frac{n_i e E_z \ell}{nkT} \ ,$$

Where $n_i$and n are the ion density and neutral density, respectively. The fractional isotope mass difference, $\frac{\Delta m}{m} = .075$, for the ^{86}Kr / ^{80}Kr isotope mixture in Fig. 47, while $\frac{\Delta m}{m} = .013$ for the ^{78}Kr / ^{79}Kr mixture considered in this propulsion concept. While the smaller mass difference will reduce the separation factor by a factor of 6, we can also increase the length of the discharge capillary, ℓ, by a similar factor in order to maintain the same separation factor.

If we assume an ideal cascade separation system can be constructed from individual DC discharge elements described above, the total number of stages required is given by:

$$N_{stages} = \frac{log\left(\frac{N_p}{1-N_p}\frac{1-N_0}{N_0}\right)}{\log(a)} \ ,$$

Where $N_p$is the product molar enrichment and $N_0$is the initial molar enrichment.

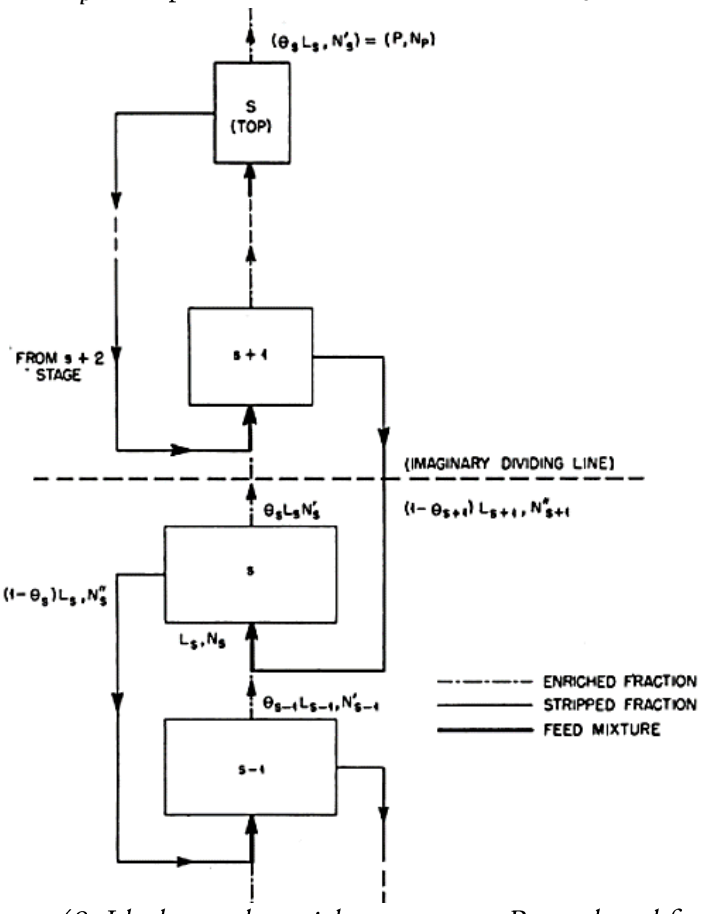

Figure 48. Ideal cascade enrichment stages. Reproduced from [107].

The total flow in this ideal cascade, in mol/s, is given by [107]:

$$\sum_{s=0}^{S} L_s = \frac{a+1}{a-1} P \left[\frac{(2N_p-1)\ln\left(\frac{N_p}{(1-N_p)P_0}\right)}{\ln(a)} + \frac{a-(a+1)N_0}{a-1} \frac{N_p-N_0}{N_0(1-N_0)} \right] \quad (5)$$

Where P is the product (enriched ^{79}Kr) flow and P_0 is the initial flow rate into the enrichment system. By calculating the total flow in the system based on the product flow requirement and enrichment requirements, this allows us to estimate the total mass of the DC discharge capillary elements, M_{enrich}, based on the individual elements size:

$$M_{enrich} = \frac{RT\tau_{stage}}{PV} m_e \sum_{s=0}^{S} L_s \ ,$$

Where R is the ideal gas constant, T is the gas temperature, τ_{stage} is the time required for the isotope concentrate on to reach equilibrium, $m_e$is the mass of an individual element. One challenge with this design is that the enrichment of the Krypton coming into the enrichment system, N_0, changes during the breeding of ^{79}Kr, following:

$$N_0 = \frac{^{79}Kr}{^{79}Kr + ^{78}Kr}.$$

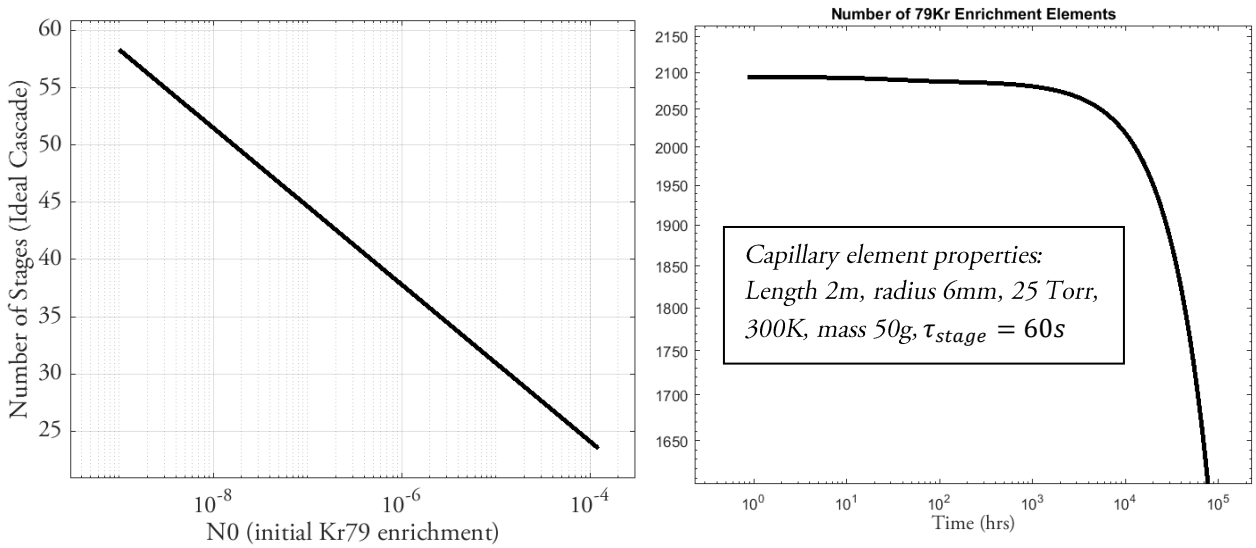

Figure 49. On the left, number of stages in ideal cascade enrichment system vs ^{79}Kr feed enrichment N_0, based on output flow rate, P, required to generate enriched ^{79}Kr in less than the radioisotope half-life. On the right, the number of elements required vs mission time.

The total flow from equation 5 above is somewhat independent of N_0 for low enrichment ($N_0 \ll 1$). However, the number of stages required in an ideal cascade varies with N_0, such that number of stages required during the breeding stage, when N_0 will increase in the range $10^{-9} < N_0 < 10^{-4}$.

It's clear from Fig. 49 that the enrichment process during the early stages of ^{79}Kr breeding will not follow the ideal cascade dynamics, since the physical number of elements cannot change, this may lead to inefficiencies of the enrichment cascade and an increase in the breeding period. In addition, the number of elements is necessarily high due to the low enrichment and flow requirements due to finite ^{79}Kr lifetime. In the example in Fig. 49 above, the mass of the elements is approximately 100kg, which does not include the required cathode/anode structures, gas handling, and power supplies. If we assume a similar current density in the DC discharge capillaries to reference [104}, then the total power required for this enrichment system is ~25kW.

Mills Separation Method

Mills suggested the use of ^{79}Kr as a positron beam source in the early 1990's [36]. Later, Mills also devised a means to enrich the ^{79}Kr in order to increase the intensity and brightness of cold positron sources [35]. This method takes advantage of differing sublimation rates between ^{78}Kr and ^{79}Kr.

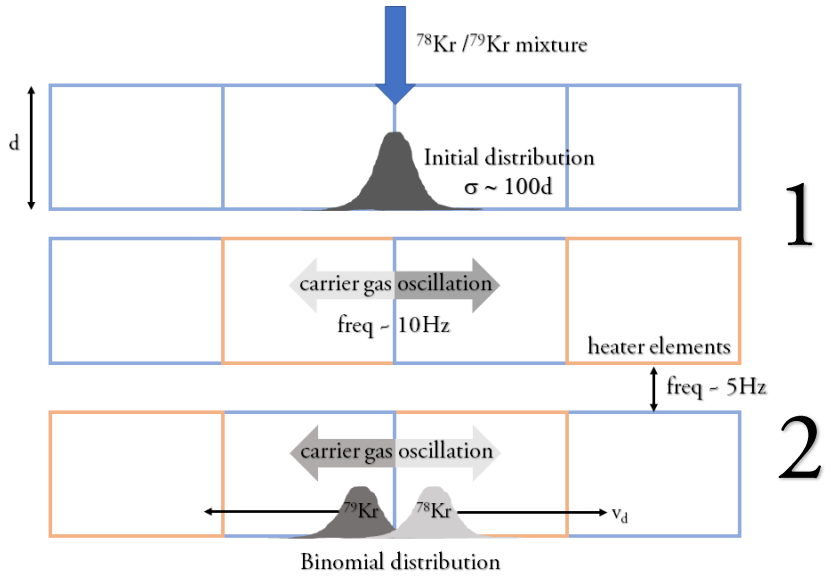

Figure 50. Overview of Mills Separation Method.

In this concept, the ^{78}Kr/^{79}Kr mixture is fed into the center of a long cylinder with diameter d, with large number of heater elements. In part 1, the heater elements are turned on such that a Gaussian distribution is formed with a frozen layer on the walls of the cylinder with a standard deviation of 100σ. In part 2, a carrier gas (e.g. D_2, He) is oscillated at frequency, f ~ 10Hz, while the heater

elements are switched at frequency $f/2$. The heater power is adjusted such that half the frozen Krypton is evaporated from the cylinder wall surfaces in a time $\frac{1}{2f}$. The Krypton isotopes will then spread along the cylinder in a binomial distribution process, with the centroid moving at velocity:

$$v_d = \left[\sqrt{\frac{79}{78}} - 1\right] fd \approx {fd}/{157}\,.$$

In this case the enrichment or the product concentration depends only on the initial molecular abundance ratio, $R_0^{78} = \frac{N_0^{78}}{N_0^{78}-1}$, and the number of cycles, n:

$$N_p \approx \frac{1}{1+R_0\left[1+erf\left(\frac{n}{2.2E4}\right)\right]}.$$

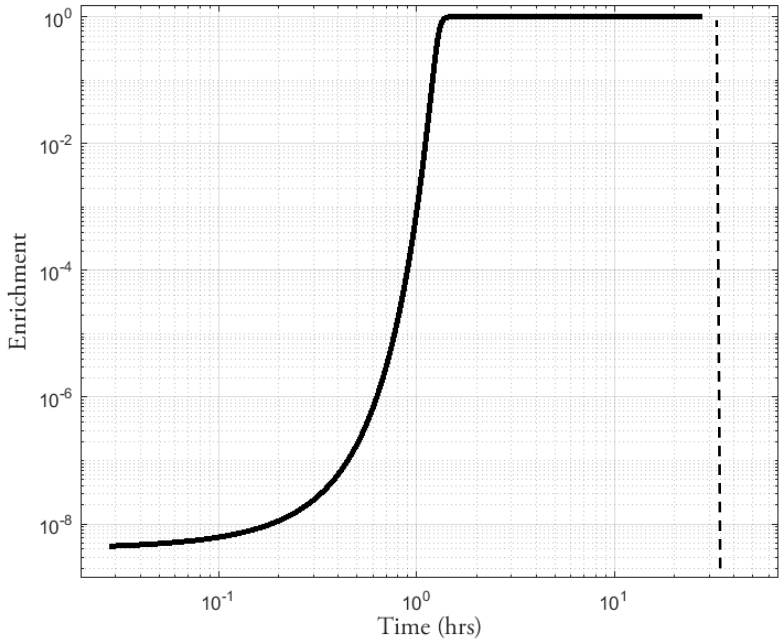

Figure 51. Molar fraction of product, N_p, in Mills Separation scheme vs time. The dashed line indicates the half-life of the product isotope, ^{79}Kr.

From Fig. 51 above, we see that a Mills Separation system offers extremely high separation factors in a single stage, negating the need for a cascade type enrichment scheme. To estimate the mass and power requirements, we start with a reasonable estimate of the cylinder diameter of d=5mm, based on the requirement to place heating elements at intervals of the cylinder diameter. Using the sublimation curve of Krypton [114] we can estimate the layer thickness δ_L, such that half of Krypton is evaporated in a time $\frac{1}{2f}$:

$$\delta_L = \frac{P_{vap} dM_u}{\pi R T \rho_s}.$$

For an average temperature of 80K and a vapor pressure of 3E4 Pa, this gives a required Kr layer thickness of 3um. Each section of the separation cylinder contains approximately 1mg of Kr. Estimating the total length of the separation cylinder is approximately 500d or 2.5m, consistent with the length scale of the positron beam optics, making the total mass of Kr in the single separation cylinder 500mg. Using a similar mass scaling to the DC discharge elements, we estimate the mass of each 2.5m long separation cylinder with 5mm diameter at 1kg, including added mass due to heating elements. To reach the reach the peak demand for enriched ^{79}Kr, this would require 10 individual separation cylinders, totaling 10kg.

We expect the power demand from the Mills Separation scheme, P_m, to be dominated by the ~5,000 individual heater elements driving the evaporation of frozen Krypton from interior walls of the separation cylinders. An estimate of this power is based on the molar enthalpy of sublimation ΔH_{sub}=10.7kJ/mol,

$$P_m = \Delta H_{sub} \left(\frac{\pi P d^3}{RT} \right) f N_e.$$

Based on estimates for number of separation cylinders and heater elements, this gives a power requirement of 4.3kW. Including mass and power budget for the carrier gas handling and cryogenic separation of Krypton and carrier gas we estimate total mass of the Mills separation system at 20kg and total power draw of 6kW.

Based on the mass and power requirements of the DC Discharge method versus the Mills separation method, the Mills method is the clear choice for spacecraft applications. However, this novel isotope separation method has not been tested and will require further development.

3.5 Reference Spacecraft Design

While the majority of work in Phase I focused on annihilation catalyzed fusion ignition, positron beam system, and ^{79}Kr breeding feasibility, some other key aspects of an RPP-based spacecraft are considered here in order to decrease the uncertainty of the spacecraft SWAP. This will produce a more accurate mission analysis, although more detailed analysis of these subsystems will be part of future efforts.

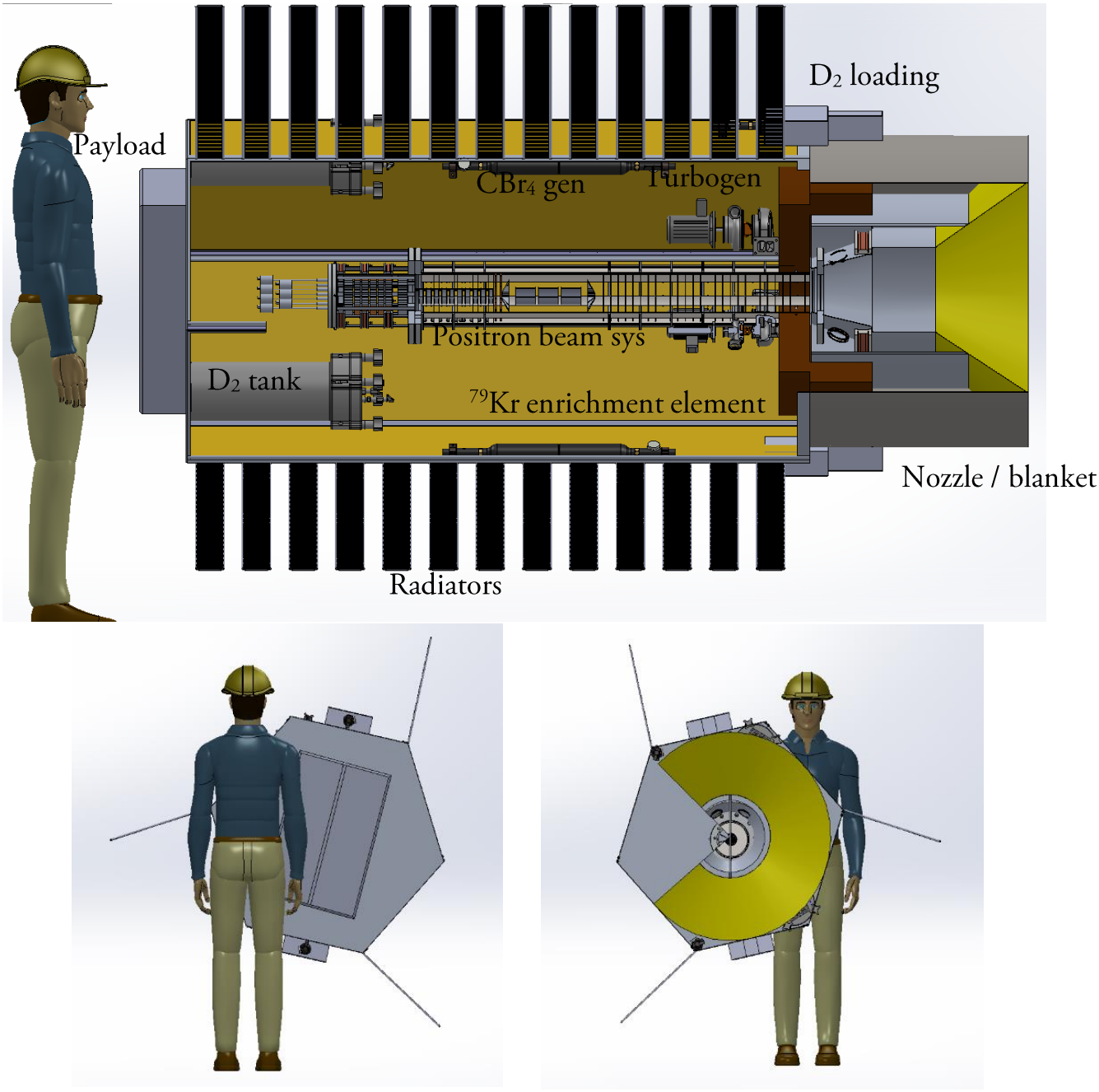

Figure 52. A cutaway model of RPP based spacecraft with deployed radiators, including most of the subsystems required for operation of the RPP engine.

3.5.1 Deuterium Fuel System

The Deuterium fuel will be stored in insulated tanks, as shown in Fig. 52 above, in liquid form at ~MPa pressure, at a temperature just above the triple point (~14K).

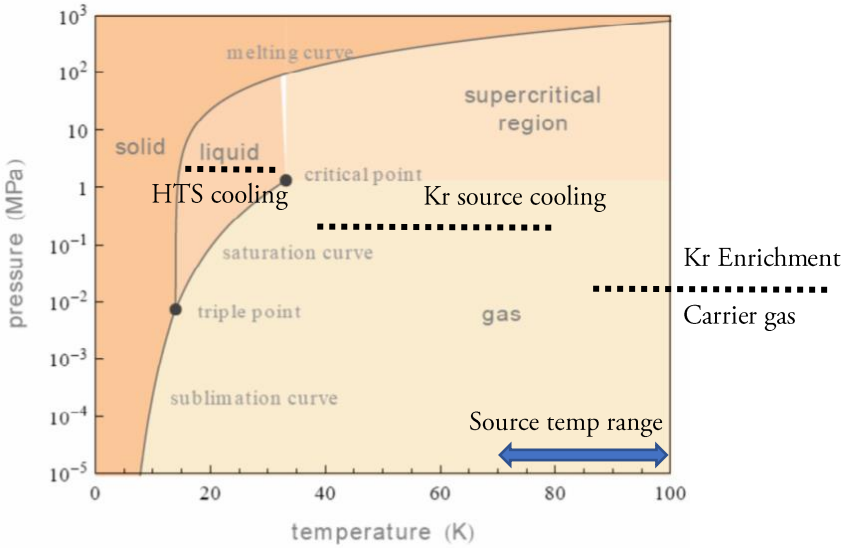

Figure 53. Phase diagram for Deuterium, reproduced from [108].

The cryogenic fluid will be used for active channel cooling of the source stage, augmenting the cryocoolers that maintain the frozen enriched ^{79}Kr layer at an appropriate temperature (see section 2.3). This process temperature ranges and pressures for magnet cooling, ^{79}Kr source cooling, and ^{79}Kr Enrichment stages are indicated by the dashed lines in Fig. 53 above.
Deuterium fuel will be transported to one of two substrate loading chambers, as shown in Fig. 54. Here the Deuterium will pass through a catalyst structure, where dense clusters are formed, and deposited onto a moving tape substrate. This arrangement is similar to laser ablation tape propulsion system, shown in Fig. 54 (left).

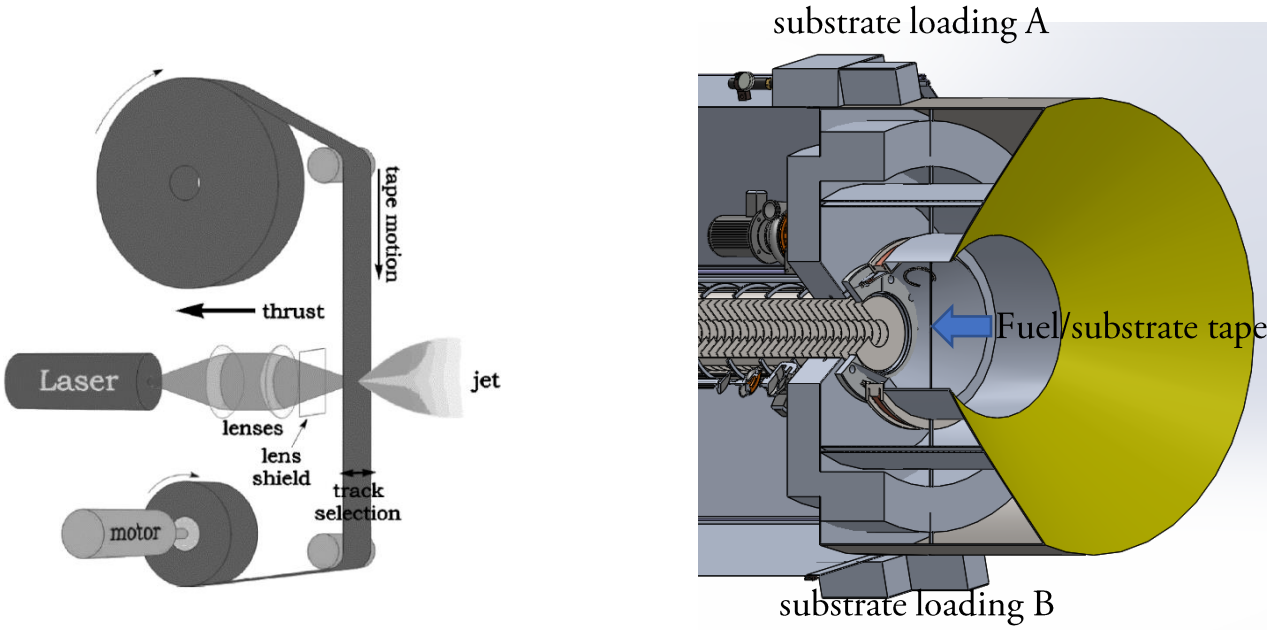

Figure 54. On the left, a laser tape propulsion system diagram, reproduced from [110] On the right, a cutaway view of the RPP nozzle, showing the two Deuterium substrate loading systems on two sides of the nozzle, with the fuel substrate tape traveling between the two.

The key difference between the laser ablation tape propulsion system and the RPP system is that fuel must be loaded onto the tape through a catalyst feed in a closed cycle, whereas the tape itself is the fuel in the laser ablation concept. The Deuterium loading will be done in closed chambers so that Deuterium gas that is not deposited on substrate surface can be recycled through the catalyst several times. This system would look similar to existing 'drop' sources [128], where D_2 gas flows through a Potassium doped iron-oxide plug several cm above a metallic substrate, with the addition of a feed and store mechanism for the substrate tape. Fig. 55 below shows existing static Deuterium cluster deposition chambers, used for laser spectroscopy of dense clusters on substrate surfaces.

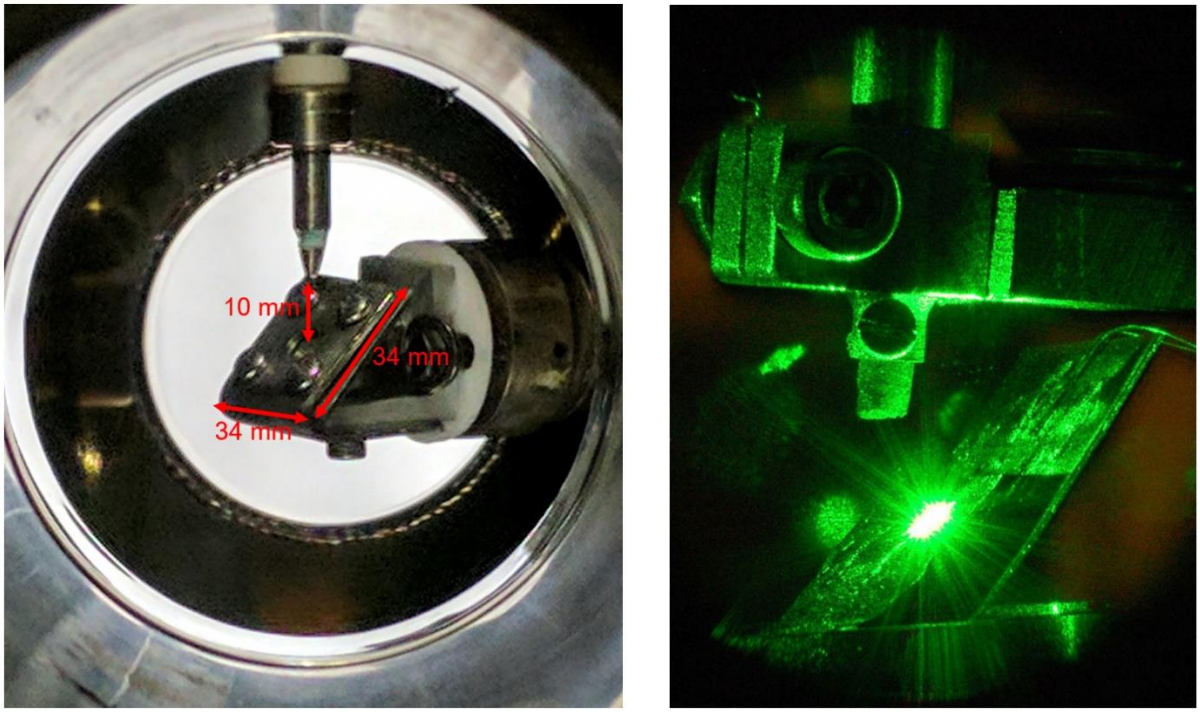

Figure 55. Loading dense Deuterium clusters onto metallic surfaces. On the left, the Positron Dynamics Deuterium loading setup (Appendix A), on the right, work from Holmlid et al [26].

The Deuterium handling system that we have described is a complex and interconnected system. The D_2 not only acts as the spacecraft fuel, but it also is an important cryogenic working fluid for several other subsystems – magnet cooling, source cooling, and carrier gas for isotope enrichment. This will necessarily complicate the D_2 handling requirements. However, by using liquid and gas-phase D_2 for multiple operations, the total number of cryogenic storage and handling systems is reduced, lowering total spacecraft dry mass and increasing mission performance.

The achievable D density on the fuel substrate is uncertain. Recent thermal desorption measurements indicate presence of ultra-dense clusters localized to lattice defects [65-68] with densities up to 10^{35} m^{-3}. Laser Time-of-Flight (TOF) spectroscopy measurements also support the existence of dense Deuterium clusters ([25-28], Appendix B). In addition, SQUID measurements that show these clusters exhibit properties of a type II superconductor [24], although the underlying mechanisms are not well understood. Theoretical work also suggested that Deuterium clusters in metal lattice vacancies may form Bose-Einstein-Condensates due to the extremely high local pressures [69]. As such, the local density and quantum state are likely to play a role in the annihilation momentum transfer probability, and fusion ignition properties (see section 3.2). For the Phase I RPP performance estimate, we assumed a target density of 10^{30} m^{-3}, which is higher than normal solid hydrogen fuels,

yet well below the ultra-dense regime($>10^{35}m^{-3}$) discussed above. Further experimentation and analysis of these dense Deuterium states will be the focus of future work.

3.5.2 Blanket Design

The initial Kr blanket design called for a single high-pressure gas section surrounding the DD fusion target, capturing neutrons and producing ^{79}Kr. While this design is the simplest, it requires significant structural strength at high pressure and temperature, leading to a design that may be too massive. We explored an alternative design with a hot gaseous section close to the DD fusion target, surrounded by multi-layered insulation, surrounded further by a medium pressure liquid Kr section.

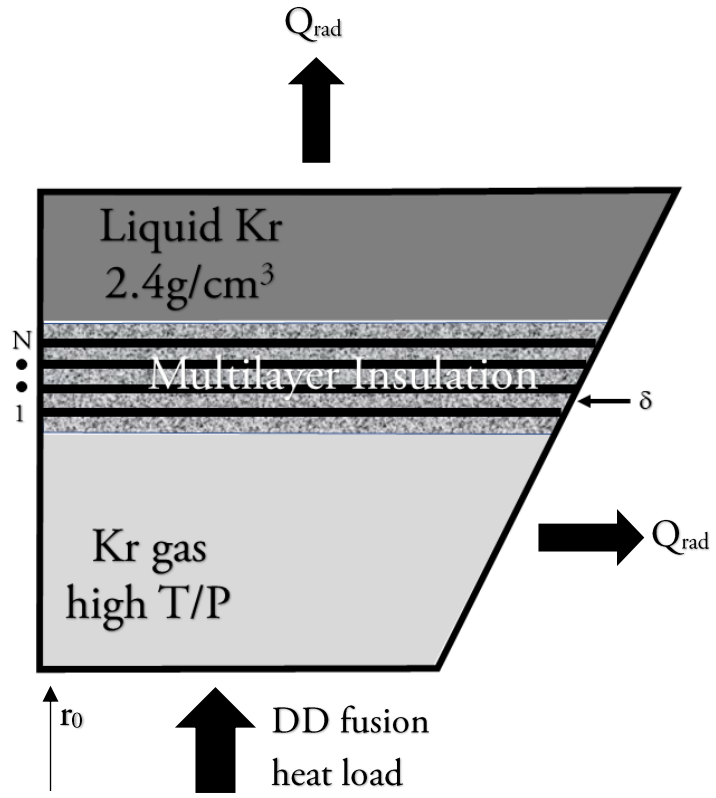

Figure 56. Second iteration of Kr blanket design, with hot gas section and liquid section.

This blanket design allows us to reduce the overall volume of the structure, due to the higher density phase of Kr. The solid angle to neutrons emitted from the D fusion target remains the same, as does the number density and path length product. From this, we can estimate that the neutron capture probability will remain the same, although investigation of the layered structure effect on neutron propagation will be studied in the future. In fact, if proper insulation material is chosen, the insulation layers may increase the neutron capture probability by shifting (or moderating) the neutron energy

spectrum to slightly lower energies where the $^{78}Kr(n,\gamma)^{79}Kr$ cross section is higher (see Fig. 12 in Sect 2.3).

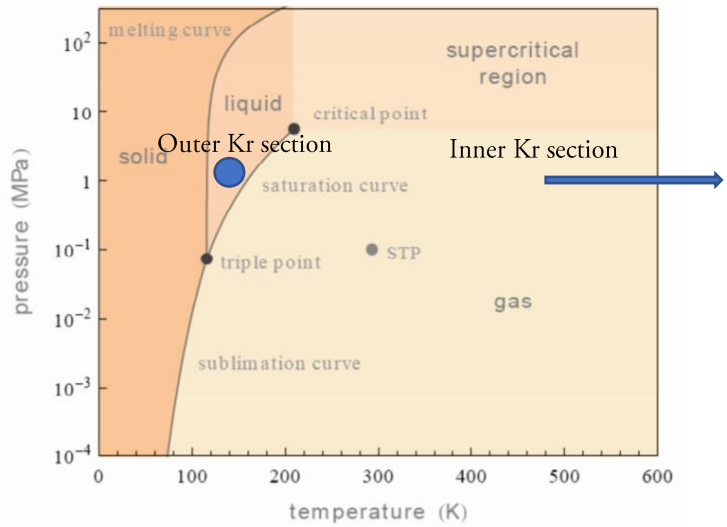

Figure 57. Phase Diagram for Krypton. Reproduced from [108]

The primary concern with this design is the thermal load and maintaining the temperature and pressure of the liquid Kr section due to the simple geometry and symmetry of the system, we can analyze the thermal characteristics of the design by approximating the structure as a concentric array of cylinders, such that passive thermal shielding is implemented using multilayer insulation (MLI). The MLI uses an array of reflective thin films (e.g. polished Aluminum) separated by insulating interlayers (e.g. Aerogel, Vacuum). The reflective layers reduce radiative heat transfer while the insulating and/or vacuum layers reduce conductive heat transfer. The heat load to the outer surface (which radiates to ~4K thermal well) in such a system with N concentric MLI structures is given by [115]:

$$q = \frac{\sigma A_N (T_0^4 - T_0^4)}{\left(1+N\frac{\delta}{r_0}\right)+\frac{1-\varepsilon}{\varepsilon}+\left(\left(\frac{1-\varepsilon}{\varepsilon}+\frac{1}{2}\right)\sum_{i=1}^{N-1}\frac{2\left(1+N\frac{\delta}{r_0}\right)}{1+i\frac{\delta}{r_0}}\right)}.$$

This allows us to estimate the heat load to the outer LKr layer as a function of the number of MLI layers based on the core geometry and Kr gas temperature (See Fig. 58).

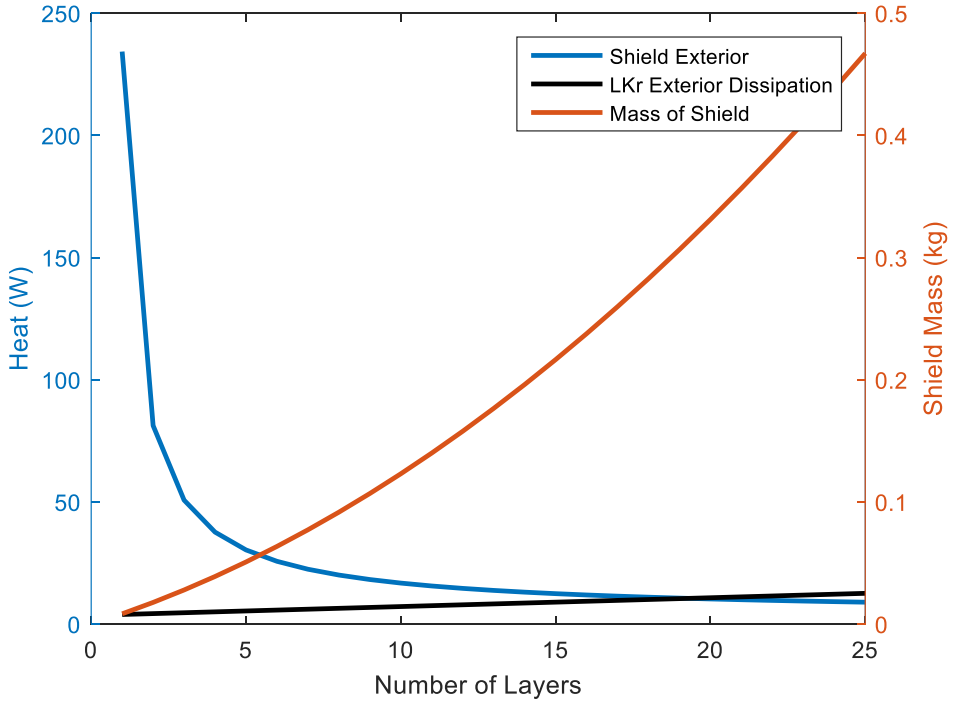

Figure 58: Estimate of the radiated power to the LKr tank at 150K for an r_0 plus interior tank of 10 cm thickness at 1000K, an upper estimate to core blanket temperature. Heat shield material is 25 um Al foil with 1 cm spacing (concentric cylinders). Layers are separated by aerogel. The length of the assembly is 20 cm (See Fig. 56).

The interior radius of the tank is 10 cm as discussed in the following section. Fig. 58 indicates that 20 layers balances the radiative heat load incident on the interior surface of the LKr tank and its exterior. The total tank dimensions are 40 cm in radius and 20 cm in length. Based on the volume and pressure these concentric tanks, a mass scaling using Ti-alloy tanks is input into the MATLAB system model.

3.5.3 Turbine Generator

In order to remove heat from the interior blanket section, a high pressure/high temperature gaseous Krypton section drives a high specific power (kW/kg) turbine generator. The electrical power generated from the turbine will power electrical heating elements on radiator structures described in Section 3.5.4.

This allows for radiator temperatures higher than krypton gas temperature, reducing the size and mass of the radiators. An overview of this system is shown in Fig. 59.

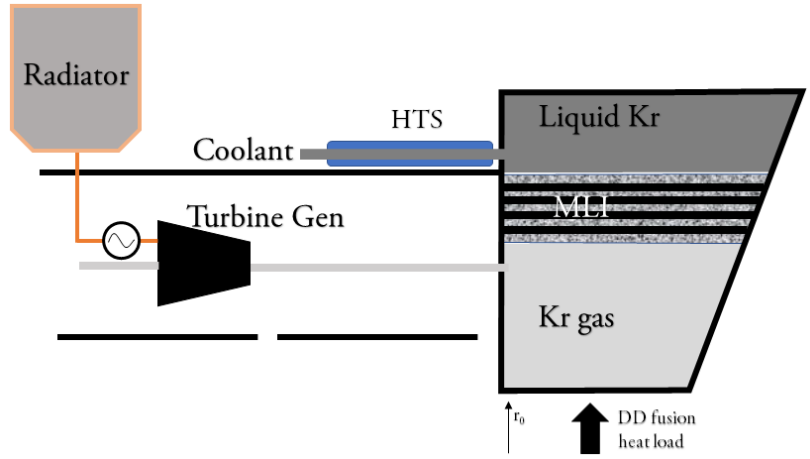

Figure 59. Overview of turbine generator system.

The heat load to the interior gas section of the blanket is primarily due to energetic charged particles and neutral particles impinging on interior nozzle structure. The heat flux depends on the magnetic structure, ignition characteristics, plasma expansion (see section 3.5.5) and blanket geometry. We can estimate the heat load to the interior nozzle wall, assuming a static magnetic field and the fusion reaction products follow single particle trajectories (no plasma effects).
In this case, we start with an isotropic distribution of fusion products with velocity v_e, which has a component perpendicular to the magnetic field, $v_\perp$, and parallel to the magnetic field, $v_\parallel$. The Larmor radius of the charged particles is,

$$r_g = \frac{mv_\perp}{qB}.$$

If we substitute specific impulse for velocity of the particles using $v_e = g_0 I_{sp}$, we can estimate the heat load to the interior blanket section, q_b, based on the fusion rate, f, average energy released per fusion event, Q_{DD},

$$q_b = \frac{fQ_{DD}}{2\pi}\left(\frac{\pi}{2} - \tan^{-1}\left[\frac{r_0 qB}{mg_0 I_{sp}}\right]\right).$$

From Fig. 60 below, we can see that the heat load to the blanket structure increases with specific impulse. At a magnetic field of 10T and 100mm nozzle diameter, the heat load fraction to the blanket wall is <6% of the fusion power at specific impulse below 10^6 seconds.

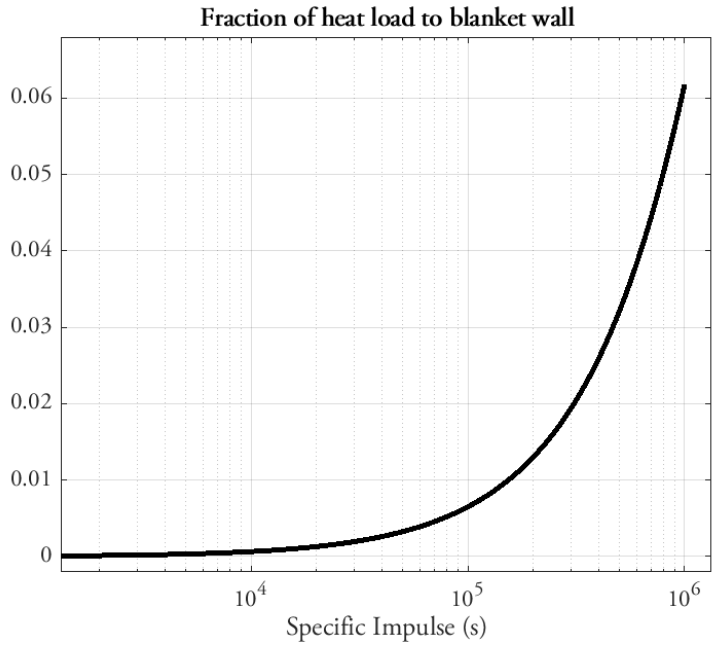

Figure 60. Fraction of heat load to interior blanket wall from microfusion vs specific impulse, based r_0=50mm and B=10T.

From energy balance in this system the heat load follows,

$$q_b - Q_{rad} - Q_{gen} = 0,$$

where Q_{rad} is the radiated heat and Q_{gen} is the heat removed by the generator. For a fixed geometry of the blanket core and assuming perfect emissive surfaces, we can estimate the load dissipation required of the turbine-generator and estimate the system mass to input into the MATLAB system model. Recent advances in oil-free, high-speed micro-turboalternators [116] have achieved high specific power through operating speeds up to 180,000 rpm and the use of compliant foil bearings, allowing for high operating temperatures. In addition, the alternator section is isolated from the turbine engine portion of the system to further decrease thermal load to the generator section. An example of such a turbine-generator is shown in Fig. 61.

We may estimate of the enthalpy available in the interior section of the Kr blanket that can be extracted by a tubrogenentor system using expected temperature and pressure of the Kr gas. We estimate that the inter blanket region will be at 1000 K and at a pressure of 10 Bar. Assuming a temperature difference of ~700 K, approximately 43kJ of energy is available. This estimate is based on the geometry of the blanket and an exhaust temperature of the turbine at 300 K. However, turbo-generators such as those shown in Fig. 62 have been designed to operated closer to 2 Bar. The current performance of a single turbo-generator at a specific power of 1.6kW/kg is able to move 80 g/s at high (180krpm) operating speed. To maintain thermal equilibrium of the inner blanket, approximately 100

g/s would be required to flow. Thus, it appears feasible to use multiple or parallel stages to extract heat from Kr gas which has been heated in the inner blanket.

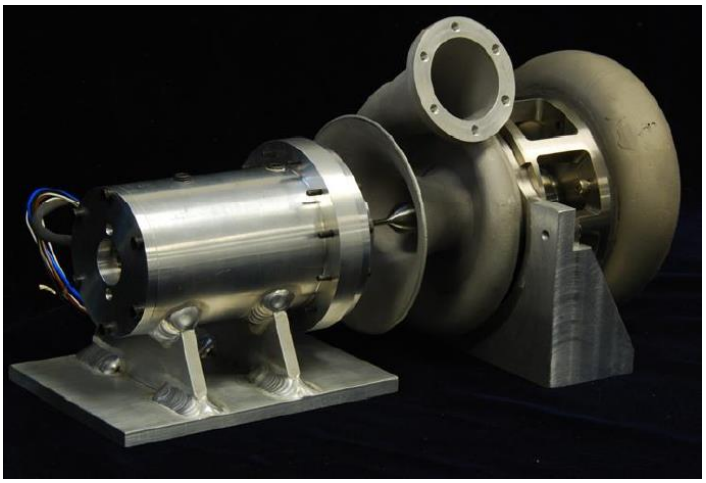

Figure 61. An assembled turbo-generator with specific power of 1.6kW/kg. Reproduced from [116]. This turbine was shown to operate up to 760 deg C.

3.5.4 Radiator

Because of the nature of the DD fusion reaction, the production of thrust from the reaction products is not 100% efficient. In fact, a large portion of kinetic energy from the fusion reactions will be deposited into the surrounding nozzle structure. This kinetic energy will turn into heat and will need to be dissipated for a steady state temperature to be reached.
Most fusion based propulsion systems require such large radiator structures that the radiator will dominate the overall spacecraft design. High emissivity coatings are common and nearly ideal such that any improvement in dissipating a heat load, q, will come by increasing the radiator temperature, since the area of the radiator, A_{rad}, follows:

$$A_{rad} = \frac{q}{\varepsilon \sigma T^4}.$$

Recent work using bare woven carbon fiber have demonstrated radiator areal densities of 2kg/m2 [117] at a radiator temperature of nearly 600 deg C. This is consistent with NASA technology roadmaps for radiator technology.

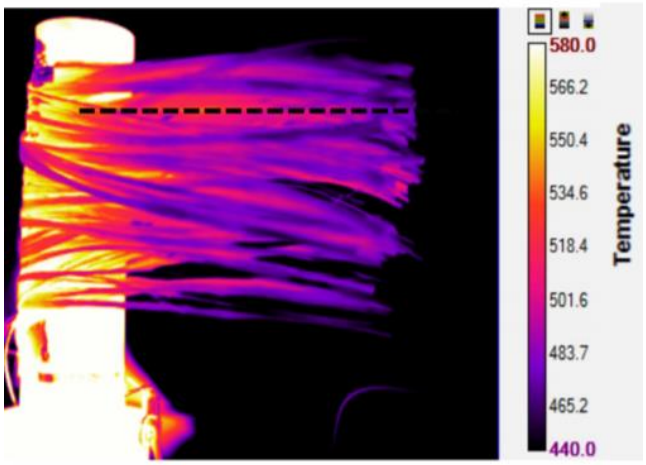

Figure 62. Woven carbon fiber at 580deg C, reproduced from [117].

The primary role of the radiators is to dissipate the thermal energy incident on the interior blanket structure, caused primarily by hot plasma and neutral particles impinging on the inner surface of the nozzle aperture. The exact amount of heat energy will depend on the plasma expansion properties and average fusion rate. Following the analysis from section 3.5.3, we expect a heat load in the range of 10 – 100kW. This energy will be transferred through radiative and conductive heat transfer to the Kr gas in the inner core region and electrical power will be generated from the Kr gas enthalpy (section 3.5.3). While some of this electrical power will run spacecraft subsystems (e.g. Kr enrichment, Avionics, etc.), most of this power will be directed to electrical heating elements in the radiators. This radiator system is composed of arrays of woven carbon fibers on a deployable structure, operating at approximately 600C (see Fig. 52).

3.5.5 Magnets

The initial design of the target, blanket, nozzle section included a resistive pulsed magnet, cooled with cryogenic Kr. The short pulse characteristics and low duty factor of the positron beam system was the driver for the pulsed magnet design. This type of magnet has been designed and operated successfully at 30T (see Fig. 63). Unfortunately, the positron beam pulse repetition rates at higher thrust levels approach 100kHz, which make the cooling requirements unreasonable. In addition, the pulsed resistive magnet design requires a massive capacitor bank that would further reduce propulsion system performance.

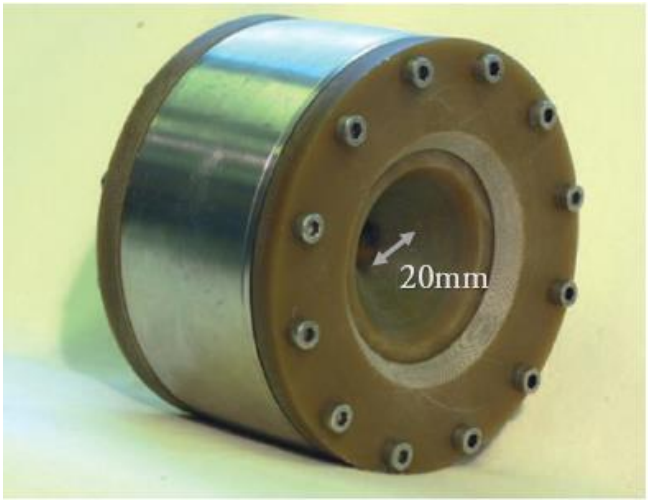

Figure 63. Resistive pulsed 30T magnet. The magnet was submerged in a liquid nitrogen bath and operated at 6 pulses per hour (.0016Hz). Reproduced from [118].

Initially, the RPP concept did not include a superconducting magnetic nozzle, due to concerns about magnet mass and cryogenic constraints of superconducting coils. However, the magnetic field requirements of the pulsed positron beam system (see section 3.3) in combination with recent advances in large-bore high temperature superconductor (HTS) have warranted further consideration. These magnets based on rare earth Barium-Copper-Oxide (ReBCO) elements which can operate as a superconductor up to 90K and are formed into extremely strong, flexible, and thin tapes, as shown in Fig. 64.

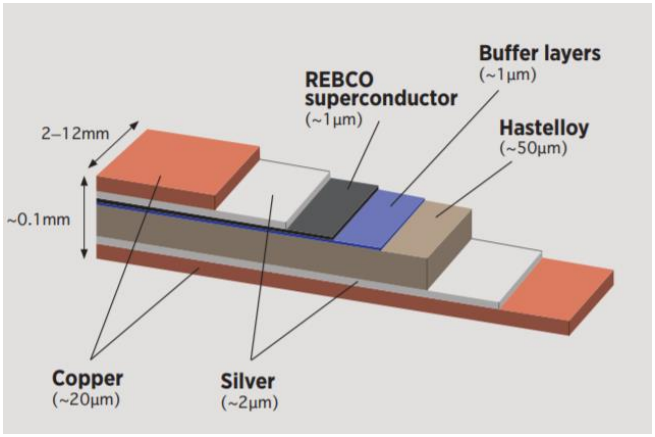

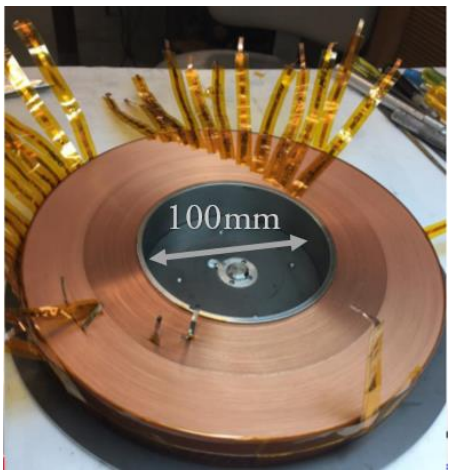

Figure 64. ReBCO high temperature superconductor, with operating field of 30T. On the right, a coil section from HTS large aperture coil being designed at Brookhaven National Lab, reproduced from [120].

These HTS materials are sought after in the production of compact fusion tokamak [129], since fusion power in these devices scale with B^4. For our purposes, the larger bore means that energetic fusion products are less likely to interact with the nozzle wall structure, increasing thrust while relaxing cooling requirements of the blanket structure.

Studies on the neutron damage in BCO type superconductors indicate that the HTS performance will not be significantly degraded over the lifetime of operation at large scale fusion reactor [64,64]. A sketch of how the HTS coils might be integrated into the existing blanket/nozzle design is show in Fig. 65.

The HTS ReBCO magnets will require MLI and LKr layer insulation from the hot section of the blanket. Active cooling will be required to maintain magnet temperature between 20-70K. The critical field lowers significantly towards the high end of this temperature range, while the cooling power capability increases at the higher temperatures. A full analysis and trade study of magnet operating temperature, cooling mechanisms, and mechanical properties will be the subject of future work.

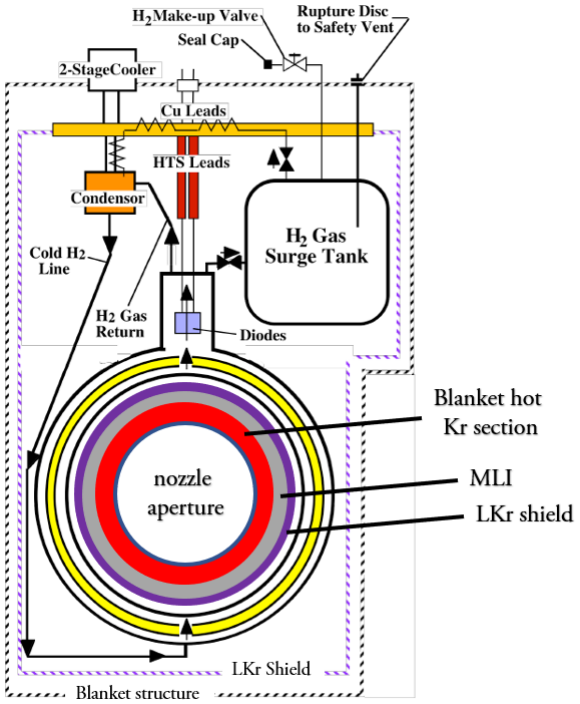

Figure 65. Overview of magnet (yellow) cooling system, adapted from [121]

For the RPP concept we provide a rough estimate of magnet properties that are derived from an example ReBCO magnet [120] with bore size comparable to the RPP positron beam system and Kr blanket inner diameter. Direct conduction cooling using a pulse tube Stirling or two-stage GM type cryocooler for such a large magnet is infeasible. Therefore, a liquid cryogen loop is a more likely solution to maintain the magnet operating temperature. Traditionally, Helium cryocoolers are used to cool down and maintain low temperatures required by superconducting materials at temperatures <10K, typically between the He triple point temperature (2K) and critical temperature (5K). With the advent of different HTS materials, operating temperatures in the range of 10-70K are possible, allowing for working fluids with higher triple point and critical temperatures.
As such, we envision that cooling for the HTS magnet may be provided by thermal siphon cooling loop system utilizing the spacecraft fuel (D_2) as the working fluid, with a triple point and critical temperature of 14K and 32K [122]. In fact, a

Hydrogen-based cooling arrangement has been studied previously [123] (see Fig. 65). Such a cooling system would also benefit the overall RPP system performance by supplying a common D_2 compressor infrastructure, as the operating frequency of the Stirling type cryocooler (50-100Hz) is in the same range as the operating frequency of the Mills method isotope separation method (see Section 3.4.3). Thus, the D_2 gas could be used in both the HTS Stirling cryocooler and the ^{79}Kr enrichment process, eliminating the need for a separate carrier gas compressor and associated gas handling system.

3.5.6 Thrust and Delta-V

The dynamics of the expanding fusion plasma into the surrounding magnetic structure is a complicated problem involving the interaction of an expanding dense plasma with magnetic structures (see Fig. 66). A detailed analysis and simulation of the physics of the magnetic nozzle is not within the scope of this work. However, the significant previous work in this area has led to thrust efficiency estimates for magnetic nozzles of approximately 60% [86, 124-126].

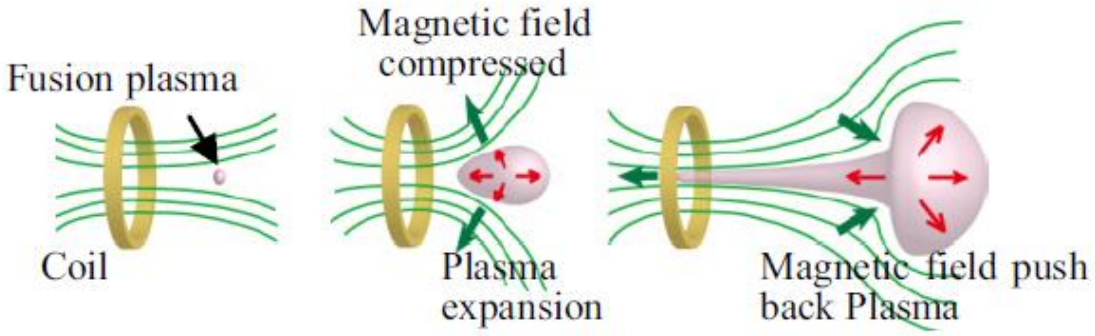

Figure 66. Overview of target expansion in magnetic field following fusion burn. Reproduced from [86].

The thrust efficiency is defined as the ratio of total parallel momentum to total initial momentum:

$$\eta_e = \frac{\sum m_e v_{\parallel}}{\sum (mv)_{DD}}.$$

This equation gives us a means to relate initial fusion product momentum, $(mv)_{DD}$, to momentum of exhaust particles producing thrust, $\sum mv_{\parallel}$. From this, we can estimate propulsion system thrust without an exact solution to the plasma dynamics of the microfusion burn and plasma expansion.

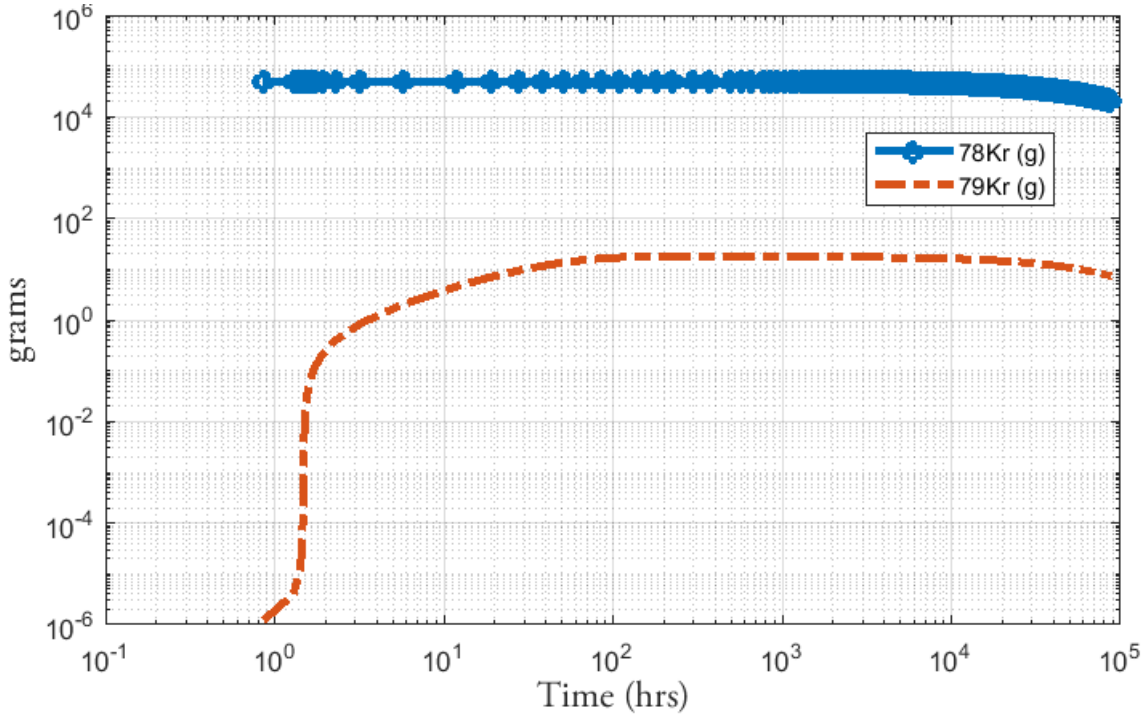

Figure 67. Amount of ^{78}Kr and ^{79}Kr versus time from MATLAB RPP model.

Using the breeding model from section 3.4.2 and subsystem properties from sections 3.1-3.5, an RPP system performance model was generated in MATLAB. The model inputs and characteristics are included in Table 2 below. From Fig. 67, we see that the initial breeding period lasts less than a week, increasing the amount of ^{79}Kr from 1ug to more than 10g and thrust from Nano-N's to 200mN. This also means that the RPP system can be turned off for days at a time, without losing the ability to restart the engine.

Table 2. MATLAB RPP model inputs and thrust characteristics

ITEM	VALUE	NOTES
Positrons/pulse	1.96E11	Section 3.2
R (annihilation momentum transfer probability)	0.1	Morioka, Appendix B
^{79}Kr Source Area	200 cm2	8cm radius source
Positron pulse temporal FWHM	400 ps	SIMION + heritage
Positron beam width FWHM at target	50um	SIMION + heritage
Positron pulse repetition rate	.006Hz – 80kHz	
Moderator Efficiency	0.4	See Appendix C
Fuel (D) density	1E30 m^{-3}	See Section 3.5.1
Ignition burn depth	250nm	

Burn fraction	10%	0-D simulations
Specific Impulse	3E5 secs	
Initial ^{79}Kr	1ug	
Maximum ^{79}Kr	14g	
^{79}Kr enrichment	0.99	Mills method
Accumulator lifetime	100sec	Previous work
Thrust efficiency	0.65	
Thrust	10nN-0.2N	
Maximum engine power	2.1MW	
Delta-V capability	60km/s	

This model assumed a total initial Kr mass of 52kg, including 1ug of ^{79}Kr. Engine throttling is accomplished by controlling the repetition rate of the pulsed positron beam, with the maximum repetition rate constrained by the ^{79}Kr source intensity and positron beam characteristics.
The work described in prior sections was used to determine refined estimates of the spacecraft mass properties and the performance attainable by the RPP system in the mission application to retrieve the asteroid and bring it to Earth's orbit. The key elements, derived masses, and the basis of the underlying assumptions are briefly described below.

Table 3. Mass properties of an RPP based ARM concept spacecraft

System Element	Dry Mass Outbound (kg)	Assumption
Radiator	5	2 kg/m2, 800K, e=1, 2.5m2
Krypton	52	Breeding analysis, neutron cap
Positron beam	100	0.1 T coils, from CAD model
HTS Magnet	164	CAD model
Payload	25	Asteroid manipulation hardware
Turbogen (power)	26	1.6 kW/kg
Structure	75	Interplanetary allocation as a percentage of dry mass [127]
Kr blanket structure	15	.03bar m^3/kg Ti alloys tank
Isotope separation	26	Based on Mills method (including carrier gas sys)
Attitude Control System	13	Interplanetary allocation as a percentage of dry mass [127]
Communications	22	Interplanetary allocation as a percentage of dry mass [127]

Command & Data Handling	13	Interplanetary allocation as a percentage of dry mass [127]
Harnessing	32	Interplanetary allocation as a percentage of dry mass [127]
Deuterium System	34	Including 15kg D_2 fuel
CBr4 Generator	10	<500mg/hr production
Misc. Positron beam support hardware/electronics	40	
Shielding	10	ExB or physical shutter between source and target
TOTAL	662	

3.6 Mission Analysis - Asteroid Redirect

Low-thrust trajectory calculations (using GMAT [135]) were performed to demonstrate the benefits of an RPP system in a potential mission application – an asteroid redirect mission to target 2009 BD.

Based on the performance analysis performed in previous sections, a constant specific impulse of 3E5 seconds and 200 mN constant thrust were assumed for initial trajectory calculations. Assessing the first-order feasibility of the derived dry mass performing a rendezvous with 2009 BD, we find that with a canonical impulsive two-burn transfer from LEO to the target, the 662kg delivered mass is well-enveloped by the capabilities of Falcon 9 and Atlas V class launchers for a wide range of prospective departure dates, with times-of-flight within a year possible. Thus, it is feasible that several launch opportunities will be available within the parameters of the spacecraft. The limiting factor in this case is performance to fly the asteroid back to the proximity of Earth.

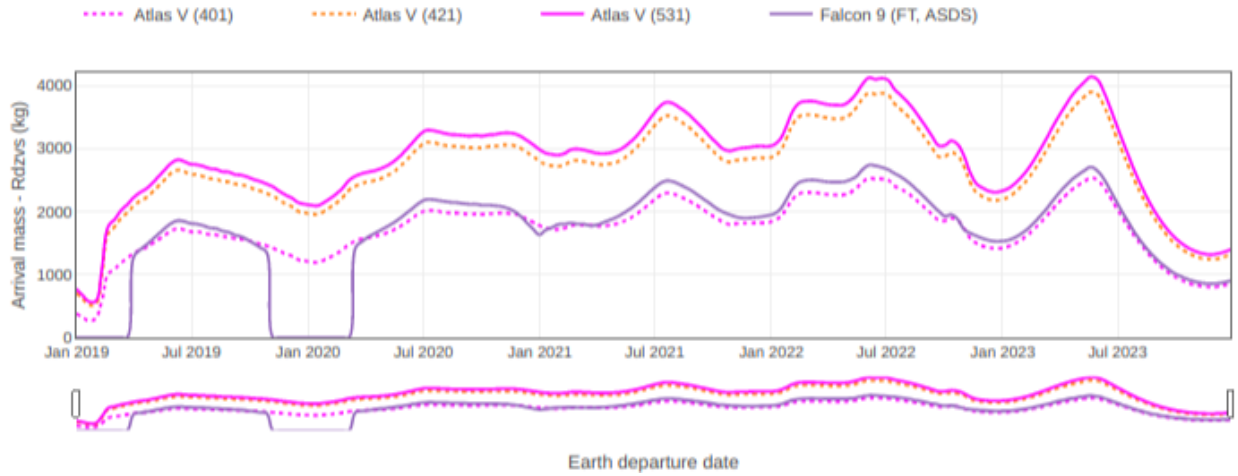

Figure 68. Rendezvous mass for two impulsive burn transfer to 2009 BD, per JPL Small Bodies Mission Design tool [131].

Ephemeris data for 2009 BD (NAIF 3444297) was obtained from the SPICE database [132]. The approach used to target the destination is B-Plane targeting. The B-Plane is a planar coordinate system associated with the target (in this case, the asteroid for the outbound journey and Earth-Moon system for the return) which is perpendicular to the incoming asymptote of the approach hyperbola. Preliminary trajectory calculations were performed to arrive at the asteroid destination, to within a 100 km approach for the initial estimates. Burn duration and thruster duty cycle were the variable parameters in the optimization. Propagators were set up to propagate the trajectory in the near Earth, deep space, and near asteroid phases of the mission.

The time of flight to 2009 BD was found to be approximately 1.4 years for the arbitrarily assumed epoch, starting in at Low Earth Orbit and proceeding to the asteroid. Further studies will evaluate specific launch windows and further optimize the transfer times, but the initial trajectory analysis shows that the performance derived can accomplish the mission in a reasonable duration.

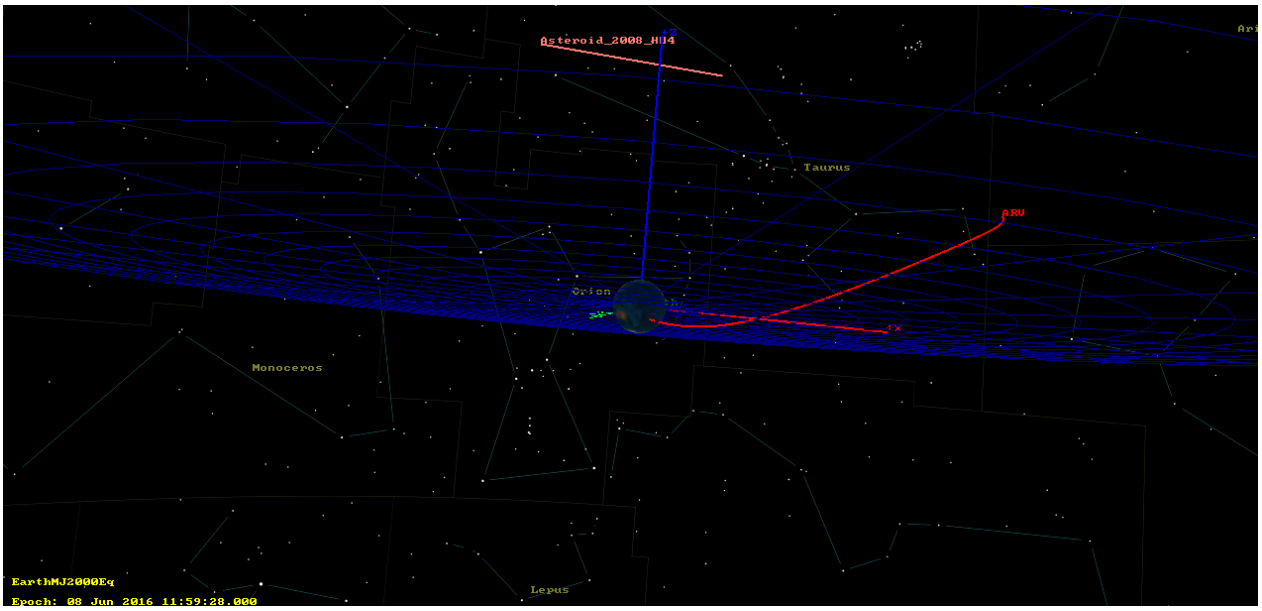

Figure 69. Earth departure visualization of trajectory to target asteroid 2009 BD.

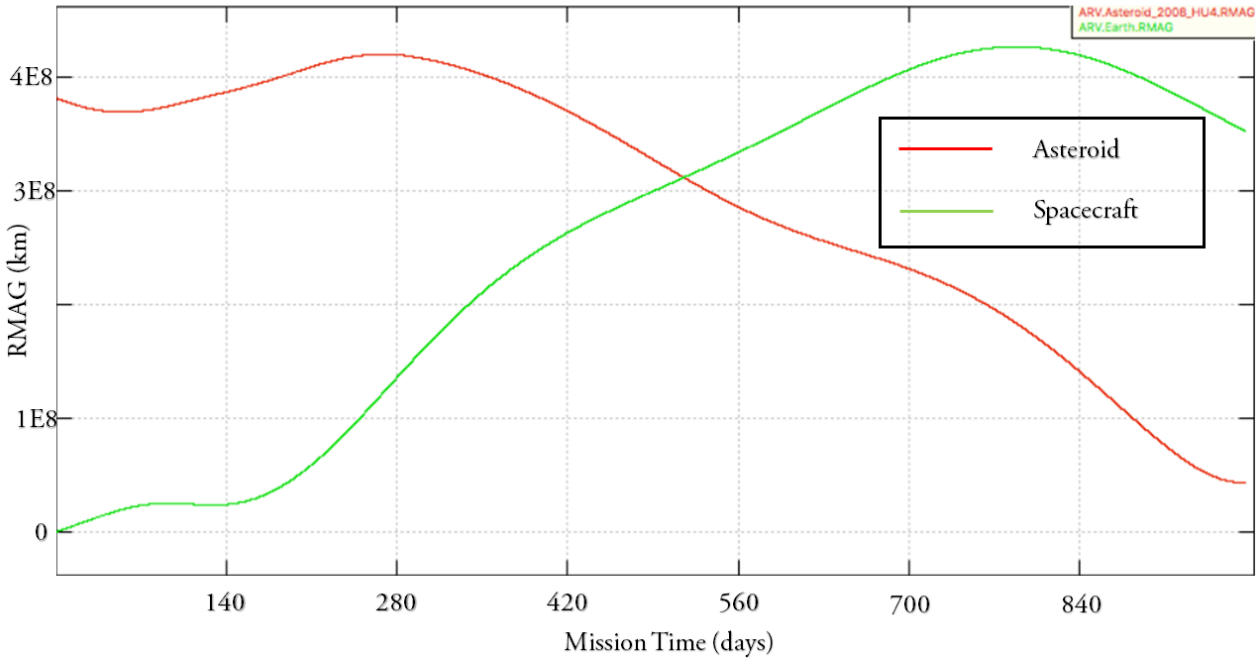

Figure 70. The radial magnitude (RMAG) position of 2009 BD and the RPP spacecraft in km in Earth MJ200 Eq coordinate frame.

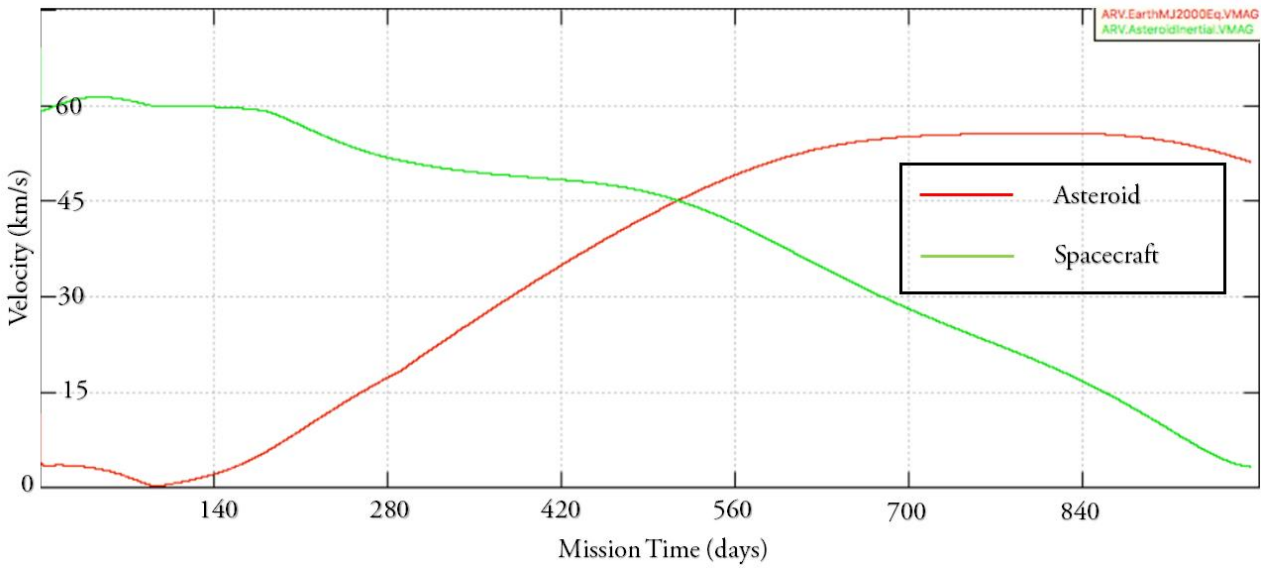

Figure 71. Velocities of 2009 BD and the RPP spacecraft in km/s in Earth MJ200 Eq coordinate frame.

Figures 70 and 71 show the outbound leg of the RPP spacecraft to the intercept point where the velocities and positions of the two bodies are equivalent at approximately 500 days.

The 2009 BD mass of 100 metric ton (1E5 kg) was assumed for the return leg. A delta-V of ~200 m/s, required to divert the asteroid to a trajectory inbound to Earth, can be achieved with an approximately

12-year transit time assuming 0.5 AU distance and ignoring the effects of gravity for deep space. This calculation suggests that the RPP as described in this report is capable of closing the mission profile.

The return trajectory was evaluated for both SEP and RPP for an arbitrary return date. Similar in principle to the outbound trajectory, the inbound to Earth trajectory was evaluated targeting the B-Plane of the Earth, stopping the burn at periapsis, and iterating on the burn duration and thrust vector. A target within 5 million km of Earth was chosen; further trajectory work will include bringing the asteroid to a Lagrange point or in orbit around the Earth or Moon. Some sensitivity analysis to the assumed coasting phase duration at the beginning of the return suggests room for further optimization.

Using the same performance parameters as the outbound journey for RPP, the return journey is achieved in 9.3 years burning 17.6 kg of propellant. Orbit insertion was not evaluated for this comparative evaluation.

Prior work performed as NASA's Asteroid Retrieval Mission study employed the use of SEP with an assumed Isp of 3000 s and thrust of 1N [132]. These studies predict mission duration on the order of 10 years. The performance parameters above were used to evaluate the duration in GMAT for an SEP system and the mission was found to be accomplished in 9.4 years burning 8,807 kg of propellant, which is in the realm of previous predictions given that significant effort was not applied to find the optimal solution for this comparative assessment.

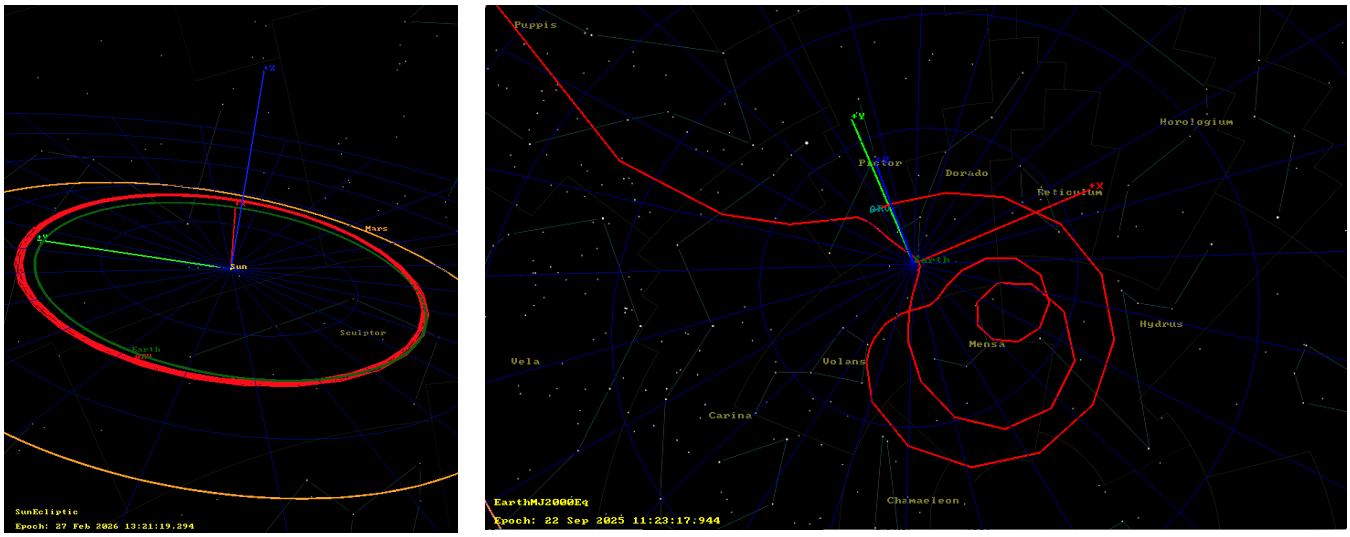

Figure 72. Radioisotope Positron Propulsion asteroid retrieval trajectory, from initial coast phase (left) to Earth proximity (right).

In conclusion, initial feasibility of performance capability has been determined using the mass properties and performance from the RPP study and further refinement and optimization of trajectory parameters, launch windows for an asteroid retrieval mission can be performed in roughly the same amount of time as the SEP mission. The RPP system offers a reduction in launch mass by a factor of 20. Such reduction in launch mass would mean that a much smaller/cheaper launcher could be used. Alternatively, a single large launcher (e.g. Falcon Heavy) might deploy several ARM spacecrafts.
The majority of Phase I work focused on minimizing launch mass, rather than maximizing Thrust. While lowering launch mass is important for cost considerations, ARM mission duration is more dependent on Thrust. Thus, it is likely that an array or scaled version of RPP concept could perform an ARM-type mission at a reduced mission duration. Reduced launch mass and mission duration are performance advantages would be attractive for the growing number of private companies interested in asteroid mining. For an asteroid redirect and capture mission, the ground-breaking nature of RPP concept is clear.

4. Next Steps, Challenges and Benefits

In this work plan we have addressed the most significant barriers to developing an RPP engine, however, several other challenges will need to be fully addressed: Remote source handling, Deuterium fuel storage and substrate loading, shielding, neutron damage and regulatory issues will need to be understood and mitigated. The high temperature and radiation environment presents a unique challenge for surrounding materials and electronics. Various fusion projects are addressing these issues and progress is being made, particularly in understanding of fusion facing materials and their damage characteristics inside fusion plasmas. A large effort over recent years has been made to develop high temperature, high-field, high-temperature superconducting (HTS) materials for magnetic fusion applications. HTS with high critical fields and current densities will offer reduced magnet mass and a decrease in heat load to the nozzle structure. We expect to leverage this technology to further increase the performance of the RPP based spacecraft.

We have identified several other benefits that could contribute, outside of propulsion technology, in a variety of fields: For example, the ^{79}Kr production and enrichment process could be used in terrestrial cold positron beam non-destructive diagnostic systems for investigating defects in semiconductors, photovoltaic materials, and thin-films (potential non-aerospace spinoffs).

The detailed study of ultra-dense Deuterium and fusion ignition characteristics will have significant benefits outside the aerospace field and in basic science research – this unique material could prove useful in advancing the terrestrial electrical power generation possibilities of ICF by reducing the amount of target pre-compression infrastructure and associated plasma physics challenges (plasma instabilities).

Utilizing hydrogen isotopes as engine fuel opens the possibility of In-situ resource utilization – refueling the spacecraft with hydrogen gathered from asteroids and other planetary bodies. A propulsion system like RPP is also advantageous when solar illumination is limited (e.g. shadowed, distant from sun).

The fuel cycle described could also provide abundant source of thermoelectric power to run avionics, communications, and sensors in a wide variety of aerospace applications.
High Isp and Thrust-to-Weight allows a spacecraft large velocity change (ΔV). Higher ΔV has a broad impact on all space-system architectures (e.g. earth/sun observing, LEO based services, planetary defense). For exploration purposes, very high ΔV (>1000km/s) capability produces large spacecraft velocities, reducing transit time for long distance missions both inside and outside of our solar system.

Next Steps:
Positron catalyzed fusion ignition in dense Deuterium targets is a key enabling technology #1. Phase I work showed that fusion ignition with positrons is feasible. Next, we will focus on work needed to demonstrate microfusion at a positron user-facility.

Deuterium fuel loading experiments
One of the largest uncertainties in the fusion ignition analysis is the number density of the Deuterium fuel. With several research groups reporting production of Deuterium densities ranging between 10^{24} and 10^{29} cm^{-3}[25-28,30,65-69], this parameter space is too large to make an informed design decision on target geometry beyond a simple planar model. Phase I ignition work showed improvement in ignition characteristics at higher Deuterium density. Therefore, production of Deuterium at a predictable and reproducible density and depth (location and distribution) is a key enabling technology #2. With the goal of producing dense Deuterium states on the surface of metallic substrates, we will use Temperature Programmed Desorption (TPD) measurements to determine loading fraction and temperature stability in addition to optical and scanning electron microscopy (SEM) to determine adsorption characteristics and damage of the metallic substrate due to the Deuterium loading.

Modeling targets and plasma expansion
Phase I included ignition analysis using Lawson criteria, 0-D energy balance simulation and preliminary 2-D PIC simulations including relevant physics (radiation, ionization, collisions). While the results of these simulations indicate fusion ignition is feasible, these simulations do not provide optimized target geometry or an estimate on thrust performance. In phase I, we considered planar target geometry for fusion ignition, more detailed simulations of the ignition process and plasma characteristics could point towards other higher gain geometries (e.g. Spherical, Conical).

These questions, along with determination of plasma expansion characteristics in magnetic nozzle (i.e. specific impulse) will be the focus of Phase II simulation work.

Ignition test-bed

In order to demonstrate key enabling technology #1 and advance the TRL of the propulsion concept, a demonstration of micro-fusion ignition is required. There are several positron beam facilities in the world, but few are capable of providing sufficient cold positron intensity ($>10^9$ s^{-1}) required to accumulate the required number of positrons in a single pulse to reach ignition. However, there are several planned improvements to these facilities coming in the next few years. The aim of Phase II work is to create a detailed design of a portable ignition testbed 'end-station' that can be taken to a beam-port at a positron user facility (e.g. NEPOMUC, NC State PULSTAR).

^{79}Kr enrichment and beam production

In the Phase II task, we will use a commercially available DD/DT neutron generator and a small amount of ^{78}Kr to generate a low-activity (<uCi) amount of ^{79}Kr. A liquid nitrogen bath will cool a cold-finger below the freezing point of Kr and a small amount of ^{79}Kr will be deposited on a cold-finger inside a vacuum chamber

After irradiation, the ^{78}Kr/^{79}Kr mixture is deposited onto a cold-finger surface in vacuum and cold positrons will be magnetically guided towards a Scintillation/PMT detector. The experiment can also be augmented with a cylindrical or mesh electrode used as a retarding potential analyzer to determine the energy distribution, parallel to the magnetic field, of the emitted positron beam, although the main purpose is to demonstrate production of a cold beam.

Mills Isotope Separation Testing

In the Phase I analysis, we determined that the Mills Method [35], using the difference in ^{78}Kr/^{79}Kr vapor pressure, was an efficient and lightweight means of ^{79}Kr enrichment, although it has yet to be demonstrated. Thus, a demonstration of the Mills method would satisfy key enabling technology #4. Rather than use expensive ^{78}Kr, the Mills method can be demonstrated with natural abundance Kr. Using a residual gas analyzer (RGA), we can measure the change in isotope distribution from natural abundance. In this system, a series of heating elements surround a long tube immersed in a LN2 bath. A commercially available He compressor provides the carrier gas in a controllable manner.

Spacecraft Reference Design

Phase II work will consider the entire spacecraft thermal state and the radiation environment and determine the effect to performance and ARM-type mission accomplishment.

The thermal analysis completed in the Phase I work focused on the Kr blanket, which surrounded the fusion volume to capture the largest solid angle of neutrons while allowing for extraction of the fusion products for thrust. In order to maximize the absorption of neutrons, a liquid layer was chosen, which requires a vessel at ~150 K. Thus, this tank would require thermal isolation from the fusion volume. It

was determined that an interior gas-phase vessel or tank at elevated temperature and pressure surround the fusion volume. While the Phase I work was able to show the feasibility of the nested tanks of gaseous Kr and liquid Kr in near thermal isolation, thermal analysis considering a typical trajectory in which the spacecraft would transit near radiating objects is a key next step. In addition, heat load from neutrals and neutrons to the ion optics and source moderator will be considered. An overall thermal model of the spacecraft subsystems, including the turbine-generator and radiator will be developed in Phase II work.

Radiation Damage

Radiation damage of components was not considered in the Phase I work. In Phase II, the radiation spectrum; neutrons, photons, neutrals, and charged particles, would be investigated to estimate the operation lifetime of critical components, in particular, those part of the Kr blanket and associated equipment. As the fuel cycle is only limited by the amount of ^{78}Kr, mission duration and/or performance may be increased should the radiation environment be found to be sufficiently benign. Thus, an analysis of the radiation damage of critical components is a key step in defining the maximum mission duration and ultimately performance.

Mission Application

The amount of mass which can be transported is the primary metric for any transportation technology. In principle, our fuel cycle enables continuous performance without the requirement of proximity to the sun. The reduced mass and increase performance of RPP over existing electric propulsion allows for multiple ARM type missions, but also the possibility of an extended prospecting type mission profile.

Multiple ARM mission / Prospector

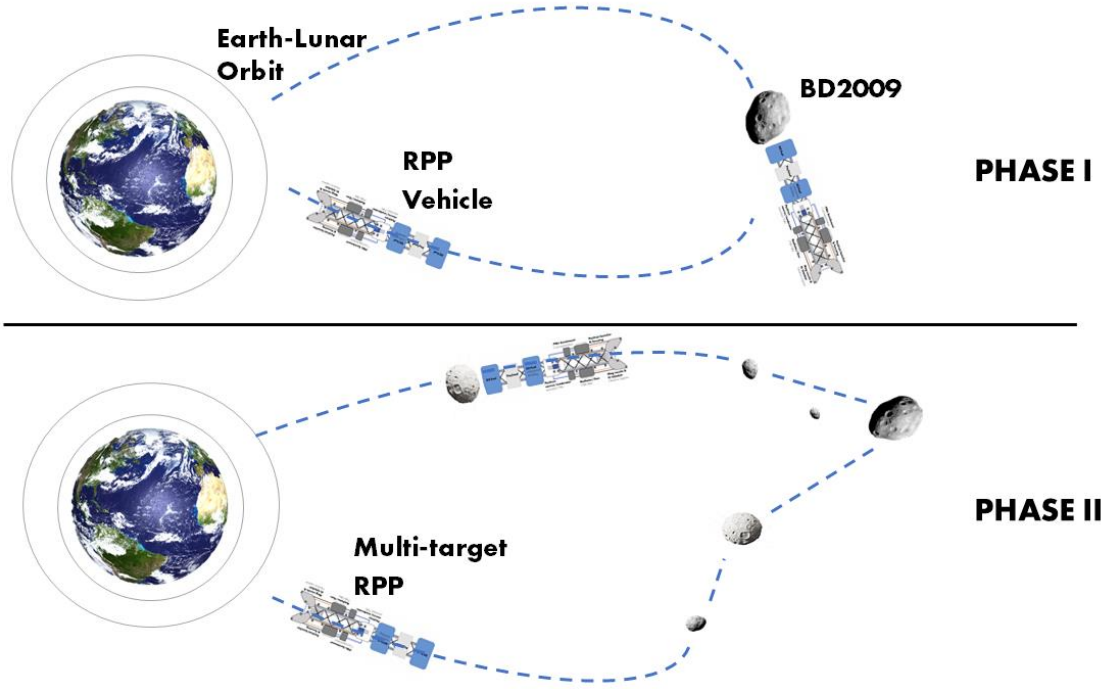

Figure 73. Mission Concept Development

The focus of the Phase I work was to compare the proposed RPP propulsion system to the ARM mission. Phase II work will consider the possibility of multiple ARM missions for a single RPP powered spacecraft. This requires considering more complicated trajectories beyond the original ARM mission.

Additionally, a prospector mission profile would be considered. Here, an instrument payload would be included to analyze "on the go" to preferentially determine the best objects to capture. The analysis would be based on an initial trajectory and include the possibility of excursions to objects of interest as they presented themselves. Of particular note would be the addition of a return mass, which would change as the mission progressed.

Integration and Regulatory

Integration of the subsystems, based on updated work on the key enabling technologies, will be investigated to decrease the uncertainty on the reference vehicle SWAP. Following this work, integration of the reference design into candidate launch vehicles will be analyzed.

In the Phase I analysis, a minimum activity of ^{79}Kr was determined to start the fuel cycle (~2Ci). Since the half-life of ^{79}Kr is 35 hours, the amount of ^{79}Kr required to be loaded on the spacecraft prior to

launch to LEO given typical launch scheduling will be determined in Phase II. The associated regulatory procedures will be determined.

5. Acknowledgements

I would like to thank the NIAC Program Office for their support of a crazy idea – antimatter propulsion.

I would also like to acknowledge helpful discussions with the NIAC External Council and other NIAC Fellows over the course of this year. Discussions with Professor Peter Hosemann and Professor Karl van Bibber at University of California Department of Nuclear Engineering were beneficial in hashing out some of the details of the Krypton-based neutron capture fuel cycle. Thanks to Ken York at YD Visual who provided useful animations of the RPP concept. I also wish to thank Dr. Lubos Brieda for his significant contribution on the fusion ignition aspects of this report and for his patience in dealing with positron physicists. Many thanks to Bridgette Hyde for assistance in editing this report.

Finally, thank you to the efforts of a myriad of scientists, engineers, students, tinkerers, and makers that this work builds on - from Tsiolkovsky and Goddard to the unbounded future generations - let's go mine asteroids and bring humanity to the stars.

-R.Weed

6. References

[1] E. Sanger, "Zur Theorie der Photonenrakteten", Ing. Arch. 21, 213, 1953.

[2] Bohm, W. L, Propulsion by light: visions of the German pioneer Eugen Saenger, *Proc. SPIE* 5777, XV International Symposium on Gas Flow, Chemical Lasers, and High-Power Lasers, 986 (April 01, 2005)

[3] Krause-Rehberg, Reinhard, and Hartmut S. Leipner. *Positron annihilation in semiconductors: defect studies*. Vol. 127. Springer Science & Business Media, 1999.

[4] Danielson, J. R., et al. "Plasma and trap-based techniques for science with positrons." *Reviews of Modern Physics* 87.1 (2015): 247.

[5] Smith, G. NIAC Phase I Final Report "Positron Propelled and Powered Space Transport Vehicle for Planetary Missions"

[6] McNutt, A Realistic Interstellar Explorer, NIAC 7600-039 Final Report, 2002

[7] Kramer, K. et al "Antimatter-initiated microfusion: Direct energy conversion for propulsion applications" AIP Conference Proceedings, 608, 787-788 (2002)

[8] Tabak, Review of Progress in Fast Ignition, Physics of Plasmas 2005

[9] Ditmire 1999 Nuclear fusion from explosions of femtosecond laser-heated Deuterium clusters NATURE VOL 398

[10] Weed, R. et al "Positron Catalyzed Fusion Propulsion and Corresponding Methods", US2015 62183187

[11] Weed, R. et al "Positron propulsion for Interplanetary and Interstellar Travel" Proceedings of the Foundations of Interstellar Studies Workshop at City Tech, CUNY, *Journal of the British Interplanetary Society*, Accepted Oct 2018

[12]. Morioka, "Nuclear Fusion Triggered by Positron Annihilation in Deuterated Metals", Il Nuovo Cimento, Vol107a, N12, 1994

[13] Huke, A., et al. "Enhancement of deuteron-fusion reactions in metals and experimental implications." *Physical Review C*78.1 (2008): 015803.

[14] Raghavan, R.S., Mills, A. "Nuclear Excitation by positron annihilation: Comments on theory vs experiment" Physical Review C Vol 24 Num 4, October 1981

[15] Present, R.D., Chen, S.C. "Nuclear Disintegration by Positron-K Electron Annihilation," Physical Review, Vol 85, Num 3, February 1952

[16] Cassidy, D.B., et al, "Resonant versus nonresonant nuclear excitation of 115In by positron annihilation," Physical Review C, Vol 64 054603, October 2001

[17] Ljubičić, A "Nuclear excitation in 176Lu by positron annihilation on K-shell electrons" Journal of Radioanalytical and Nuclear Chemistry V 272 2007

[18] Unpublished data from positron annihilation catalyzed fusion reaction rate measurement (see Appendix).

[19] Huba, Joseph D. *NRL: Plasma formulary*. No. NRL/PU/6790--04-477. NAVAL RESEARCH LAB WASHINGTON DC BEAM PHYSICS BRANCH, 2004.

[20] Weed, et al Array Structures for Field Assisted Positron Moderation and Corresponding Methods WO Patent App. PCT/US2012/042,049

[21] Lynn, K.G. and B.T.A. Mckee, *Some Investigations of Moderators for Slow Positron Beams*. Applied Physics, 1979. 19(3): p. 247-255.

[22] Al-Qaradawi, I.Y., P.A. Sellin, and P.G. Coleman, *Tests of a diamond field-assisted positron moderator*. Applied Surface Science, 2002. 194(1-4): p. 29-31.

[23] Merrison, J.P., et al., *Field Assisted Positron Moderation by Surface Charging of Rare-Gas Solids*. Journal of Physics-Condensed Matter, 1992. 4(12): p. L207-L212.

[24] Lipson et al, Transport and Magnetic Anomalies below 70K in a Hydrogen Cycled Pd Foil with a Thermally Grown Oxide PHYSICAL REVIEW B 72, 212507 2005

[25] Winterberg, F "Ultra-dense Deuterium and cold fusion claims", Physics Letters A, Volume 374, Issue 27, 14 June 2010, Pages 2766-2771

[26] Holmlid, L. "High-charge Coulomb explosions of clusters in ultra-dense Deuterium D(−1)", International Journal of Mass Spectrometry, Volume 304, Issue 1, 15 June 2011, Pages 51-56

[27] Andersson, P. "Ultra-dense Deuterium: A possible nuclear fuel for inertial confinement fusion (ICF)", Physics Letters A, Volume 373, Issue 34, 17 August 2009, Pages 3067-3070

[28] Holmlid, L. "Laser-induced fusion in ultra-dense Deuterium D(−1): Optimizing MeV particle emission by carrier material selection", Nuclear Instruments and Methods in Physics Research Section B: Beam Interactions with Materials and Atoms, Volume 296, 1 February 2013, Pages 66-71

[29] Ditmire, Todd, et al. "Nuclear fusion from explosions of femtosecond laser-heated Deuterium clusters." *Nature* 398.6727 (1999): 489-492.

[30] Unpublished data from laser pulse initiated coulomb explosion in dense Deuterium clusters from time of flight (TOF) spectrometer with Micro-channel plate (MCP) detector and variable bias drift tube.

[31] Reynolds, Thaine W. "Effective specific impulse of external nuclear pulse propulsion systems." (1972).

[32] Gilland, James H., et al. "Magnetic-Nozzle Studies for Fusion Propulsion Applications: Gigawatt Plasma Source Operation and Magnetic Nozzle Analysis." (2004).

[33] Hoffman, R., et al. *Neutron and charged-particle induced cross sections for radiochemistry in the region of bromine and krypton*. No. UCRL-TR-205563. Lawrence Livermore National Laboratory (LLNL), Livermore, CA, 2004

[34] Merrison, J. P., et al. "Field assisted positron moderation by surface charging of rare gas solids." *Journal of Physics: Condensed Matter* 4.12 (1992): L207.

[35] Mills Jr, A. P. "Physics with many positrons." *Rivista del Nuovo Cimento della Societa Italiana di Fisica* 34.4 (2011): 151-252.

[36] Mills Jr, A. P. "Suitability of 79 Kr as a Reactor-Based Source of Slow Positrons." *Nuclear science and engineering* 110.2 (1992): 165-167.

[37] Strange, Nathan, et al. "Overview of mission design for NASA asteroid redirect robotic mission concept." (2013).

[38] Schmidt, G. R., et al. "Antimatter requirements and energy costs for near-term propulsion applications." *Journal of Propulsion and Power* 16.5 (2000): 923-928.

[39] Gaidos, Gerard, et al. "AIMStar: Antimatter initiated microfusion for pre-cursor interstellar missions." *Acta Astronautica* 44.2 (1999): 183-186.

[40] Baro, J., et al. "PENELOPE: an algorithm for Monte Carlo simulation of the penetration and energy loss of electrons and positrons in matter." *Nuclear Instruments and Methods in Physics Research Section B: Beam Interactions with Materials and Atoms* 100.1 (1995): 31-46. 99.

[41] Briesmeister, Judith F. "MCNPTM-A general Monte Carlo N-particle transport code." *Version 4C, LA-13709-M, Los Alamos National Laboratory* (2000)

[42] Mortensen, T., et al. "Manipulation of the magnetron orbit of a positron cloud in a Penning trap" *Physics of Plasmas* 20 (2013) 012124

[43] Cassidy, D. B., et al. "Accumulator for the production of intense positron pulses." *Review of scientific instruments* 77.7 (2006): 073106.

[44] Isaac, C. A., et al. "Compression of positron clouds in the independent particle regime." *Physical review letters* 107.3 (2011): 033201.

[45] Jah, Moriba, et al. "The General Mission Analysis Tool (GMAT): A New Resource for Supporting Debris Orbit Determination, Tracking and Analysis." *Fifth European Conference on Space Debris*. Vol. 672. 2009.

[46] Kammash, Terry, and David L. Galbraith. "Improved physics model for the gasdynamic mirror fusion propulsion system." *Journal of propulsion and power* 14.1 (1998): 24-28.

[47] "Asteroid Retrieval Feasibility Study," Keck Institute for Space Studies, April 2, 2012

[48] Intrepid-1 launch cost: http://rocketcrafters.space/products-services/intrepid-launcher-family/intrepid-1/

[49] Yoshizawa, Y., et al., Precision Energy Measurements of Positron-Annihilation Radiation. Journal of the Physical Society of Japan, 1984. 53(12): p. 4125-4128.

[50] Bellotti, R., et al., A Transition Radiation Detector for Particle Astrophysics Experiments Using Low-Power Consumption Electronics. Nuclear Instruments & Methods in Physics Research Section a-Accelerators Spectrometers Detectors and Associated Equipment, 1992. 323(1-2): p. 71-77

[51] Dirac, P.A.M., The principles of quantum mechanics. The international series of monographs on physics. 1930, Oxford,: The Clarendon Press. 257

[52] Anderson, C.D., The Apparent Existence of Easily Deflectable Positives. Science 1932.

[53] Andersen, C.D., The Positive Electron. Physical Review, 1933. 43(491).

[54] Chehab, R. *Positron Sources.* in *CAS* 1994

[55] Madansky, L. and F. Rasetti, An Attempt to Detect Thermal Energy Positrons. Physical Review, 1950. 79(2): p. 397-397

[56] Cherry, W., PhD dissertation, in Princeton University1958

[57] Mills, A.P. and E.M. Gullikson, *Solid Neon Moderator for Producing Slow Positrons.* Applied Physics Letters, 1986. **49**(17): p. 1121-1123.

[58] Schultz, P.J. and K.G. Lynn, *Interaction of positron beams with surfaces, thin films, and interfaces.* Reviews of Modern Physics, 1988. **60**(3): p. 701

[59] Lynn, K.G. and B.T.A. Mckee, *Some Investigations of Moderators for Slow Positron Beams.* Applied Physics, 1979. **19**(3): p. 247-255.

[60] Al-Qaradawi, I.Y., P.A. Sellin, and P.G. Coleman, *Tests of a diamond field-assisted positron moderator.* Applied Surface Science, 2002. **194**(1-4): p. 29-31.

[61] M. Ahmadi et al. (ALPHA Collaboration), *Enhanced Control and Reproducibility of Non-Neutral Plasmas*, Phys. Rev. Lett. 120, 025001 – Published 8 January 2018

[62] Feynman, R.P., Mathematical Formulation of the Quantum Theory of Electromagnetic Interaction. Physical Review, 1950. 80(3): p. 440-457.

[63] R. Prokopec, et al, "Suitability of coated conductors for fusion magnets in view of their radiation response", Supercond. Sci. Technol. 28 014005 (2014)

[64] J. Emhofer, M. Eisterer and H. W. Weber, "Stress dependence of the critical currents in neutron irradiated (RE)BCO coated conductors", Supercond. Sci. Technol. 26 035009 (2013)

[65] G. Miley X. Yang, Fusion Sci. Technol., 56 (1), 395 (2009).

[66] A. Lipson et al., Physics Letters A, 339 (3-5), 414 (2005).

[67] A. Lipson et al., Physical Review B, 72 (21), 212507 (2005).

[68] L. Holmlid, H. Hora, G. Miley et al., Laser and Particle Beams, 27 (03), 529 (2009).

[69] Y. E. Kim, Naturwissenschaften, 96 (7), 803 (2009).

[70] Lewis R.A. 1990 An antiproton catalyst for inertial confinement fusion propulsion Proc. AIAA/SAE/ASME/ASEE 26th Joint Propulsion Conf. (Orlando, FL,16–18 July 1990)

[71] Smith G.A. 1997 Antiproton-catalyzed microfission/fusion propulsion systems for exploration of the outer solar system and beyond Technical Interchange Meeting on the Use of Fusion Energy for Space Propulsion (NASA Marshall Space Flight Center, Hunstville AL, 25–26 March 1997

[72] Gaidos G. et al 1998 AIMStar: antimatter initiated, microfusion for precursor interstellar missions 2nd IAA Symp. on Realistic Near-Term Advanced Scientific Space Mission (Aosta, Italy, 29 June–1 July 1998)

[73] Chen, Hui, et al. "Relativistic positron creation using ultraintense short pulse lasers." Physical review letters 102.10 (2009): 105001.

[74] LeMoyne, Robert. "Positron Induced Fusion Pulsed Space Propulsion through an Ultra-Intense Laser." Journal of Applied Mathematics and Physics 5.04 (2017): 813.

[75] Meyer, Mike, et al. "In-space propulsion systems roadmap." National Aeronautics and Space Administration, Office of the Chief Technologist (2012).

[76] Makhov, A.F., The Penetration of Electrons into Solids .1. The Intensity of an Electron Beam, Transverse Paths of Electrons. Soviet Physics-Solid State, 1961. 2(9): p. 1934-1941.

[77] Vehanen, A., et al., Profiling Multilayer Structures with Monoenergetic Positrons. Physical Review B, 1987. 35(10): p. 4606-4610

[78] Schultz, P.J., et al., Channeling Effects on Positron Transmission through Thin-Crystals. Physical Review B, 1988. 38(10): p. 6369-6379.

[79] J. C. Fernandez, B. J. Albright , K. A. Flippo et al., Journal of Physics: Conference Series (2), 022051 (2008)

[80] Weed, R., A New Beamline for Positron Annihilation Lifetime Spectroscopy, Ph.D. Dissertation, The Australian National University, ARC Centre for Antimatter-Matter Studies, 2011

[81] Danielson, J. R., Dubin, D. H. E., Greaves, R. G. & Surko, C. M. Plasma and trap-based techniques for science with positrons. Rev. Mod. Phys. 87, 247–306 (2015)

[82] T. J. Murphy and C. M. Surko, Phys. Rev. A 46, 5696 (1992)

[83] Marjanović, S. et al. A CF 4 based positron trap. J. Phys. B At. Mol. Opt. Phys. 49, 215001 (2016)

[84] Murtagh, D. J. A positron buncher-cooler. Eur. Phys. J. D 68, 213 (2014)

[85] Greaves, R. G., and C. M. Surko. "Practical limits on positron accumulation and the creation of electron-positron plasmas." AIP Conference Proceedings. Vol. 606. No. 1. AIP, 2002

[86] Matsuda, Nobuo, et al. "A magnetic thrust chamber design for a laser fusion rocket based on impact fast ignition scheme." J. Plasma Fusion Res. Series 8 (2009): 1602-1605.

[87] Andersson, Patrik U., Leif Holmlid, and Stephan Fuelling. "Search for superconductivity in ultra-dense Deuterium D (– 1) at room temperature: depletion of D (– 1) at field strength> 0.05 T." Journal of superconductivity and novel magnetism 25.4 (2012): 873-882.

[88] Atzeni, Stefano, Jurgen Meyer-Ter-Vehn, and Jürgen Meyer-ter-Vehn. The Physics of Inertial Fusion: BeamPlasma Interaction, Hydrodynamics, Hot Dense Matter. Vol. 125. Oxford University Press on Demand, 2004.

[89] Tabak, Max, et al. "Ignition and high gain with ultrapowerful lasers." Physics of Plasmas 1.5 (1994): 1626-1634

[90] Hubbell, John H., and Stephen M. Seltzer. Tables of X-ray mass attenuation coefficients and mass energy-absorption coefficients 1 keV to 20 MeV for elements Z= 1 to 92 and 48 additional substances of dosimetric interest. No. PB-95-220539/XAB; NISTIR-5632. National Inst. of Standards and Technology-PL, Gaithersburg, MD (United States). Ionizing Radiation Div., 1995.

[91] Shaoshuai Liu , Zhenhua Jiang , Lei Ding , Haifeng Zhu , Qi Huang , Yinong Wu , Impact of operating parameters on 80 K pulse tube cryocoolers for space applications, International Journal of Refrigeration (2018)

[92] Radebaugh, Ray. "Development of the pulse tube refrigerator as an efficient and reliable cryocooler." Proceedings of Institute of Refrigeration. Vol. 96. 2000

[93] Greaves, R. G., and C. M. Surko. "Practical limits on positron accumulation and the creation of electron-positron plasmas." AIP Conference Proceedings. Vol. 606. No. 1. AIP, 2002

[94] Cassidy, D. B., et al. "Accumulator for the production of intense positron pulses." Review of scientific instruments 77.7 (2006): 073106.

[95] Danielson, J. R., et al. "Plasma and trap-based techniques for science with positrons." Reviews of Modern Physics 87.1 (2015): 247.

[96] Wiedemann, H., Particle accelerator physics. 2007, New York: Springer.

[97] Mills, A.P., Time Bunching of Slow Positrons for Annihilation Lifetime and Pulsed Laser Photon-Absorption Experiments. Applied Physics, 1980. 22(3): p. 273-276

[98] Schodlbauer, D., et al., A Pulsing System for Low-Energy Positrons. Nuclear Instruments & Methods in Physics Research Section B-Beam Interactions with Materials and Atoms, 1988. 34(2): p. 258-268

[99] T. R. Weber, J. R. Danielson, and C. M. Surko, Phys. Plasmas 17, 123507 (2010),

[100] Hurst, N. C., J. R. Danielson, and C. M. Surko. "Magnetic field extraction of trap-based electron beams using a high-permeability grid." Physics of Plasmas 22.7 (2015): 073503.

[101] Simpson, James C., et al. "Simple analytic expressions for the magnetic field of a circular current loop." (2001)

[102] Parkins, William E. "The uranium bomb, the calutron, and the space-charge problem." Phys Today 58.5 (2005): 45-51

[103] Olivares, Ignacio E., et al. "Lithium isotope separation with tunable diode lasers." Applied optics 41.15 (2002): 2973-2977

[104] Akatsuka, H., et al. "An Experimental Study of Noble Gas Isotope Separation by DC ArcDischarge." Contributions to Plasma Physics 39.6 (1999): 557-570.

[105] Ezoubtchenko, A., et al. "Measurements of plasma parameters in the direct current discharge for isotope separation." Plasma Sources Science and Technology 7.2 (1998): 136.

[106] Bader K and Roth M W 2003 Simulated behavior of krypton/argon mixtures confined between two graphite slabs: new terrain for familiar systems Surf. Sci 538 30-44.

[107] Cohen, Karl. "The theory of isotope separation as applied to the large-scale production of U235." (1951)

[108] Young, David A. Phase diagrams of the elements. Univ of California Press, 1991

[109] Phipps, C., et al. "Micropropulsion using a laser ablation jet." Journal of Propulsion and Power 20.6 (2004): 1000-1011

[110] Greaves, R. G. & Surko, C. M. Positron trapping and the creation of high-quality trap-based positron beams. Nucl. Instruments Methods Phys. Res. Sect. B Beam Interact. with Mater. Atoms 192, 90–96 (2002)

[111] Murtagh, D. J. A positron buncher-cooler. Eur. Phys. J. D 68, 213 (2014)

[112] Marjanović, S. et al. A CF 4 based positron trap. J. Phys. B At. Mol. Opt. Phys. 49, 215001 (2016)

[113] Linstrom, Peter J., and William G. Mallard. "The NIST Chemistry WebBook: A chemical data resource on the internet." Journal of Chemical & Engineering Data 46.5 (2001): 1059-1063.

[114] Ferreira, A. G. M., and L. Q. Lobo. "The sublimation of argon, krypton, and xenon." The Journal of Chemical Thermodynamics 40.12 (2008): 1621-1626.

[115] Frigo, A. A. Heat-shield design for glovebox applications. No. ANL/CMT/CP-96761. Argonne National Lab., IL (US), 1998

[116] Heshmat, Hooshang, James F. Walton, and Andrew Hunsberger. "Oil Free 8 kW High-Speed and High Specific Power Turbogenerator." ASME Turbo Expo 2014: Turbine Technical Conference and Exposition. American Society of Mechanical Engineers, 2014.

[117] Craven, Paul, et al. "Lightweight Damage Tolerant Radiators for In-Space Nuclear Electric Power and Propulsion." (2014).

[118] Billette, J., et al. "A 30 T pulsed magnet with conical bore for synchrotron powder diffraction." Review of Scientific Instruments 83.4 (2012): 043904.

[119] Mazanek, Daniel D., et al. "Enhanced gravity tractor technique for planetary defense." (2015).

[120] Gupta, R., et al. "High-Field Solenoid Development for Axion Dark Matter Search at CAPP/IBS." IEEE Transactions on Applied Superconductivity 26.4 (2016): 1-5.

[121] Green, Michael. "Cooling and Cooling-down MgB2 and HTS Magnets using a Hydrogen Thermal Siphon Loop." (2014).

[122] V. J. Johnson Ed., A Compendium of the Properties of Materials at Cryogenic Temperature, Volume 1 Properties of Fluids, Pergamon Press, New York NY, (1961)

[123] Green, Michael. "Cooling and Cooling-down MgB2 and HTS Magnets using a Hydrogen Thermal Siphon Loop." (2014).

[124] C. D. Orth, VISTA – A Vehicle for Interplanetary Space Transport Application Powered by Inertial Confinement Fusion, UCRL-LR-110500 (2003)

[125] N. Sakaguchi, Y. Kajimura, H. Nakashima, Thrust Efficiency Calculation for Magnetic Nozzle in Laser Fusion Rocket, Trans. Jpn. Soc. Aeronaut. Space Sci. 48 (2005), pp.180–182.

[126] Y. Kajimura, R. Kawabuchi and H. Nakashima, Control Techniques of Thrust Vector for Magnetic Nozzle in Laser Fusion Rocket, Fusion Engineering and Design. 81 (2006), pp. 2871-287

[127] Larson, Wiley J., and James Richard Wertz. Space mission analysis and design. No. DOE/NE/32145-T1. Torrance, CA (United States); Microcosm, Inc., 1992.

[128] Andersson, P., Lonn, B. & Holmlid, L. (2011). Efficient source for the production of ultra-dense Deuterium D(-1) for laser-induced fusion (ICF). Rev. Sci. Instrum. 82, 013503.

[129] Greenwald, M., et al. The high-field path to practical fusion energy. PSFC Report, 2018.

[130] Villani, Stelio. "Uranium enrichment." (1979).

[131] Broschart, Stephen B., et al. "The small-body dynamics toolkit and associated close-proximity navigation analysis tools at JPL." AAS Guidance and Control Conference. 2015.

[132] Acton, Ch, et al. "Extending NASA's SPICE ancillary information system to meet future mission needs." SpaceOps 2002 Conference. 2005.

[133] Asteroid Retrieval Mission Concept – Trailblazing Our Future in Space and Helping to Protect Us from Earth Impactors D. D. Mazanek, J. R. Brophy, R. G. Merrill IAA-PDC13-04-14 Planetary Defense Conference 2013

[134] Le Roux, Marie-Noëlle, and Hans Wilhelmsson. "Simultaneous diffusion, reaction and radiative loss processes in plasmas: numerical analysis with application to the dynamics of a fusion reactor plasma." Physica Scripta 45.2 (1992): 188

[135] Hughes, Steven P. "General Mission Analysis Tool (GMAT)." (2016).

[136] Brown, Benjamin L. "A cobalt 58 'slow positron generator'." Applied surface science 116 (1997): 104-107.

Appendix A. Fabrication of dense Deuterium loaded thin-film fuel

Recent work on dense states of Deuterium in metal substrates could lead to a further increase in the positron/Deuterium overlap and therefore fusion rate, leading to a corresponding increase in thrust. Ultra-dense Deuterium states on the surface and subsurface of Palladium have been reported by two groups and correspond to a number density between 10^{27} and 10^{29} cm^{-3}. [24-27]. In fact, the University of Gothenburg group reported on laser induced fusion events in these dense states on the surface of metals [28].

This work on dense Deuterium, in addition to earlier work on laser-initiated coulomb explosion in D clusters [29] inspired us to not only experimentally verify these results using much improved particle detection schemes, but also to investigate a regime of positron flux that can produce similar coulomb explosion fusion process in dense D clusters and surface states. Utilizing these ultra-dense states results in significantly higher thrust for a given amount of positron radioisotope by relaxing the conditions necessary to produce a fusion burn (see section 3.2).
The propulsion system performance depends not only on the cold positron intensity, but also on the fuel (Deuterium) density that can be achieved. In order to maximize thrust levels for a given amount of positron source activity, a significant effort over the past year focused on creating dense Deuterium clusters using a doped Iron-Oxide catalyst on a thin-film metal substrate.

To this end, we developed a pulsed (5ns) laser (1,200 mJ) time-of-flight (TOF) spectrometer integrated with an ultra-high vacuum test chamber that included heated Deuterium catalyst injector target, Scintillator / Photomultiplier Tube (PMT) and Microchannel Plate (MCP) detectors for fast timing resolution of emitted energetic particles, as shown in Fig. 73. In these experiments, the laser pulse ionizes the electrons in the Deuterium clusters, initiating a Coulomb Explosion (CE) process where the ion cores repel each other. The energy of the resulting ions reveals the spacing between adjacent ions in the Deuterium clusters.

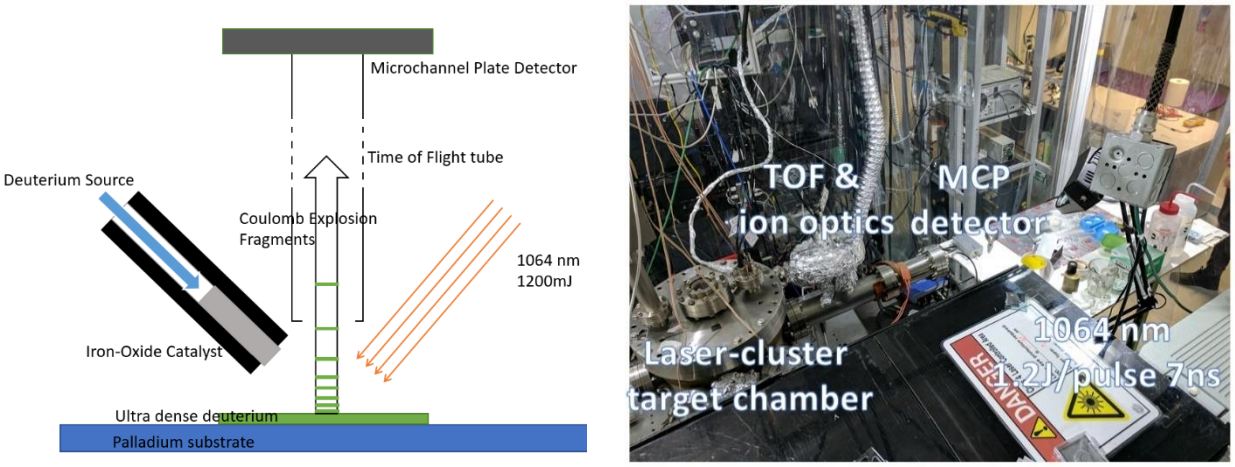

Figure 73. Experimental setup for Laser-TOF studies of dense Deuterium production.

Initial results indicate production of ultra-dense Deuterium (UDD) clusters with interatomic spacing of several picometers (See Fig. 74 below). These experiments continue in order to optimize UDD production based on several factors (mass flow rate, injector temperature, substrate geometry, etc). This will allow us the possibility to create fuel densities several orders of magnitude higher than standard ICF Deuterium targets and greatly increase propulsion system performance.

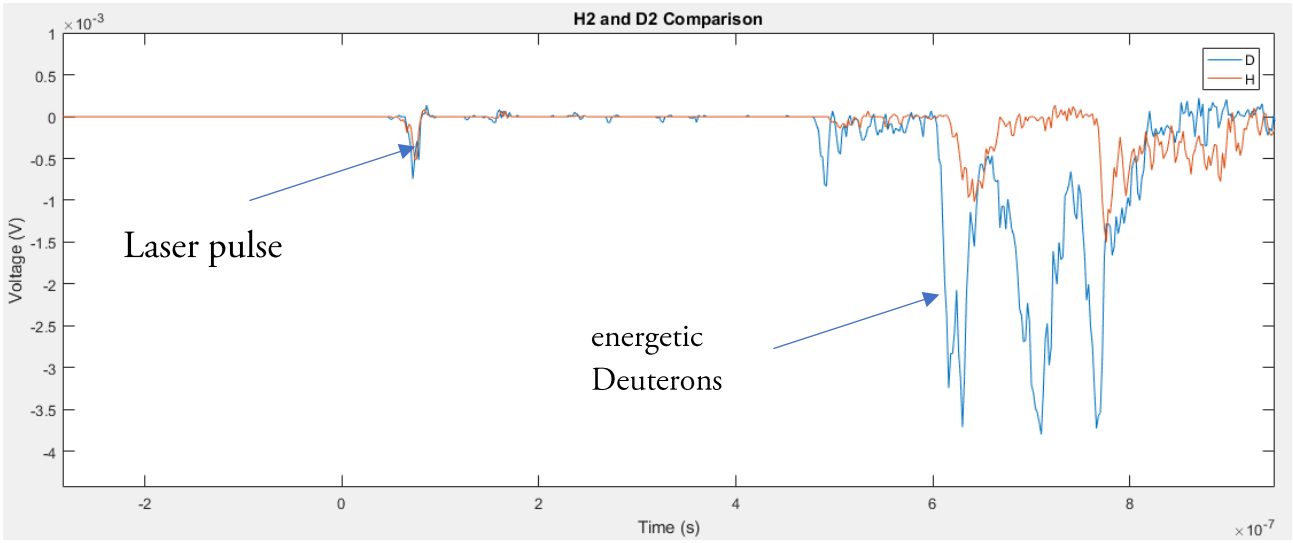

Figure 74. TOF data from laser pulse spectrometer.

By changing the ion transit energy, we can determine mass as well as initial kinetic energy from the coulomb explosion process. Ion optics inside the time of flight tube reject electrons, ensuring that the measured ion energy range is between 100-800eV. 200 shot average, 1.2J/pulse. Fig. 74 above shows data from single stack 50mm, fast anode, 40:1 gain MCP from Tectra, indicating interatomic spacing in the range of a few pm.

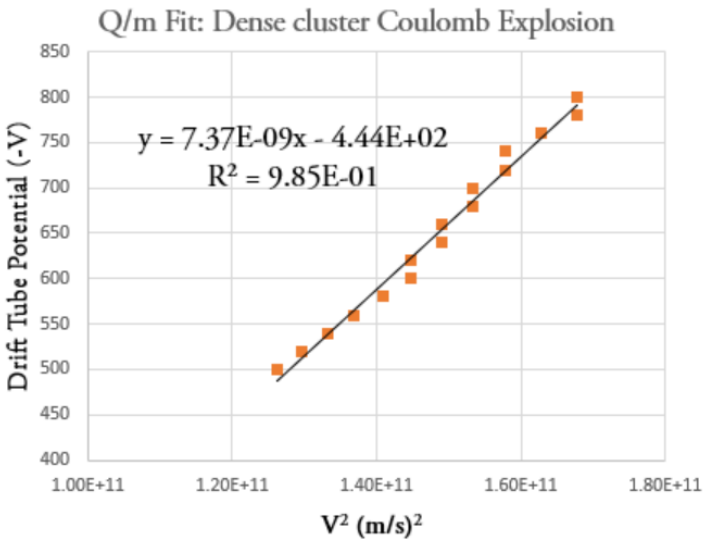

Figure 75. Charge to mass ratio TOF results from the D peak in laser.

The data shown in Fig. 75 are the first charge-to-mass ratio measurements indicating 1-2amu particles at 444eV exiting clusters. These results seem to confirm the CE process results from references [25-28].

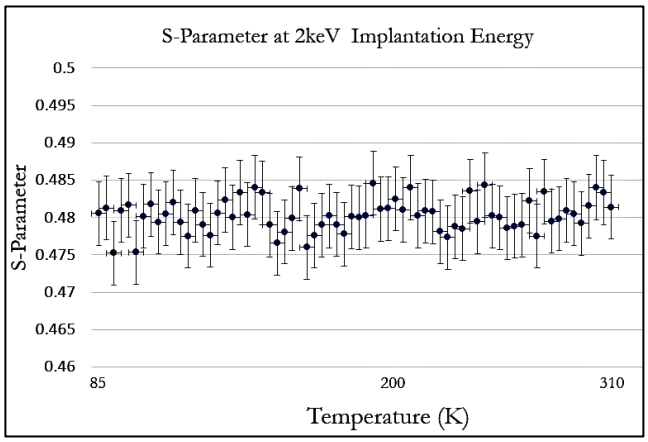

Fig.75 S-parameter from Positron annihilation Doppler Broadening Spectroscopy (DBS) showing Deuterium fuel stability on Palladium substrate subsurface over a wide temperature range

In addition to density, the stability of the Deuterium fuel over a wide range of operating temperatures is important in a space propulsion application. Fuel samples fabricated at our Livermore facility have been measured at the positron beamline at Washington State University (WSU). There we have characterized the Deuterium loading using depth profiling (10nm to 1um) with a low-flux positron beam at various sample temperatures (80K to 300K).

This work is part of the larger effort at to provide an analysis of thin film component and fuel stability as a function of thermal environment and other factors relevant to the spacecraft environment (ionizing radiation, surface contaminants).

Appendix B. Measurements of Annihilation Momentum Transfer Probability

Our propulsion concept relies on the transfer of energy from positron annihilation to surrounding dense Deuterium clusters, causing Deuterium-Deuterium (DD) fusion reactions. An experimental measurement of this momentum transfer probability is key to determining feasibility of the propulsion concept. An initial experiment has been conducted at Positron Dynamics' Livermore lab to determine the upper limit on the PCF cross section and momentum transfer probability. This experiment used a low activity source (30uCi) of positrons.

Deuterium-Deuterium fusion reactions will release energetic (2.5MeV) neutrons and are a tell-tale sign of fusion reactions. To measure the cross section for PCF reaction, a simple experiment was set up to measure fusion neutrons from a low-activity positron source over the period of ~month. This experiment was based on un-cooled Na22 radioisotope source of positrons surrounded by (50) 5um Deuterium loaded Pd thin films. We make the assumption that all of the emitted positrons thermalize

inside of the Pd films as the thermalization length of un-moderated positrons from Na22 is <250um. The electrochemical/gas loading of Pd thin films produces approximately 0.7 loading fraction over entire Pd volume, which means every positron is likely to diffuse to a defect site containing one or more Deuterium atoms (saturation trapping).

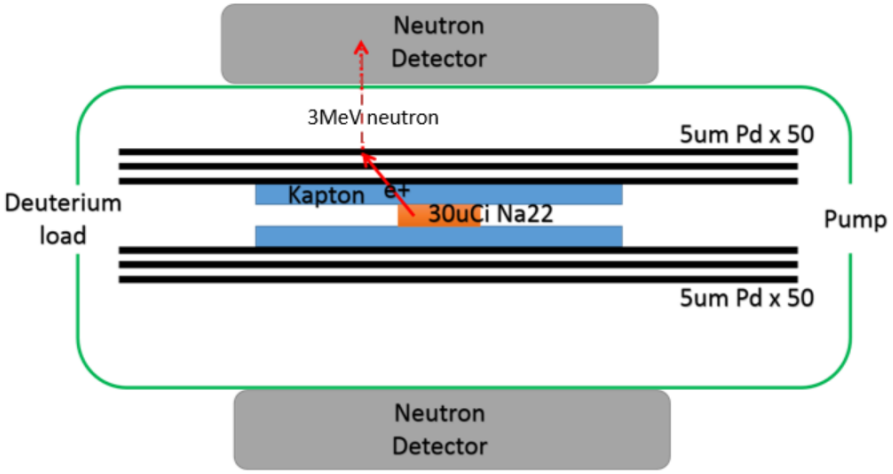

Figure 76. Experimental setup for long counter neutron detection of PCF reactions.

Background runs were taken over the same period without the Na22 installed. Results over the month-long acquisition time a neutron signal of approximately 0.1mrem/hr over a background signal of <0.01mrem/hr. Although the statistical uncertainty might be as much as +/- 50%, we can estimate the positron catalyzed momentum transfer probability per positron-electron annihilation of R=0.1, higher than predicted in reference [12]. The erratic, yet positive neutron signal may be due to the neutron detection method (super heated droplet bubble type). More tests are required (using higher activity source and higher density Deuterium) in order to reduce the uncertainty, however, this cross section is more than sufficient for PCF to produce a viable propulsion system.

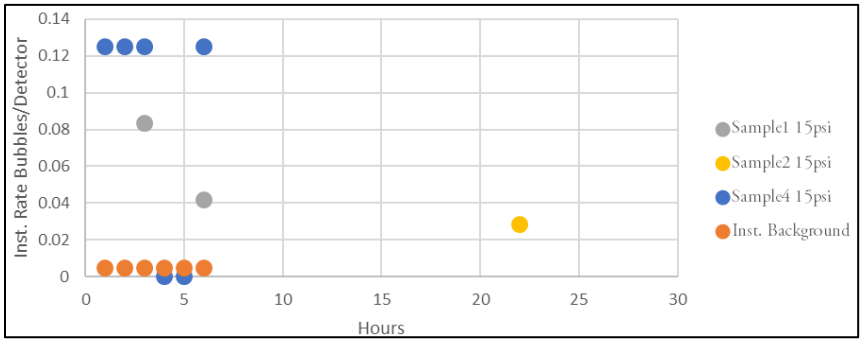

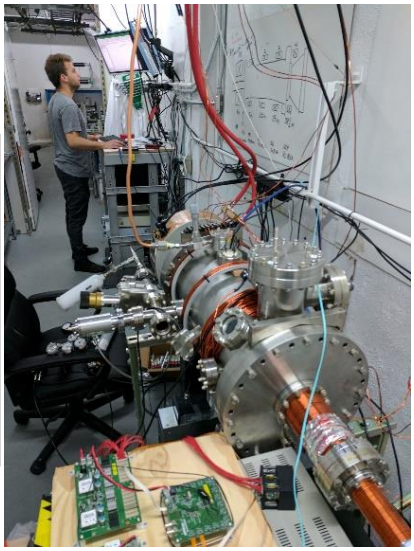

Figure 77. Measurement of the annihilation momentum transfer probability

Appendix C. Positron Moderation Estimates

When positrons are born, they are extremely energetic or 'hot' (mean energy ~250keV) and thus, difficult to control. One significant challenge to date is the ability to control these very hot positrons using realistic electric and magnetic fields. Before the positrons can be used as such, they must be cooled down to <keV energies in a process called moderation. The efficiency for the moderation process to date has been <1%. Through a grant from the Thiel Foundation's Breakout Labs, Positron Dynamics has developed new methods to increase moderation efficiency by several orders of magnitude [20], combining a technique called Field-assisted-moderation [21-23] in wide bandgap semiconductor (Silicon Carbide) arrays with a charged particle extraction technique using crossed electric and magnetic fields (ExB drift). This moderator will allow for production of intense and focused pulses of positrons that are able to deposit substantial amounts of power into fuel targets.

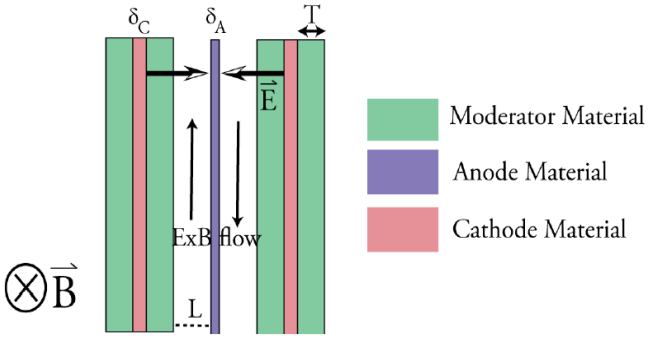

Figure 78. Planar Array extraction concept.

In this moderation process, strong electric fields applied to several layers of wide-bandgap semiconductor (GaAs or SiC) material cause thermal positrons to drift toward moderator surfaces. Once the positrons are emitted, an external magnetic field produces an ExB drift in order to extract cold positrons from between moderator surfaces.

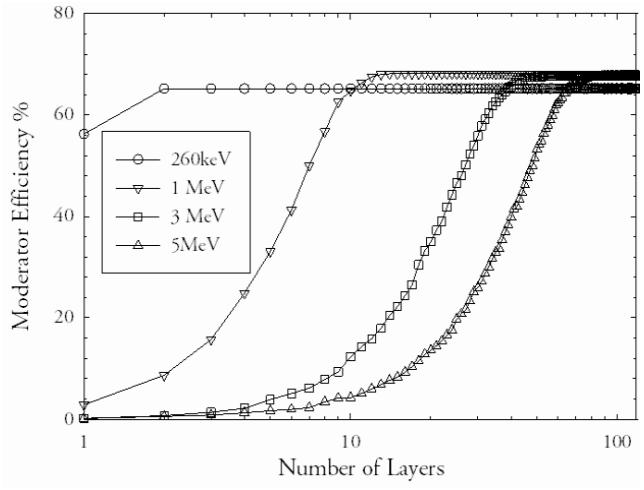

Fig. 79 Array moderator simulation results, using SRIM and GEANT4

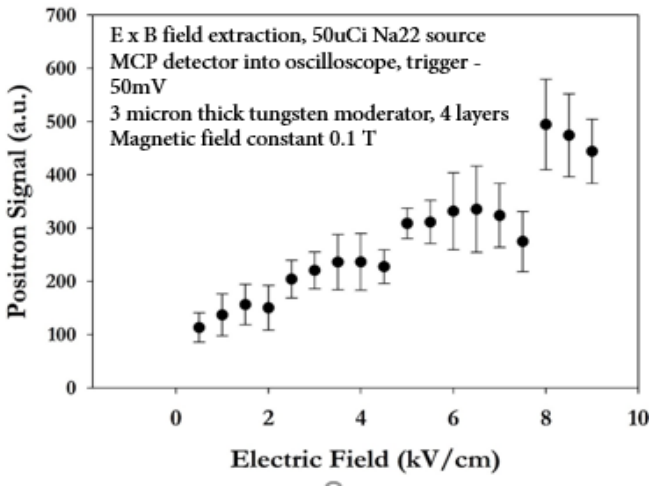

Fig. 80. Array moderator ExB extraction Proof of concept results.

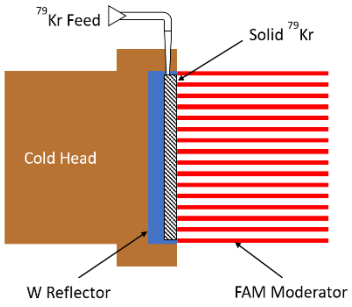

Fig.81 SiC Moderator Array.

At our Livermore facility, Positron Dynamics created and tested several successful iterations of the moderator array. Above, experimental results for ExB extraction in a Tungsten array moderator fabricated on site. Next iterations will be constructed using semiconductor fabrication techniques that guarantee structural repeatability and consistency. These structures are produced at Minnesota Nanofabrication Center (MNF) by JCap LLC, a contractor of Positron Dynamics, and successfully tested at our Livermore facility. We are continuing to push this technology towards 60% efficiency (see Fig. 79) by leveraging advanced manufacturing opportunities at our existing contracted facility at MNF.

Appendix D. Ignition Models

On the fundamental level, the operation of the propulsion system is based on a positron annihilating a Deuterium valence electron, leaving behind an energetic 1.02 MeV Deuterium ion (a deuteron). This deuteron then undergoes collisions with the dense Deuterium fuel surrounding it. Some of these collisions may be energetic enough for the two nuclei to fuse. Fusion can lead to a production of tritium, or one of two isotopes of Helium. Fusion is an exothermic reaction, and hence it leads additional heating of the fuel and additional fusion reactions. At the same time, processes such as radiation, ionization, or the less energetic momentum transfer provide an energy loss mechanism. In order for the fusion burn to sustain itself, the energy created by the fusion reaction needs to dominate over the loss terms. To simplify the analysis, the annihilation process can be neglected, and we can assume that a population of energetic deuterons is being injected into an initially cold Deuterium layer. We can then use conservation equations to model the time evolution of species temperatures and densities. If spatial variation is neglected, this model leads to a zero-dimensional approximation, in which the control volume is a single “fusion cell”. This is illustrated in Figure 82. We consider the rate of energy flowing into, and out of the system, and use it compute the evolution of temperatures and densities of the material inside the cell. Due to the zero-dimensional nature, this setup does not allow us to study processes that depend on spatial variation of properties, such as thermal conduction.

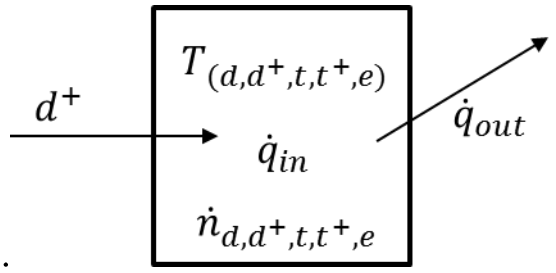

Figure 82a. Control volume for a zero-d model

Conservation Equations

From kinetic theory of gases, it is possible to arrive at a relationship stating that the mean per particle energy is

$$\langle E_i \rangle = \frac{N}{2} kT$$

where N is the number of degrees of freedom. Treating the hydrogen isotopes as a monoatomic gas with $N = 3$,[1] we have the following energy balance for a species "j"

$$\frac{\partial}{\partial t}\left(\frac{3}{2} n_j k T_j\right) + \nabla \cdot \left(\frac{3}{2} n_j \vec{v}_j k T_j + \vec{q}_j\right) + p_j \nabla \cdot \vec{v}_j = \sum S_j$$

The term on the right-hand side includes various elastic and inelastic energy transfer terms. For a zero-dimensional problem with no spatial variation, the divergence terms vanish, leaving us with

$$\frac{d}{dt}\left(\frac{3}{2} n_j k T_j\right) = S_a + S_f + S_e + S_{le} + S_i \equiv (\sum S)_j \quad (1)$$

The terms on the RHS correspond to energy input from annihilation (a), fusion (f), elastic energy transfer to other species €, line emission radiation (le), and ionization (i). The units of all terms are $J/(s \cdot m^3) \equiv W/m^3$. Some terms, such as ionization or radiation, will be negative as they correspond to energy loss. The partial derivative was replaced with a total derivative since there is no longer any spatial dependence. Similarly, mass conservation,

[1] This assumption may not be a valid for the ultra-dense material of interest here, however, the equation of state for this novel state of matter is an unexplored area.

$$\frac{\partial \dot{n}_j}{\partial t} + \nabla \cdot (n\vec{u}) = \dot{n}_j$$

with $\nabla \cdot (\quad) = 0$ leads to

$$\frac{dn_j}{dt} = \dot{n}_j \tag{2}$$

The term on the RHS captures the mass creation in chemical reactions, such as ionization. Besides the five species indicated in Fig. 82a, a complete model should also include positrons (e^+), electrons (e^-), and two isotopes of Helium, ^3He and ^4He. However, the positrons only serve to produce the initial population of deuterons through Deuterium valence electron - positron annihilation,

$$d + e^+ \rightarrow d^+ + 1.02\ MeV$$

This process can thus be skipped, reducing the number of equations by one. Electrons are not modeled as we assume the system is quasi-neutral. This may not be a perfectly valid assumption, since the fermion annihilation leads to a creation of ions without the corresponding neutralizing electron charge. Helium is not modeled as it is the product of fusion and does not undergo additional reactions of interest. We also terminate our simulation at an energetic ignition. The simulation is initialized with the cell containing some prescribed density of Deuterium atoms,

$$n_d(t = 0) = (n_d)_{initial}$$

Tritium density is initially set to zero,

$$n_t(0) = 0$$

Temperatures is initialized to

$$T_d(0) = T_t(0) = 273\ \mathrm{K}$$

We also assume that annihilation generates deuterons with uniform rate over some time period τ_{beam}. Nominally, $\tau_{beam} = 50\ \mathrm{ps}$ but case with $\tau_{beam} = 400\ \mathrm{ps}$ was also run. We set an injection deuteron density rate of change as

$$(\dot{n}_a)_{d^+} = \frac{\left(n_{final}\right)_{d^+}}{\tau_{beam}}$$

where $\left(n_{final}\right)_{d^+}$ is some desired annihilation-generated deuteron density after time τ_{beam}. $(\dot{n}_a)_{d^+}$ (units of $m^{-3}s^{-1}$) and $\left(n_{final}\right)_{d^+}$ (units m^{-3}) are two simulation inputs. The simulation is run for

$\tau_{sim} = 2000\, ps$ using 500,000 time steps. The deuteron injection switches off for $t > \tau_{beam}$. The temperature at the end of the simulation can be used to determine if the fusion reaction occurred.

Integration Scheme

Implementing the above model reduces to writing algorithms for the energy source terms and using some numerical algorithm to integrate Equations 1 and 2. These two equations can be combined into a single vector form

$$\frac{d\vec{f}}{dt} = \vec{b} \tag{3}$$

where

$$\vec{f} = \begin{bmatrix} n_{d^+}T_{d^+} \\ n_d T_d \\ n_t T_t \\ n_{t^+}T_{t^+} \\ n_{d^+} \\ n_d \\ n_t^+ \\ n_t \end{bmatrix} \text{ and } \vec{b} = \begin{bmatrix} (2/3k_b)(\sum S)_{d^+} \\ (2/3k_b)(\sum S)_d \\ (2/3k_b)(\sum S)_t \\ (2/3k_b)(\sum S)_{t^+} \\ \dot{n}_d \\ \dot{n}_d \\ \dot{n}_{t^+} \\ \dot{n}_t \end{bmatrix}$$

This system can be integrated in time using the fourth-order accurate Runge-Kutta scheme, RK4. We have

$$\vec{R}_0 = \vec{b}(\vec{f}^k), \qquad \vec{f}_1 = \vec{f}^k + \frac{\Delta t}{2}\vec{R}_0$$

$$\vec{R}_1 = \vec{b}(\vec{f}_1), \qquad \vec{f}_2 = \vec{f}^k + \frac{\Delta t}{2}\vec{R}_1$$

$$\vec{R}_2 = \vec{b}(\vec{f}_2), \qquad \vec{f}_3 = \vec{f}^k + \frac{\Delta t}{2}\vec{R}_2$$

$$\vec{R}_3 = \vec{b}(\vec{f}_3), \qquad \vec{f}^{k+1} = \vec{f}^k + \frac{\Delta t}{6}(\vec{R}_0 + 2\vec{R}_1 + 2\vec{R}_2 + \vec{R}_3)$$

While explicit, this scheme is more stable than a simple first-order forward Euler scheme. It allows us to utilize larger Δt time steps without introducing non-physical oscillations or negative densities or temperatures.

Energy Source Terms

Implementing the solver then involves writing equations for the energy and density source terms forming the RHS of Equation 3. In general, the energy sources rate is

$$(\sum S)_j = S_a + S_f + S_e + S_{le} + S_i$$

where the terms on the RHS correspond to annihilation, fusion, elastic (collisional) energy transfer with other species, line emission radiation, and energy lost to ionization. These terms are now described in detail.

Annihilation (D+ generation)

As noted earlier, annihilation is not modeled directly, and we use an inflow of energetic deuterons as a heat term,

$$(S_a)_{d^+} = (\dot{n}_a)_{d^+} \times 1.02MeV$$

This term is applied only to the d^+ population.

Fusion

Another source of energy is fusion, which is also the actual end goal of this model. There are three reactions of interest:

$$1, T(d,n)\,{}^4He: \qquad T + D \rightarrow n + {}^4He + 17.590\ MeV$$

$$2, D(d,p)T: \qquad D + D \rightarrow p + T + 4.03\ MeV$$

$$3, D(d,n)\,{}^3He: \qquad D + D \rightarrow n + {}^3He + 3.268\ MeV$$

The chemical reaction rates ($\#/m^{-3}$) for these reactions could be written as

$$k_{f1} = (n_t n_d)\langle\sigma v\rangle_{f1}$$

$$k_{f2} = \left(\frac{n_d n_d}{2}\right)\langle\sigma v\rangle_{f3}$$

$$k_{f3} = \left(\frac{n_d n_d}{2}\right)\langle\sigma v\rangle_{f2}$$

The factor of 1/2 arises from the fact that Deuterium is interacting with itself. In our model, the ion and neutral species are however treated separately, giving us total of 10 equations.

$$k_{f1,t^+,d^+} = (n_{t^+} n_{d^+})\,\langle\sigma v\rangle_{f1}$$

$$k_{f1,t^+,d} = (n_{t^+} n_d)\,\langle\sigma v\rangle_{f1}$$

$$k_{f1,t,d^+} = (n_t n_{d^+})\,\langle\sigma v\rangle_{f1}$$

$$k_{f1,t,d} = (n_t n_d)\,\langle\sigma v\rangle_{f1}$$

$$k_{f2,d^+,d^+} = \left(\frac{n_{d^+} n_{d^+}}{2}\right) \langle \sigma v \rangle_{f2}$$

$$k_{f2,d^+,d} = n_{d^+} n_d \langle \sigma v \rangle_{f2}$$

$$k_{f2,d,d} = \left(\frac{n_d n_d}{2}\right) \langle \sigma v \rangle_{f2}$$

$$k_{f3,d^+,d^+} = \left(\frac{n_{d^+} n_{d^+}}{2}\right) \langle \sigma v \rangle_{f3}$$

$$k_{f3,d^+,d} = n_{d^+} n_d \langle \sigma v \rangle_{f3}$$

$$k_{f3,d,d} = \left(\frac{n_d n_d}{2}\right) \langle \sigma v \rangle_{f3}$$

The $\langle \sigma v \rangle$ term is a function of temperature, and for each pair, we use the higher value of the two products, $T = \max(T_1, T_2)$ It is possible that a density averaged temperature is more appropriate. This will be investigated as part of Phase II effort. The reaction rate (in $(m^3 s^{-1})$ is given by Bosch and Hale [2] in their equation 12:

$$\langle \sigma v \rangle_f = 10^{-6} \cdot C_1 \cdot \theta \sqrt{\xi / (m_r c^2 T^3)} \exp(-3\xi)$$

$$\theta = T / \left[1 - \frac{T\left(C_2 + T(C_4 + TC_6)\right)}{1 + T\left(C_3 + T(C_5 + TC_7)\right)}\right]$$

$$\xi = \left(\frac{B_G^2}{4\theta}\right)^{\frac{1}{3}}$$

with T in keV. The coefficients are given by the authors in Table VII of their text. They are listed here for completeness in Table 4. The $\langle \sigma v \rangle_{f2}$ term for reaction 2 is visualized in Fig. 82b. As can be seen, the rate becomes non-negligible only around $T > 5$ keV.

Table 4. Bosch-Hale reaction rate coefficients for reactivities in cm³/s.

Coefficient	T(d,n)4He (1)	D(d,p)T (2)	D(d,n)3He (3)
$B_g\ (\sqrt{keV})$	34.3827	31.3970	31.3970
$m_r c^2\ (keV)$	1,124,656	937,814	937,814
$C1$	1.17302×10^{-9}	5.65718×10^{-12}	5.43360×10^{-12}
$C2$	1.51361×10^{-2}	3.41267×10^{-3}	5.85778×10^{-3}
$C3$	7.51886×10^{-2}	1.99167×10^{-3}	7.68222×10^{-3}
$C4$	4.60643×10^{-3}	0.0	0.0
$C5$	1.350×10^{-2}	1.05060×10^{-5}	-2.9640×10^{-6}
$C6$	-1.06750×10^{-4}	0.0	0.0
$C7$	1.3660×10^{-5}	0.0	0.0

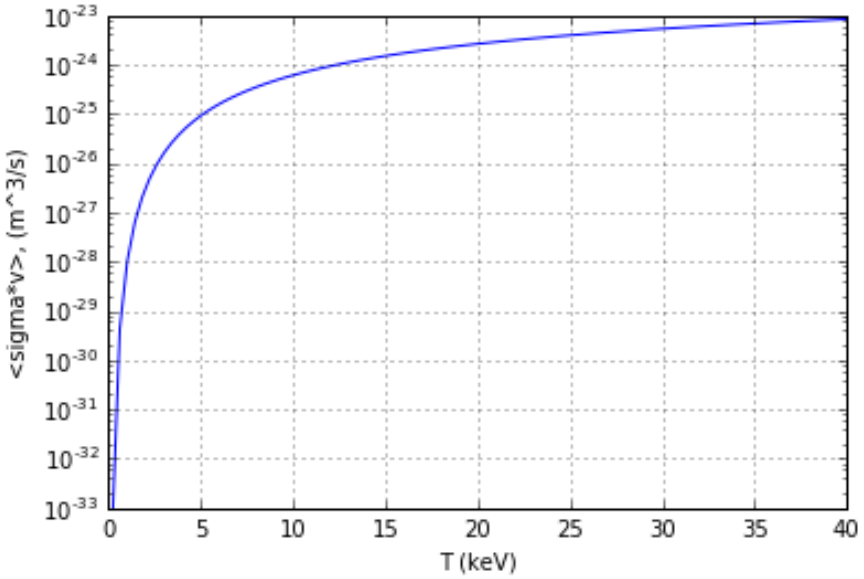

Figure 82b. Visualization of the Bosch Hale $\langle \sigma v \rangle$ term for the D(d,n)4He reaction

The reaction rates can then be used to write terms for the change of species number density,

$$\left(\dot{n}_f\right)_{d^+} = -\left(k_{f1,t^+,d^+} + k_{f1,t,d^+} + 2k_{f2,d^+,d^+} + k_{f2,d^+,d} + 2k_{f3,d^+,d^+} + k_{f3,d^+,d}\right)$$

$$\left(\dot{n}_f\right)_{d} = -\left(k_{f1,t^+,d} + k_{f1,t,d} + k_{f2,d^+,d} + 2k_{f2,d,d} + k_{f3,d^+,d} + 2k_{f3,d,d}\right)$$

$$\left(\dot{n}_f\right)_{t^+} = -\left(k_{f1,t^+,d^+} + k_{f1,t^+,d}\right)$$

$$\left(\dot{n}_f\right)_{t} = -\left(k_{f1,t,d^+} + k_{f1,t,d}\right) + \left(k_{f2,d^+,d^+} + k_{f2,d^+,d} + k_{f2,d,d}\right)$$

Reaction 2, $D(d,p)T$ produces tritium. This product is assumed to be born in the atomic form. The ionization reaction, described below, subsequently creates tritium ions.

The energy released by each fusion reaction is distributed to the species based on the species density fraction. We have

$$\left(S_{f1}\right)_j = \frac{n_j}{n}\left(k_{f1,t^+,d^+} + k_{f1,t^+,d} + k_{f1,t,d^+} + k_{f1,t,d}\right)(17.590MeV)$$

$$\left(S_{f2}\right)_j = \frac{n_j}{n}\left(k_{f2,d^+,d^+} + k_{f2,d^+,d} + k_{f2,d,d}\right)(4.03MeV)$$

$$\left(S_{f3}\right)_j = \frac{n_j}{n}\left(k_{f3,d^+,d^+} + k_{f3,d^+,d} + k_{f3,d,d}\right)(3.268MeV)$$

where $j \in [d^+, d, t^+, t]$ and $n = (n_{d^+} + n_d + n_{t^+} + n_t)$ is the total density. The per-fusion energies are listed for convenience only. The code calculates these based on reactant and product masses. Then finally, the resulting energy term for each species is

$$\left(S_f\right)_j = \left(S_{f1}\right)_j + \left(S_{f2}\right)_j + \left(S_{f3}\right)_j$$

Line Emission Radiation

As excited atoms become de-excited, they emit photons with energy corresponding to the quantum energy lost. This results in a characteristic line emission, with radiation limited to a few distinct spectral frequencies. IAEA AMDIS website[2] provides total emission rates for various chemical elements as a function of energy and density. For hydrogen, the tabulated data is given for pairs within $T_e = [0.5{,}10^5]$ eV and $n_e = [10^{18}, 10^{30}]$ m^{-3} limits. Since we do not model electrons directly, an assumption was made that for each species we can use the atom / ion temperature for the T_e term. All contributions from bound-bound, bound-free and free-free radiative transitions are included in the calculation. While experimenting with the data, we found that the rates can be collapsed into a function solely of temperature by scaling the rates by the electron density. This plot is shown in Fig. 3 by the red line. The blue line shows the standard deviation of data for the given temperature across the density range. We can see that for $T_e \geq 100$ eV, there is almost no dependence on density, as the normalized standard deviation is effectively zero. Even for $T_e \geq 10$ eV we obtain a fairly good approximation, with the error limit to under 50% of the mean value.

The data given by the red curve for $T \geq 10$ eV was tabulated and included in the model. Linear interpolation is used for the intermediary values. Since these rates, r, provide the normalized value per density given in ergs, we obtain the corresponding power density term for the energy equation from

$$S_{le,j} = r(T_j) n_j \cdot 10^{-7}$$

The factor on the RHS corresponds to the conversion $1\ erg = 10^{-7}\ J$. This equation is applied to each species.

[2] https://www-amdis.iaea.org/FLYCHK/ZBAR/csd001.php

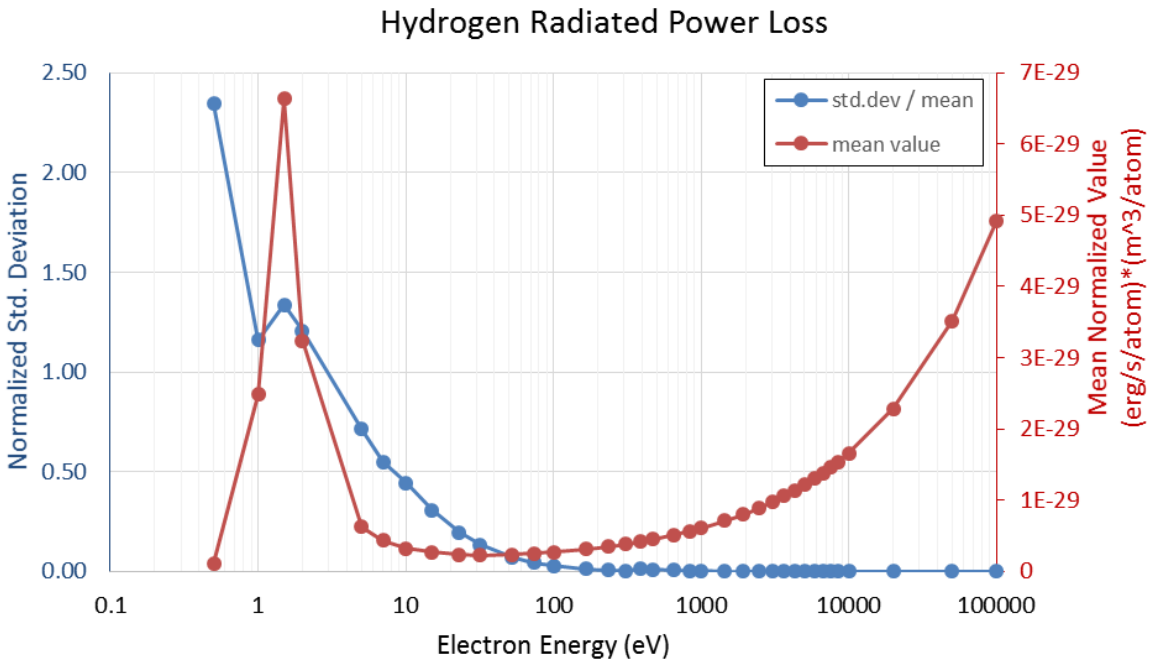

Figure 83. Line emission radiated power loss rates for hydrogen. Original data from AMDIS.

Bremsstrahlung Radiation

Another radiation loss is due to Bremsstrahlung radiation. This radiation arises in plasmas from slowing down of charged particles as they interact with each other. This term IS NOT included in the model since it appears the contribution is already included in the AMDIS line emission spectrum above. But if needed, it could be approximated using a power density loss due to thermal effects model given by Wikipedia as

$$P_{br} = \frac{Z_i^2 n_i n_e}{[7.69 \times 10^{18} m^{-3}]^2} \sqrt{\frac{eT_e}{k}}$$

Here Z_i is the average ionization state of the ions.

Elastic Collisions

Energy transfer due to inter-species elastic collisions is given by Fife [134] as

$$S_{e,j} = m_j n_j \sum_r \nu_{jr} \left[\left(\vec{v}_r - \vec{v}_j \right)^2 + \frac{3}{m_r} k_b \left(T_r - T_j \right) \right]$$

Here species j is interacting with background species r. The first term arises from drag in gases with species moving at different average streaming velocity. This term can be ignored since the species are at rest. The second term is the random thermal energy transfer. We thus have

$$S_e = n_j 3k_b \sum_r \nu_{jk} \frac{m_j}{m_r}(T_r - T_j)$$

Here $\nu_{jr} = n_r\langle\sigma v_{th}\rangle$ is the collision frequency (in 1/s) for momentum transfer collisions. We use the model of Bird (eq. 4.64) to approximate this rate as

$$\langle\sigma v_{th}\rangle = 4d_{ref}^2 \left(\frac{\pi k T_{ref}}{m}\right)^{\frac{1}{2}} \left(\frac{T}{T_{ref}}\right)^{1-\omega}$$

For molecular hydrogen H_2, Bird's Appendix A gives $d_{ref} = 2.92 \times 10^{-10}$m, $\omega = 0.67$, and $T_{ref} = 273.15$ K. We use these same values in our model, but assume atomic hydrogen, with $d_{ref} = 1.46 \times 10^{-10}$ m. The values for T and m are obtained by density averaging the two reacting species.

Ionization

Finally, ionization should be included since the release of an electron requires finite energy, and ionization thus acts as another energy sink. Here we use a macroscopic approximate model based on the Saha equation, which provides an expression for the ionization state of the gas. Specifically, it relates the number density of atoms in ionization state "i" to those in the next ionization state "i+1" at some temperature T. It is given by

$$\frac{n_{i+1}n_e}{n_i} = \frac{2}{\lambda^3}\frac{g_{i+1}}{g_i}\exp\left[-\frac{\epsilon_{i+1} - \epsilon_i}{k_B T}\right]$$

Here λ is the thermal de Broglie wavelength of an electrons and is given by

$$\lambda = \sqrt{\frac{h^2}{2\pi m_e k_B T}}$$

with h and k_B being the Planck and Boltzmann constants, respectively. The $\Delta\epsilon = (\epsilon_{i+1} - \epsilon_i)$ term is the energy required to remove the $(i+1)^{th}$ electron. The degeneracy ratio is given for hydrogen3 as

[3] "Princeton U. A403 notes," https://www.astro.princeton.edu/~gk/A403/ioniz.pdf

$$\frac{g_{i+1}}{g_i} = \frac{1}{2}$$

For hydrogen, which contains only a single electron, we have $\Delta\epsilon = 13.603$ eV[4]. We can write a modified form of the equation by assuming neutrality $n_i = n_e$ and defining total density $n = n_0 + n_i$. Therefore

$$\frac{n_i^2}{n - n_i} = s$$

or alternatively,

$$n_i^2 + n_i s - n\, s = 0$$

where

$$s = \frac{2}{\lambda^3}\frac{g_{i+1}}{g_i}\exp\left[-\frac{\epsilon_{i+1} - \epsilon_i}{k_B T}\right]$$

We can then use the quadratic equation to obtain the electron density at some temperature

$$(n_i)_{saha} = \frac{-s + \sqrt{s^2 + 4sn}}{2}$$

The resulting ionization state is visualized in Fig. 5. The noise at higher values seems to be due to numerical overflow errors. The ionization rate increases with temperature but decreases with density. The density dependence is likely due to the increase in recombination events at higher densities. We can see that for $T_e \geq 1000$ eV, the Deuterium/hydrogen population can be expected to be fully ionized.

[4] https://webbook.nist.gov/cgi/cbook.cgi?ID=C16873179&Mask=20

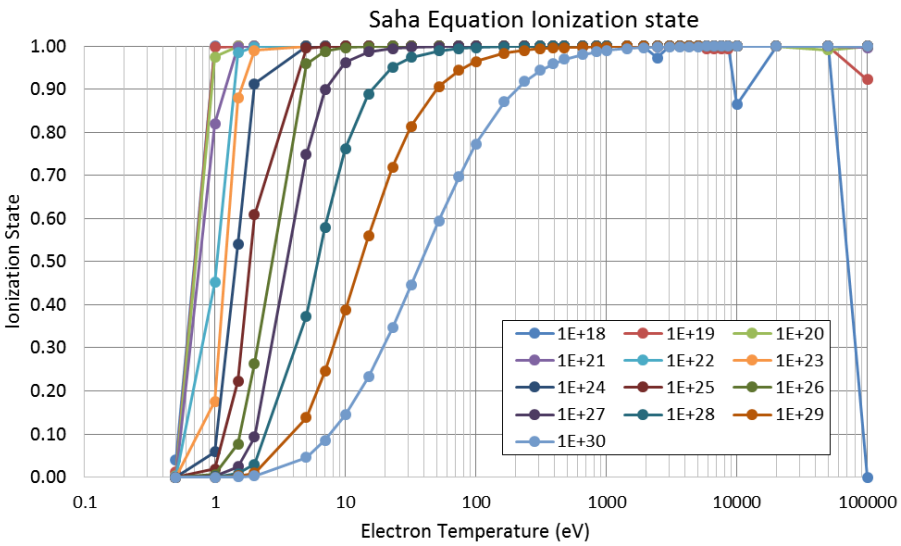

Figure 84. Hydrogen ionization state per the Saha equation

In our model, the Saha equation is applied individually to Deuterium and tritium. For both species, we compute

$$(\dot{n}_i)_{d^+} = \frac{(n_{d^+})_{saha} - n_{d^+}}{\Delta t}$$

$$(\dot{n}_i)_d = -(\dot{n}_i)_{d^+}$$

and

$$(\dot{n}_i)_{t^+} = \frac{(n_{t^+})_{saha} - n_{t^+}}{\Delta t}$$

$$(\dot{n}_i)_t = -(\dot{n}_i)_{t^+}$$

Here n_{d^+} is the deuteron density actually in the simulation and $(n_{d^+})_{saha}$ is the density predicted by the Saha equation. The corresponding energy loss is

$$(S_i)_d = (\dot{n}_i)_{d^+} \cdot \epsilon_i$$

$$(S_i)_t = (\dot{n}_i)_{t^+} \cdot \epsilon_i$$

where $\epsilon_i = 13.603$ eV is the hydrogen first (and only) ionization energy.

Unfortunately, the above model tends to predict an instantaneous conversion of all neutrals to ions. This can then result in a numerical instability, since the neutral density instantaneously drops to zero. For this reason, a limiter was first implemented limiting the conversion to no more than 20% of the neutrals per time step. Unfortunately, this did not resolve the instability issue and therefore ionization is disabled in the Phase I set of simulations. Further investigation of ionization driven numerical instabilities will be investigated in Phase II.

Final Form

Combining terms, we obtain

$$\dot{n}_{d^+} = (\dot{n}_a)_{d^+} + \left(\dot{n}_f\right)_{d^+} + (\dot{n}_i)_{d^+}$$

$$\dot{n}_{d^+} = \left(\dot{n}_f\right)_{d} + (\dot{n}_i)_{d}$$

$$\dot{n}_{t^+} = \left(\dot{n}_f\right)_{t^+} + (\dot{n}_i)_{t^+}$$

$$\dot{n}_{t} = \left(\dot{n}_f\right)_{t} + (\dot{n}_i)_{t}$$

and

$$S_{d^+} = (S_a)_{d^+} + \left(S_f\right)_{d^+} + (S_e)_{d^+} + (S_{le})_{d^+}$$

$$S_{d} = (S_a)_{d} + \left(S_f\right)_{d} + (S_e)_{d} + (S_{le})_{d} + (S_i)_{d}$$

$$S_{t^+} = (S_a)_{t^+} + \left(S_f\right)_{t^+} + (S_e)_{t^+} + (S_{le})_{t^+}$$

$$S_{t} = (S_a)_{t} + \left(S_f\right)_{t} + (S_e)_{t} + (S_{le})_{t} + (S_i)_{t}$$

2-D Ignition Model

An effort was undertaken to implement a preliminary 2D hybrid fluid-particle simulation of the ignition process. This simulation uses the hybrid Particle in Cell (PIC) method, with the dense Deuterium modeled as a constant density background fluid, and ions, generated by the annihilation process, as particles. The simulation was performed using the open source simulation code Starfish5.

[5] Available at https://www.particleincell.com/starfish/

Fig. 85 shows the computational domain. The ions are injected into the simulation from a small circle with $r = 10^{-9}$ m at $\dot{m} = 0.1$ kg/s. This mass flow rate was selected to obtain sufficiently high ion number densities. Density of the background Deuterium was set to $n_d = 10^{31}$ m-3. The simulation mesh used 50×100 cells with uniform $\Delta h = 10^{-9}$ m.

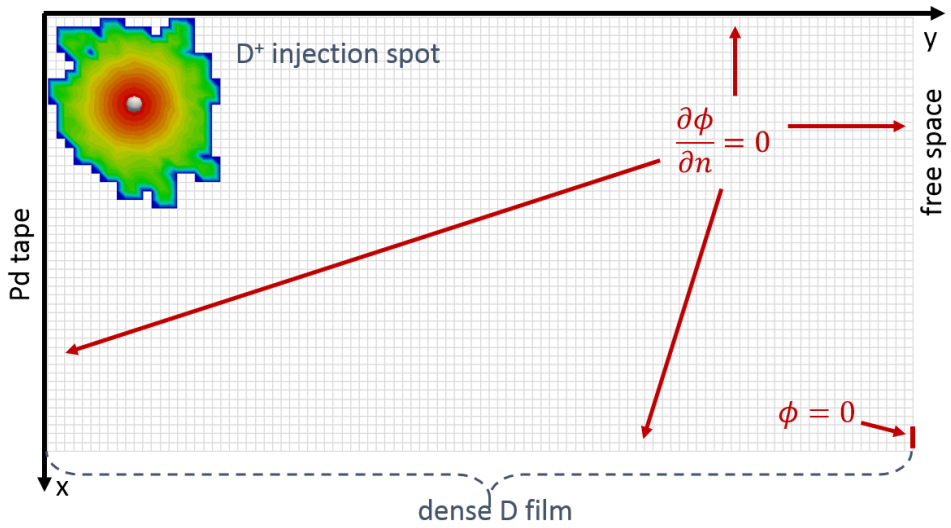

Figure 85. Conceptual 2D simulation domain.

Collision Energy Transfer

The simulation uses the MCC scheme to perform ion-neutral collisions. In this scheme, particles collide with a target "cloud". Momentum exchange collision can be modeled by sampling a virtual particle from the target population and then performing a standard binary collision between the two particles. In standard MCC, the virtual particle is discarded post collision and there is no momentum or energy transfer to the target population. Here a modification was made to allow for energy transfer. The different between pre- and post- collision energy of the interacting particle is deposited to the target "S" field. This is a new mesh-based quantity defined for fluid materials that stores the net energy density rate, which forms the RHS of the energy equation,

$$\frac{\partial}{\partial t}\left(\frac{3}{2}n_j k T_j\right) + \nabla \cdot \left(\frac{3}{2}n_j \vec{v}_j k T_j + \vec{q}_j\right) + p_j \nabla \cdot \vec{v}_j = \sum S_j$$

Starfish does not yet contain a detailed energy equation solver. This is something that is envisioned to be completed as part of Phase II effort. Instead, the zero-dimensional model was implemented for now. This form ignores the spatial derivative terms on the left and advances temperature per

$$\frac{\partial}{\partial t}\left(\frac{3}{2}n_j k T_j\right) = \sum S_j$$